

The Saturation Calibration Of Tokai To Kamioka Fine Grained Scintillating Detector

Compensating For Saturation In Hamamatsu's
Multi-Pixel Photon Counter With A Relative
Calibration

by

Simon Philip Hastings

B.Sc., The University of British Columbia, 2008

A THESIS SUBMITTED IN PARTIAL FULFILLMENT OF
THE REQUIREMENTS FOR THE DEGREE OF

MASTER OF SCIENCE

in

The Faculty of Graduate Studies

(Physics)

THE UNIVERSITY OF BRITISH COLUMBIA

(Vancouver)

August 2010

© Simon Philip Hastings 2010

Abstract

A relative calibration of the Fine-Grained Detector (FGD) in the T2K experiment is presented, with emphasis on the saturation calibration effects in Hamamatsu's multi-pixel photon counters (MPPCs). The calibration is produced on a test bed with a Hamamatsu Pico-Second Pulsed laser, on a small model of the FGD on a sample of fibers and MPPCs. The wavelength shifting fiber-MPPC complex used in the FGD is found to have an effective pixel count of 518, and to exhibit an effective after-pulsing and crosstalk fraction of 1.6% when measured between 0.6 and 0.9 Volts over-voltage (V OV).

Table of Contents

Abstract	ii
Table of Contents	iii
List of Tables	v
List of Figures	vi
1 Introduction	1
1.1 The Neutrino	1
1.2 The T2K Experiment	5
1.2.1 Neutrino Oscillation	6
1.2.2 Physical Processes	10
1.3 MPPC Overview	12
1.4 The Fine Grained Detector	16
1.4.1 FGD Optical Geometry	17
1.4.2 FGD Electronics	20
1.5 Software Overview	23
1.6 The MiniFGD Analysis	24

Table of Contents

2	Optical Equipment and Linear Optical Unit Construction	33
2.1	The Poisson Analysis Method	33
2.2	Constructing The Linear Optical Unit System	38
3	Low level Data Calibration	56
3.1	The Mean Analysis Method	57
3.2	The High To Low Channel Conversion	60
3.3	Gate Timing Selection	67
3.4	Pulse Height to Photoelectron Conversion	70
3.5	Determining the Over-Voltage of an MPPC	73
4	The MiniFGD Saturation Analysis	77
4.1	Saturation Parametrization	77
4.2	Saturation Fit Parameters on Bare MPPCs	83
4.3	Fiber Saturation Studies	93
5	Conclusion	109
5.1	Calibration Results	109
5.2	Future Work	111
	Bibliography	113
	Appendices	
	The Attenuation Calibration	119

List of Tables

1	Part One of constants for calibrating the digital optical attenuator	120
2	Part Two of constants for calibrating the digital optical attenuator	121
3	Parts three of constants for calibrating the digital optical attenuator	122

List of Figures

1.1	Beta Decay Representation	2
1.2	The Off-Axis Effect	6
1.3	Histogram of Pulse Heights	14
1.4	FGD Without Cover	18
1.5	MPPC to WLS Fiber Coupler	19
1.6	FGD Electronics	29
1.7	Pre-ASIC Voltage Divider	30
1.8	Photograph of a bare MPPC exposure	30
1.9	Photograph of an MPPC coupled to a laser illuminated WLS fiber	31
1.10	Correlation Between Poisson Analysis and apparent Power . .	32
2.1	Gate Comparison Method	35
2.2	Temperature And Dark-Current in the power-meter	40
2.3	Overview of a Calibration Run	41
2.4	Overview of a Calibration Run	42
2.5	Micro-structure Lab Temperature and Laser Stability	43
2.6	Comparison of Calibration Locations	44
2.7	Residual of Attenuation Calibrations	45

List of Figures

2.8	Correlation of Laser with Temperature	47
2.9	Relationship Between Laser Output and Temperature	48
2.10	Correlation Between Poisson Analysis and apparent Power . .	51
2.11	Residuals of Correlation against apparent Power	52
2.12	Attenuation Calibration to Poisson Analysis Intercepts For Fibers	53
2.13	Attenuation Calibration to Poisson Analysis Intercepts For Fibers	53
2.14	Attenuation Calibration to Poisson Analysis Intercepts For Bare MPPCs	54
2.15	Attenuation Calibration to Poisson Analysis Intercepts For Bare MPPCs	54
2.16	Relative Residuals of Correlation against apparent Power . .	55
3.1	Histogram of Pulse Heights	57
3.2	Histogram of average event net pulse height	58
3.3	Mean analysis and Poisson Analysis Comparison	61
3.4	Mean analysis to Poisson Analysis Ratio	62
3.5	Mean to Poisson analysis scatter plot	63
3.6	Mean to Poisson Analysis Residual	64
3.7	An Example Waveform from 2009	65
3.8	High vs. Low Channel Scatter-plot with Fit	66
3.9	Pulse Height Histogram showing low channel distortion . . .	66
3.10	High-Low conversion factor for all MPPCs	67
3.11	Wide Histogram of pulses over the waveform	68

List of Figures

3.12	Narrow Histogram of pulses over the waveform	69
3.13	One Photoelectron Pulse Height Fit	71
3.14	Temperature and One Photoelectron Pulse Height values for an MPPC Run Series	74
3.15	One Photoelectron Pulse Height Fits and Veto Efficiency . .	75
3.16	Temperature values for an MPPC run series	76
4.1	Plots of four saturation curves with default parameters	82
4.2	Plots of bare saturation curves with 2 parameters fit	85
4.3	Plots of bare saturation curve residuals with 2 parameters fit	86
4.4	Plots of bare saturation curve relative residuals with 2 pa- rameters fit	87
4.5	Fit parameters for one bare MPPC as a function of voltage .	88
4.6	Fit parameters for all bare MPPCs as a function of voltage .	89
4.7	Bare MPPC data overlaps	90
4.8	Bare MPPC data reduced χ^2 for two parameter fits	91
4.9	Plots showing the pull from the 2 parameter fit on bare data	92
4.10	Near and Far WLS Fiber Data Overlap	94
4.11	Plots of fiber saturation curves with 2 parameters fit	99
4.12	Plots of fiber saturation curve residuals with 2 parameters fit	100
4.13	Plots of fiber saturation curve relative residuals with 2 pa- rameters fit	101
4.14	Fiber MPPC data chi-squares for two parameter fits	102
4.15	Fit parameters for one fiber MPPC as a function of voltage .	103
4.16	Fit parameters for all fiber MPPCs as a function of voltage .	104

List of Figures

4.17	Fiber MPPC data overlaps	105
4.18	Fiber MPPC data inverted overlaps	106
4.19	Residuals of fiber overlap data	107
4.20	RMS of fiber overlap data	108
5.1	Fiber MPPC data overlaps	109

Chapter 1

Introduction

The goal of this work is the production of a saturation calibration for a new type of photo-sensor: the Multi-Pixel Photon Counter (MPPC) from Hamamatsu. The MPPC is being used as the primary light sensor in the near detector of the T2K experiment. The primary physics goals of the T2K experiment are to measure the neutrino oscillation parameter θ_{13} , as well as to make more precise determinations of the atmospheric oscillation parameters Δm_{23}^2 and θ_{23} . The measurements are performed by counting the ratio of ν_e induced events to the number of ν_μ induced events at a near and far detector. The difference in the event ratio will allow us to measure the appearance of excess ν_e and disappearance of ν_μ along the path between the two detectors.

1.1 The Neutrino

The neutrino was first postulated in 1930 by Wolfgang Pauli to solve the problem of lost energy and momentum in beta-decay[4]. The initial motivation for the particle stemmed from the observation that beta decay showed the kinetic characteristics of a multi-body decay that could not be explained by the observed two child products. Despite the decay of alpha particles

1.1. The Neutrino

showing a discrete energy spectra, beta decay was found to obey a continuous relationship[6]. This implied that energy and momentum were unaccounted for in the observed daughter particles. This constituted an apparent violation of conservation laws, as in figure 1.1.

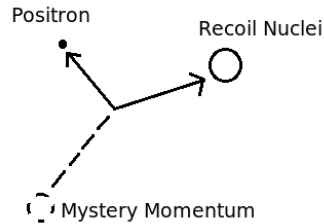


Figure 1.1: The energy spectrum of the visible products of beta-decay indicated that either momentum and energy were not conserved quantities, or that there was a mystery particle present, carrying off the excess.

This observation triggered a debate on whether nature conserved energy and momentum in this reaction, which for some scientists was a less abhorrent consequence than the creation of an “invisible” particle - one that is uncharged, very light, and weakly interacting. Pauli, having delayed the publication of his idea while he consulted with experimentalists, is famously quoted as saying: “I have done something very bad today by proposing a particle that cannot be detected; it is something no theorist should ever do.” [2][4].

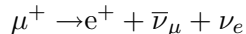
The accepted modern decay mechanism of an isotope such as ^{22}Na is the conversion of a proton to a neutron via the weak force, with the production of a transmuted isotope and a positron-neutrino pair:

1.1. The Neutrino



While direct observation of the neutrino is difficult, it is not impossible as Pauli once feared. Neutrinos, by their nature, have a signature of an interaction: visible products with momentum indicating a particle interacted from a direction where no particle is observed. Early experiments show direct evidence of the neutrino using reactors. An early confirmation in 1956 of free-neutrinos involved a reactor experiment at the Savannah River Plant by Cowan et al[18]. They found a cross-section of $6.3 \times 10^{-44} \text{ cm}^2$, and had an event rate of 2.88 per hour with a signal to background ratio of about 3 to 1. This low event rate illustrates the intrinsic difficulty of these experiments. Modern accelerator beam-based experiments such as T2K use a neutrino beam for study. Because of its high intensity beam, the off-axis detector will see of order one neutrino interaction per second during exposure.

In 1937, shortly after Pauli suggested the existence of the neutrino, evidence for the muon was identified in cosmic rays[20]. This particle was observed to have a decay mode of (although the two neutrinos were not known to be distinct at the time):



while other seemingly possible modes, such as $\mu^+ \rightarrow e^+ + \gamma$ were not observed. It was then conjectured that there must be a conservation law enforcing the decay mode selection[15]. This conservation law enforces the requirement that the sum of each lepton flavor number, where every lepton was assigned a flavor and sign, must be the same before and after a

1.1. *The Neutrino*

discrete interaction. At the time this allowed for ν_e and e^- to have be electron flavor, with electron lepton number 1 and muon lepton number zero. Likewise the μ^- and ν_μ had muon lepton number 1, with the anti-particle versions having the opposite sign. In 1975 the Stanford Linear Accelerator laboratory reported anomalous events with missing energy and momentum which were ultimately attributed to a third member of the lepton family: the tau particle[21]. Like the muon and electron, the tau particle is thought to conserve a flavor number in interactions.

Recent evidence, including oscillation of neutrino flavor type in the atmosphere, the sun, and in beam and reactor produced neutrinos, indicates that flavor number is not a conserved quantity in neutrinos. This can be understood as the result of the mass and flavor eigenstates of the neutrino not coinciding - and a necessary consequence is that there are multiple mass eigenstates, with at least two with non-zero mass[19]. The T2K experiment aims to further explore the oscillation in neutrinos, and to measure some of the oscillation parameters.

1.2 The T2K Experiment

The Tokai To Kamioka (T2K) experiment is a neutrino oscillation measurement experiment. In the fashion of previous neutrino beam based experiments such as K2K, the experiment consists of a near detector complex and a far detector complex. A proton beam incident on a target is used to produce a neutrino beam. The near detector is placed in a pit 280 meters from the beam source (hence the moniker ND280). The ND280 complex functions to characterize the pre-oscillation beam conditions. The ND280 complex consists of the INGRID detector, which is on-axis (where the axis is defined by the path of the proton beam), and a complex placed 2.5 degrees off-axis of the beam along a straight line to the far detector, Super-Kamiokande (SK). The beam is aimed 2.5 degrees off-axis in order to take advantage of the “off-axis effect”, a phenomenon where the energy spectrum of a neutrino beam narrows substantially just off the central axis[3]. This effect is shown in Figure 1.2[16]. The far detector measures the probability of ν_μ disappearance and ν_e creation, by comparing the neutrino events at SK to the values seen at the near detector. Due to the energy of the beam, negligible numbers of ν_τ events are expected. Unlike some previous experiments, the near detector is composed of a fundamentally different type of detector than SK. The near detector is composed of predominantly scintillation based detectors, with the tracker complex composed of three time-projection chambers around two fine grain detectors and surrounded by calorimeters (ECALs) both downstream and axially. The far detector by contrast is a Cherenkov radiation based detector. A matching detector would provide many benefits

including allowing the uncertainty in some measurements to be canceled out between the detectors. The transition to a non-matching detector type in this experiment results from the high-intensity beam present in the ND complex. This is necessary because Cherenkov detectors are impractical when beam intensity is such that more than one event is likely occurring in the detector during a spill, making event reconstruction difficult.

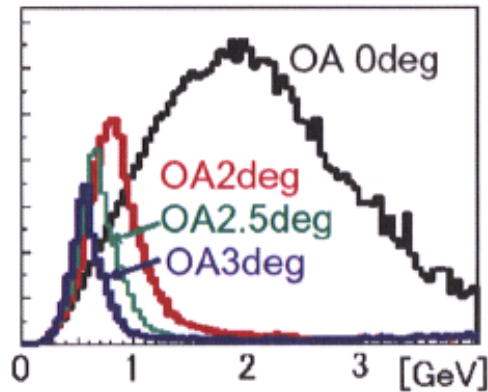


Figure 1.2: The T2K beam energy spectrum for possible off-axis beam positions. T2K presently uses a 2.5 degree offset. Figure is taken(Permission pending) from [16].

1.2.1 Neutrino Oscillation

Neutrino flavor oscillations are the result of the mass eigenstates of the neutrino not being diagonal in the flavor eigenstates, and having small and different mass values. Each neutrino is produced in a determined lepton family by the conservation of lepton flavor number in the weak force. The neutrino flavor state can be expressed as a sum of mass eigenstates:

1.2. The T2K Experiment

$$|\nu_\alpha\rangle = \sum_{i=1}^3 U_{\alpha i}^* |\nu_i\rangle$$

where α is one of the neutrino flavors e , μ and τ . $U_{\alpha i}$ are the elements of a unitary matrix, and $|\nu_i\rangle$ are the mass eigenstates. This model assumes that there are only 3 eigenstates in mass, and ignores the possibility of sterile neutrinos.

Using the above expression, and allowing for evolution through the Schrodinger equation one can derive that the probability of oscillation between states is[19]:

$$\begin{aligned} P(\nu_\alpha \rightarrow \nu_\beta) &= \delta_{\alpha\beta} \\ &- 4 \sum_{i>j} \Re(U_{\alpha i}^* U_{\beta i} U_{\alpha j} U_{\beta j}^*) \sin^2(1.27 \Delta m_{ij}^2 (L/E)) \\ &+ 2 \sum_{i>j} \Im(U_{\alpha i}^* U_{\beta i} U_{\alpha j} U_{\beta j}^*) \sin(2.54 \Delta m_{ij}^2 (L/E)) \quad (1.1) \end{aligned}$$

In these equations Δm_{ij}^2 is the mass-difference squared between states i and j , L is the distance traveled by the neutrino in the laboratory frame in km, and E is the energy in GeV. If $U_{\alpha i}$ is not real and the imaginary terms do not cancel in the above expression, then the transition probability for anti-neutrinos is different then the probability for neutrinos. The observation of such an asymmetry would imply CP violation.

The unitary matrix can be decomposed into sub-components of three angles, and a CP violating term. These, together with the separation of mass states, describe the oscillation probabilities. The evidence for non-zero mass states comes from a number of sources. Two sources used in a variety of

investigations are atmospheric neutrinos and solar neutrinos. Experiments exploiting these sources to measure oscillation parameters are described in the following sections. The primary purpose of the T2K experiment is to determine three of these parameters: θ_{13} , θ_{23} and Δm_{23}^2 .

Atmospheric Neutrino Oscillations

Early evidence for neutrino oscillations is found in the flux of neutrinos generated in the atmosphere. When cosmic rays strike the atmosphere, neutrinos are formed with electrons and from decays of produced muons, pions and kaons produced in air showers. The SK detector (located in a mine in Gifu, Japan) measured the upwards and downwards flux of neutrinos from this source. These results were then compared to a set of Monte-Carlo simulations of the flux (which included corrections for the solar activity at the time, and the shape of the earth's magnetic field). The asymmetry between the two classes of events was used as evidence that in the process of traversing the earth, the neutrino flavor types were oscillating[7]. This analysis was able to infer from the direction and energy of an incoming neutrino what its likely path length from creation was. Atmospheric neutrinos are observed with a range of path lengths going from neutrinos coming straight down from the zenith position up to neutrinos coming straight up through the earth towards the zenith position. The energy and path length can then be used to determine the oscillation parameters by comparing to the fraction of missing ν_μ .

Solar Neutrino Oscillations

Another neutrino oscillation component has been measured by examining the neutrino flux from the Sun. Solar neutrinos are a by-product of several of the reactions occurring in the Sun, including proton-proton fusion. Measurements of the neutrino flux of the sun found that in multiple energy ranges there were less ν_e than expected. Ray Davis's famous Homestake experiment measured the combined flux of mono-energetic ${}^7\text{Be}$ and ${}^8\text{B}$ neutrinos using the reaction ${}^{37}\text{Cl} + \nu_e \rightarrow {}^{37}\text{Ar} + e$. This reaction had a threshold at 0.814 MeV, resulting in detection of only a range of the neutrino energy spectrum[11]. The solar neutrino problem was also identified at the Kamiokande detector, which was only sensitive to ${}^8\text{B}$ neutrinos[23]. Kamiokande uses a real-time detector, in contrast with the radio-chemical methods used by the Homestake experiment.

The total energy output of the Sun, and knowledge of which processes dominate during fusion should predict the neutrino energy spectrum and flux. The gap between theory and observation in these experiment threw the fusion model into question. The mystery was solved when SNO lab measured processes which measured both total neutrino flux and electron neutrino flux. The SNO detector contains heavy water, which allows three signal processes to be measured[14]:



1.2. The T2K Experiment

$$\nu + d \rightarrow p + n + \nu \quad (1.3)$$

$$\nu + e^- \rightarrow \nu + e^- \quad (1.4)$$

The first process is sensitive only to electron neutrinos, whereas the second two are sensitive to all flavors. The second has the same cross-section for all flavors, while the third has an ν_e cross-section about 6.5 times the cross sections for other flavors[19]. This third process was also measured at SK, and facilitated comparison of the results.

The first two relations above allowed the SNO experiment to find that the total neutrino flux was the size expected but that the flavor mix was about 1/3 electron and 2/3 other flavor. As electron neutrinos would be expected to dominate neutrino flux from theories of nuclear processes in the Sun, a flavor change must be occurring to explain this result[14]. A necessary consequence of the mixing angles implied by these experiments is that any $\bar{\nu}_e$ that travel more than a hundred km should show substantial oscillation into other flavor states[19]. The KamLAND experiment is situated in between commercial nuclear plants in Japan, and does in fact observe a $\bar{\nu}_e$ disappearance with neutrino oscillation parameters consistent with those measured by the solar experiments[13].

1.2.2 Physical Processes

The T2K experiment depends on the measurement of various processes which are directly related to the flux of the incident neutrino beam. Due to the various detector capabilities, the background and signal processes will appear somewhat differently at the SK detector than at ND280.

1.2. The T2K Experiment

In both the ND280 detector and at SK, the primary measurement is performed by differentiating between Charged Current Quasi-Elastic (CCQE) processes involving electrons and muons.

$$\nu_l + n \rightarrow l + p$$

Where l may be either μ , e , or τ , and n is a bound neutron while p is recoil proton. The CCQE mode is a desirable method of measurement because it is two body (and hence is easy to reconstruct), and at SK the proton is usually below threshold to produce a ring, giving a very clear signature for detection.

The separation of ν_μ and ν_e therefore depends on being able to distinguish between the creation of a muon, and the creation of an electron through this reaction. At SK, this distinction is performed on the pattern and angle of the Cherenkov light cone. While electrons will cause electromagnetic cascades and produce diffuse rings of light, muons will tend to create rings which have sharper edges[7]. At ND280 muons and electrons are distinguished based on the energy deposition, range, and momentum.

In addition to the process listed above, there are several background process which are easily confused with the above process, and cuts must be applied to remove them. In particular, CC1 π events (in which a neutrino produces a lepton and a charged pion via a charged current interaction) are the largest part of the background[1], occurring when a pion is produced but is absorbed by a nucleus before it is detectable (or lost due to detector inefficiency). Other processes such a NC1 π and NC-multi π (in which a neutral current interaction produces pions) make up other large contributions to the

background[3]. These background processes have characteristic signatures which allows estimation of their cross-sections. Characteristic signatures include recoil proton angle from events which appear to be CCQE, the presence of gamma-ray pairs in the same event, and the presence of Michel electrons. At SK non-quasi-elastic processes can be indistinguishable from quasi-elastic processes, which makes characterizing them at ND280 important[3].

1.3 MPPC Overview

Hamamatsu's MPPC is an array of silicon photo avalanche diodes which acts as photo-sensor in ND280. Silicon photo avalanche diodes(SiPMs) are semi-conductor devices that are composed of layers of doped wafer with micro-electronics. Each layer is held at a bias voltage, creating an electric field within the wafer. SiPMs are interesting because once an individual section of wafer has had a photo-carrier created, it will accelerate through the electric field with enough energy to impact-ionize other carriers. In this manner an avalanche of both holes and electrons can occur[22]. An avalanche is accelerated across an electric field which grows linearly with the voltage above the breakdown voltage - the voltage where the average number of carriers produced by an initial carrier is larger than one. SiPMs are appealing for their insensitivity to magnetic fields, and their relatively low bias voltages (about 70 V in our case).

An MPPC is composed of 667 such pixels such that an avalanche in a pixel results in a discrete current discharge. Each pixel independently detects light, and shares a common bias voltage. The output of the device

is the combined current released from all firing pixels. Each pixel can be considered a capacitor held at a bias voltage above a critical breakdown voltage (where the difference between the bias voltage and the breakdown voltage is called the over-voltage, or OV). Because of wafer uniformity, each pixel fire produces a similar amount of current. A primary strength of the MPPC is that at room temperature the variations in current produced by pixels are small. This allows distinction between discrete numbers of pixel fires (in our electronics, at our typical OV and at room temperature) up to about seven photo-avalanches. An example pulse height histogram showing the discrete output for low light level is shown in Figure 1.3. Below the break-down voltage, exposure to light will result in a trickle current through the pixel. Above this voltage the an interacting photon will result in the complete discharge of that pixel. All MPPCs in the T2K experiment are operated above the breakdown voltage and hence in “Geiger mode”.

By selecting the input resistance and capacitance to the MPPCs, we are able to tune the rate that charge re-accumulates on the MPPC. A short recharge rate (relative to the length of an optical pulse) would allow for a much higher dynamic range, but would also complicate the descriptions of saturation effects by making them dependent on the length of the pulse they are exposed to. For the detector used in this work, the Fine Grained Detector (FGD), the time constant for low levels of charging is $0.6 \mu\text{s}$. For longer recoveries where we have depleted a charging capacitor near the MPPC, we expect a time constant of 0.1 s . In addition, a much shorter time constant of 13.4 ns governs the transfer of charge between unfired and fired pixels in a single MPPC[5]. The geometry we are using in the FGD makes optical pulses

1.3. MPPC Overview

longer than the fast external pixel recharge rate infrequent. As a result, the most likely manner in which a pixel may fire twice during one optical exposure is via charge transfer from an adjacent pixel. If our electrical design were different it would be possible to fire each pixel many times during a single exposure due to charge flowing onto the MPPC from outside the array. For the FGD, the total charge released during a single optical exposure is limited by the total charge present on the MPPC at the beginning of exposure. Because MPPCs have a finite number of pixels with a limited capacity for recharge, the MPPC will show saturation effects. This body of work aims to characterize these effects.

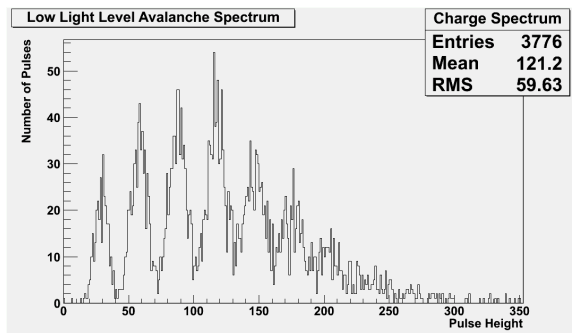


Figure 1.3: This histogram shows the discrete photo-electron spectrum that is the result of the combined effects of a signal and a background dark noise selection.

Another strength of the MPPC is that many temperature sensitive effects can be described well as a shift in the break-down voltage of the MPPC with a 56 mV/degree linear relationship. The gain and particle-detection efficiency (PDE) are both thought to obey this relationship, with the gain being a linear function of OV while the PDE is linear near the break-down

voltage and approaches an asymptote of the maximum efficiency of the device as voltage increases.

A notable feature of MPPCs is the presence dark noise. Dark noise pulses are spontaneous avalanches in a pixel triggered through thermal rather than optical processes. These represent spontaneous firing of pixels due to thermal noise. Dark noise only occurs in unfired pixels. As a result, it is not independent of the state of charge depletion in the MPPC. These pulses have the effect of placing a lower limit on the sensitivity of the system. Dark noise is indistinguishable from genuine optical signals but tends to be predominantly limited to one photo electron signals. While two or more photo electron signals are present within the dark noise spectrum, the drop-off is extremely rapid. In practice in order to achieve high signal sensitivity, it is necessary to understand the background dark noise in the optical signal and correct for it. This becomes less important at high intensity where dark noise will be suppressed by optical pixel fires and is small compared to the number of optically induced pixel fires. The dark noise rate is unusual among the effects in the MPPC in that it is sensitive to both temperature and OV in a non-linear fashion.

Two additional effects must be understood about the MPPCs in order to analyze data with them. The first, crosstalk, is the firing of a pixel by a photon released by an avalanche in another pixel in the array. The second, after-pulsing, is an event where carriers in an avalanche become trapped in local minima in the lattice. The trapping is meta-stable, and within a microsecond the pixel finishes firing. In a similar model of MPPC (which uses a 1.0×1.0 mm face rather than 1.3×1.3 mm) the after-pulsing was

found to have two time constants of 15.0 ns and 83.5 ns[12]. In the FGD system much of this activity is integrated by the pulse shaper which is set to approximately integrate the charge output of the MPPC over a rise-time of 100 ns.

1.4 The Fine Grained Detector

The Fine Grained Detector (FGD) is a segmented scintillating detector situated between the three time projection chambers[3]. Its primary purpose is to act as an active target mass, providing the tracker with tracking and energy deposition measurements for particles. In particular, low energy protons and charged pions are unlikely to exit the FGD, and in order to detect them the FGD employs fine segmentation in its scintillator bars (and hence acquires its name). Finer segmentation also allows the FGD better angular resolution and tracking efficiency on recoil protons, which is necessary to understand the background[3]. Each FGD is composed of alternating planes of 192 bars oriented in the x-direction and y-direction (referred to as XY-modules). Each bar is 0.96 cm wide and high, and 1.8432 m long[3]. In FGD1 (further upstream of the beam), there are 15 such layers. In FGD2, there are 7, with 6 layers of target water in alternating layers. The purpose of the water panels is to provide a relative measurement of the cross-sections in plastics scintillator and water, which allows event rates measured in the ND280 detectors in plastic to be compared to the events occurring in water at SK.

1.4.1 FGD Optical Geometry

The FGD scintillator is arranged as a set of hanging XY-modules, with alternating direction, as in Figure 1.4. Each scintillator bar is threaded with a Kuraray Y11 (200) S-35 wavelength shifting (WLS) fiber which acts to collect scintillation light released in the bar from traversing particles. Adjacent WLS fibers are threaded and read out on opposite sides of the detector, collecting and channeling light produced in the scintillator bars. The WLS fiber connects to a plastic coupler (referred to as the “Kyoto Coupler”), which when inserted into a matching piece secures the WLS fiber to an MPPC photo-sensor. The MPPC and coupler complex is itself secured to a daughter card. The daughter card serves as a structural component as well as an electrical component. Each daughter card is in turn affixed to a bus-board with 15 other MPPCs. A close up of this can be seen in Figure 1.5. Visible in this figure is the aluminization of the ends of each fiber, which reflects light from the end of the fiber without an MPPC to increase the number of light intensity. Also visible is an LED placed at the end of each fiber (on the far end from read-out) that can be used in principle for light injection studies. This is discussed further in the light pulser section.

The properties of the wavelength shifting fiber are important for the purposes of this analysis. Particularly of interest, the decay time for absorbed light in the fiber which is about 7 ns, with an absorption wavelength of 430 nm at peak, and an emission wavelength at 476 nm at peak[3]. These wavelengths were selected to match well with the scintillator emission wave-

1.4. The Fine Grained Detector

length, and the MPPC response (which has a peak response wavelength of 400 nm[17]). Studies of the saturation behavior of the fiber-MPPC complex must try and match this behavior.

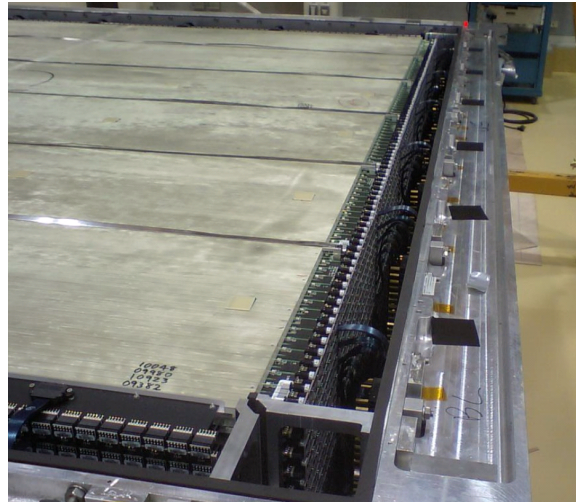


Figure 1.4: The uncovered FGD in a horizontal position. The scintillator panels can be seen in the center of the image, and the MPPCs attached to the black daughter card and bus-boards seen in black surrounding the scintillator layers.(Permission pending)

1.4. The Fine Grained Detector

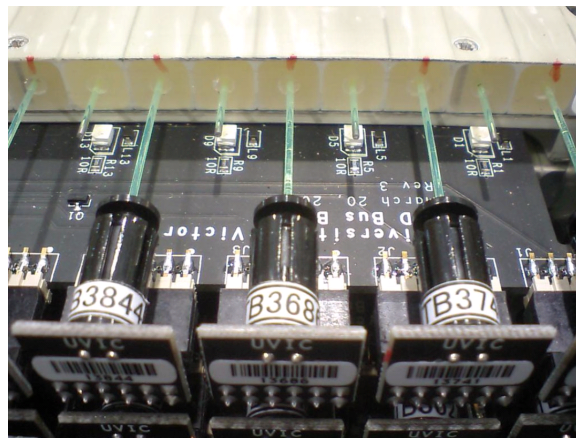


Figure 1.5: The end of a scintillator panel, illustrating the connection of WLS fibers to MPPCs, as well as the optical interfaces between LEDs for light injection and WLS fibers. WLS fibers can be seen in green connecting the the black cylindrical Kyoto coupler (within which is the MPPC). The three Kyoto couplers connect to three daughter cards, seen at the bottom of the photograph in black, labeled with “UVIC”. The LEDs can be seen as small white squares underneath every second WLS fiber.(Permission pending)

1.4.2 FGD Electronics

The FGD electronics are responsible for control of the FGD detector. This means they must be able to collect data from 8448 MPPCs, filter out extraneous information, monitor ambient conditions, and maintain the electrical conditions necessary for MPPCs to function correctly[3]. Broadly, 16 MPPCs are connected to a bus-board and up to four bus-boards can be read out by a single Front End Board (FEB). Each signal goes through a voltage divider to create two channels with different resolutions and dynamic ranges before being fed into a switched capacitor array (SCA) for analog to digital conversion. Each element in the array measures the current through the MPPC for a 20 ns time bin. The FEB also provides the voltage necessary to maintain each MPPC in Geiger mode. This process is done constantly, and when the system is instructed to trigger (or self-triggers), the FEB receives a signal from the Crate Master Board (CMB), and reads out the SCA. Data is then routed to the Data Compression Cards (DCCs), each of which reads out four CMBs. There are 6 DCCs for each FGD. This hierarchy is shown in Figure 1.6.

The digitized output from the 508 time bins (at 20 ns apiece) formed by the charge on each capacitor in the array are then passed to the CMB which filters data as necessary to achieve the required per-event data rate. This filtering typically throws away regions of waveforms where no light is observed, or where it is below some threshold near the noise level. In the work presented in this body, no filtering is needed or applied. Additionally, each FEB produces an analog sum (ASUM) of the signals it receives (1 per

every 8 channels), and the FEBs in a crate forward these to the CMB. If the sum of ASUMs is above a certain threshold, the detector can self-trigger. This allows the FGD to trigger on cosmic rays, as well as trigger other detectors.

The Front End Board

The FEB contains 2 Application Specific Integrated Circuit (ASIC) chips[3], each able to read out two bus-boards of 16 MPPCs. Four FEBs are inside each mini-crate of FGD1, and two are inside each crate of FGD2. Each MPPC is segregated into two channels by a voltage divider into a high and low attenuation channel. The circuit responsible is shown in Figure 1.7. The high and low attenuation channels are separated by a voltage divider, and achieve a ratio of about 8.5.

Each MPPC is held at a voltage drop relative to a primary charge pump. The maximum such difference allowed by the DACs is 5 Volts, hence each MPPC has a voltage:

$$V_{MPPC} = QPump_{FEB} - TrimDac_{MPPC} \quad (1.5)$$

where $QPump$ is the voltage across the primary charge pump, and $TrimDAC$ is the specific bias applied to each MPPC on top of the charge pump. The voltage applied by the $QPump$ is measured in nine different ways. One measurement with a large digital error is performed on the MSCB processor. The MSCB processor (MIDAS Slow Control Bus) is a specialized com-

ponent which monitors and controls certain conditions in the experiment, including temperature and voltage. Eight other measurements of voltage are performed by a separate ADC chip. Without external calibration the ADC chip would introduce a 0.1 to 0.2 volt error. The voltage applied to an MPPC is calculated as the average of the central 6 measurements of the high-precision ADC chip after they have been calibrated.

As the data taken during this work was partially done with an uncalibrated board, the specific conversion between DAC and voltage was initially unknown. It was therefore necessary to retroactively apply the measured calibration which was ultimately applied to this board when it was placed inside the FGD. Data taken during 2010 was performed on a different FEB which was already calibrated. Almost all figures, and all results in this work depend on data from 2010.

The Light Pulser Board

In addition to electronics for controlling the MPPCs and collecting data, there are a set of LEDs situated on the end of the fiber opposite the MPPC. This allows a systematic method for injecting light into the fibers for calibration and gain-monitoring. The LEDs are controlled by a set of Light Pulser Boards (LPBs). Each LPB controls the LEDs for an entire mini-crate, and is able to selectively activate one quarter (or half, or three-quarters, or all) of the LEDs on a bus-board, with every fourth LED firing in the first case. Additionally, the intensity and duration of the pulse can be controlled. Both the intensity and the pulse width must be calibrated to the amount of light actually produced. This is made more complicated by the presence (in er-

ror) of an inductor in series with each diode, such that the time structure and intensity is difficult to predict and control.

There are three primary modes of operation for the LPBs in the detector. They are to produce low level light (3 to 10 photo-electrons), high level light with MPPC saturation (greater than 400 photo-electrons), and stable light somewhere in the linear region of the MPPC above the dark noise (between 10 and 100 photo-electrons). The first role will allow us to study the linearity of the gain of the MPPC, in a region which can be difficult to access with cosmic rays, whereas the second will allow us to study the effect of saturation on the MPPCs, as well as electrical effects in the boards. The last roll is intended to provide a means of measuring the gain stability of the FGDs. While all these roles were intended during design, the ultimate capabilities of the LPBs installed in the FGDs remain to be seen. The saturation calibration may ultimately be reproduced on the entire detector using these devices.

1.5 Software Overview

In addition to understanding the optical and electrical aspects of the detector, a brief understanding of the software algorithms used for identifying output from the MPPC is necessary. A series of 508 time bins, each with an ADC count, is processed by a pulse-finder which looks for avalanche shapes in the voltage from each device. The software pulse-finder augments hardware filtering and pulse-shaping present in the AFTER ASIC on the FEB[8]. The pulse-finder works by looking for regions of increasing ADC

counts in the waveform, followed by regions of decreasing counts. The rising height from baseline and falling height to baseline are summed (to remove noise, which is less likely to return to a baseline value), and compared to a threshold. This cutoff removes pulses below approximately 15 ADC counts, depending on the threshold value to eliminate false signals from electrical noise. This analysis uses a threshold value of 30. The pulse-finder is cited as having an efficiency of $98.4\% \pm 0.4\%$, and a misidentification rate of $0.8\% \pm 0.3\%$ [24]. However, the pulsefinder is sensitive to gain, and as a result the efficiencies become sensitive to the bias voltage applied to the MPPC. The pulse finder also has difficulty identifying pulses which closely follow other pulses. This results from the downward distortion of pulse heights as far as 30 time bins(600 ns) from an initial pulse (30 time bins is between 1 and 2 pulse widths). The effect on efficiency is particularly hard to study, and this is a major limitation of this work.

1.6 The MiniFGD Analysis

The purpose of this work is focused on understanding the saturation effects of the MPPC which occur at high light level. The MPPC must be understood not only on its own, but also within the context of the electronics in the FGD, the optical coupling, fibers, and scintillator bars we use. This is accomplished by using the MiniFGD - a scaled down version of the FGD with two mini-crates, which is used for software development, hardware testing, and external beam tests at TRIUMF. The saturation effects are studied by injecting short pulses of light at 405 nm into the MPPC directly (Figure 1.8)

and indirectly via the the Y11 fiber (Figure 1.9). Laser pulses are produced using the Hamamatsu Picosecond Pulser, model C8898, with a 405 nm head with peak power 123 mW, and pulse width of 84.4 ps. A digital attenuator, model DA-100 from OZ Optics, is used to vary the intensity in a predictable fashion.

The general calibration scheme to measure the saturation effects of the MPPC is studied by exposing the MPPC to a wide range of laser intensity at very short time intervals. This analysis uses the fact that laser pulses arrive within a 200 ns period of time relative to a trigger to the SCA to read out data. In order to understand the conditions in the FGD better, this is studied both as a direct exposure of the MPPC to laser light, and also through exposure to the wavelength shifting fiber which is then coupled to the MPPC. Several fibers and MPPCs are studied. Data is collected with multiple MPPCs and fibers. For each MPPC and fiber used, up to 9 voltage values are selected, and an intensity scan performed over the range 0 to 40 dB (typically with a 1 dB step size). Each intensity-voltage combination is referred to as a run. The entire analysis chain is shown in 1.10.

The analysis proceeds by first establishing two independent methods of measuring light exposure from the MPPC while compensating for the dark noise intrinsic to the device. These measurements differ in that one (referred to as the mean analysis) is sensitive to the total charge output of the device (including cross-talk and after pulsing). The mean analysis counts the number of avalanches (NAva). The other (referred to as the Poisson analysis) measures the basic quantum efficiency of the device to photons and is in principle not sensitive to after-pulsing and cross-talk. The Poisson

analysis is said to work in the number of photoelectrons (NPe). The Poisson analysis is then correlated to a set of power-meter measurements which are linearly related to true light intensity. We have thereby created a scale set to have units which match the linear regime of the MPPC (where saturation effects of the MPPC are believed to be under 1% until 6 photoavalanches). The plots which establish this scale are referred to as correlation plots in the body of work. Because the Poisson analysis has statistical limitations that only allow it to work at low light level (when the probability of the detector measuring no light is greater than about 0.1%), it must also be related to the mean analysis which is able to work across the entire range of the device. This process is described in chapter two.

The analysis proceeds by applying a gain conversion on all pulse heights from the high attenuation channel to make it equivalent the low attenuation channel. This is necessary a pulse with more than 80 PE will typically saturate the ASIC low attenuation channel. As a result much of the useful data is actually in the high attenuation data. This saturation is distinct from the MPPC saturation in that it is a digital effect in the electronics rather than a loss of optical sensitivity.

Next, a charge histogram is created by using all pulse heights in a given running setting. In our analysis, the pulse height is used as a proxy variable for the charge, which would be better described by the area under the pulse. This method is not used because it is less robust to noise and complicated pulse shapes. The pulse height is also used in this fashion in the FGD analysis software. By fitting a Gaussian distribution to the first peak of the charge histogram built on areas of the waveform not affected by the

laser, a conversion between ADC count and photo-electrons is achieved. This is referred to as the one photoelectron pulse height (1PEPH). This is done by using the 80 or 250 (depending on the run) time-bins prior to any possible laser activity as an “undisturbed region”. This is valid as the recharge period of the MPPC is typically in the order of nanoseconds to microseconds, whereas the laser repeat period is 5 ms to 10 ms.

A two-dimensional histogram is built to produce a conversion between the high and low attenuation channels (the HiLo conversion). The plot consists of the pulse height values of the low channel and the high channel for each pulse individually. The data for this histogram is gathered from the region of the waveform containing laser pulses, and is amalgamated over all intensity setting, but at a single voltage value. This conversion is established over a region where neither channel has saturated its ADC, and the ratio of charge in the two channels is extrapolated to regions where the low channel is partially or fully saturated.

A voltage scan is used to identify the break-down voltage of the MPPC, and provide a measurement of OV for any given run. Voltage scans are performed by setting the voltage of the MPPC to values between 67 and 71 V, and identifying the intercept of the 1PEPH on the voltage axis. The voltage scan process, the ADC to PE and HiLo calibrations are described in Chapter Three.

These three pieces of information allow the construction of a saturation curve for the MPPC: a plot of the number of avalanches as a function of light intensity. For a given curve the voltage scans allows us to know what OV was present at the time. This can be used to construct a calibration for

1.6. *The MiniFGD Analysis*

removing the effects of saturation at any given OV range. The calibration is constructed by parametrizing the number of avalanches as a function of light intensity. Error estimates for these parameters are performed in Chapter Four.

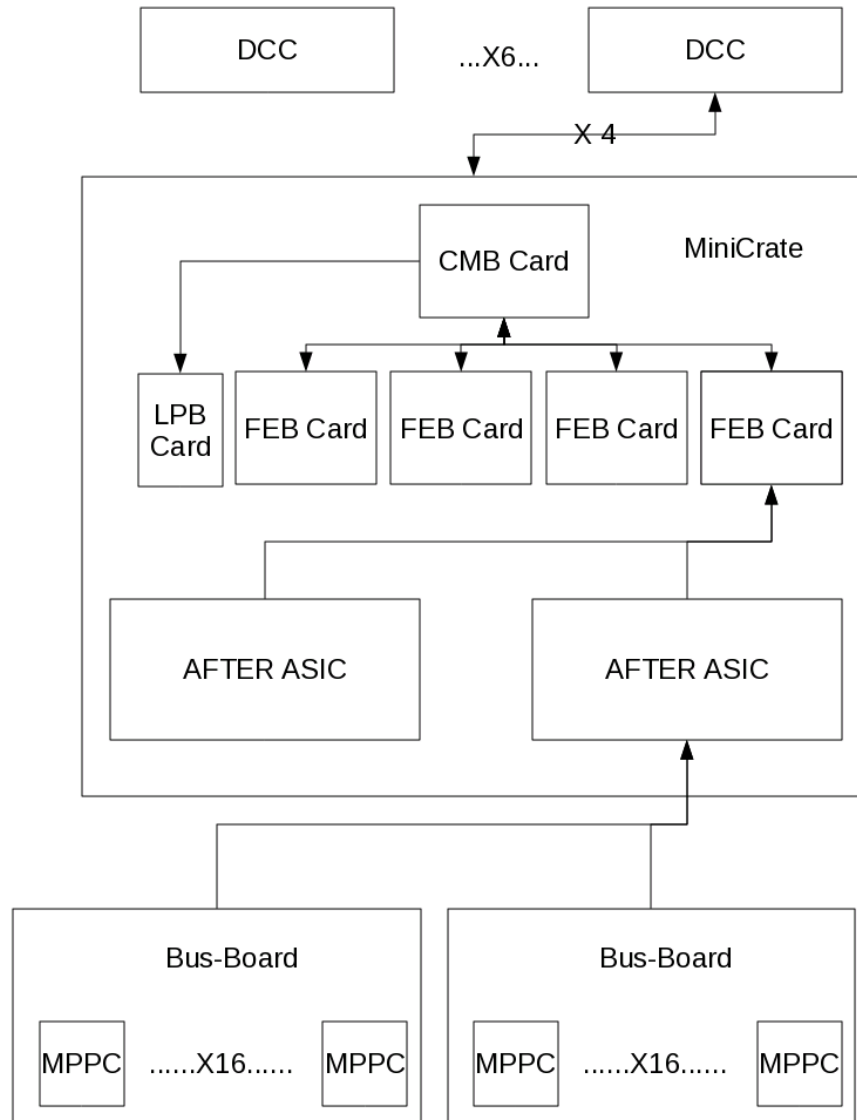


Figure 1.6: The relationship between different electrical components is shown for one FGD.

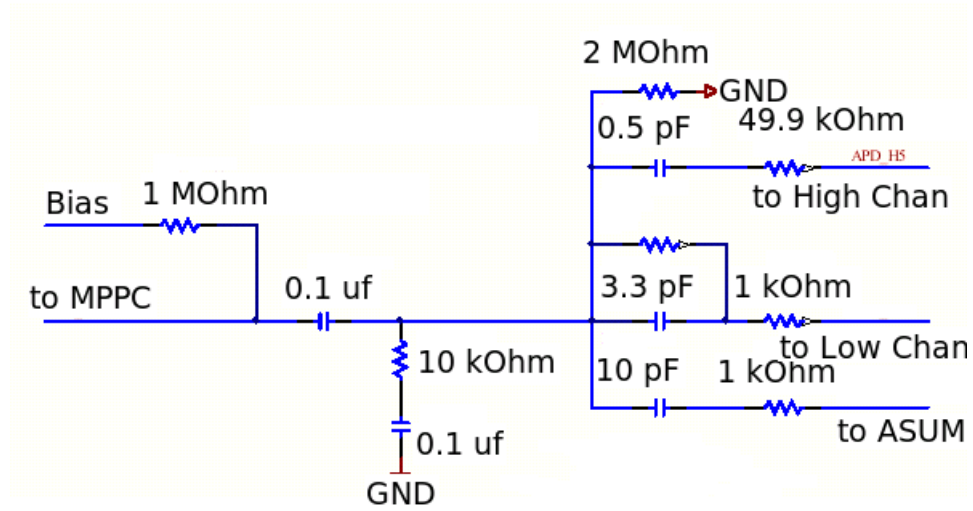


Figure 1.7: The voltage divider, ASUM, and bias circuitry are shown in this figure. The bias is the voltage line which holds the device at high voltage. Taken from the FEB Schematics[9].(Permission pending)



Figure 1.8: A photograph of the MPPC coupler which allows an FC cable to couple directly to an MPPC attached to a daughter board.

1.6. The MiniFGD Analysis

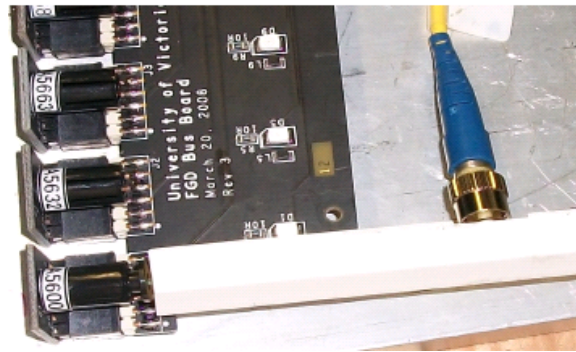


Figure 1.9: A photograph of a Y11 fiber being directly exposed to light from the laser fiber.

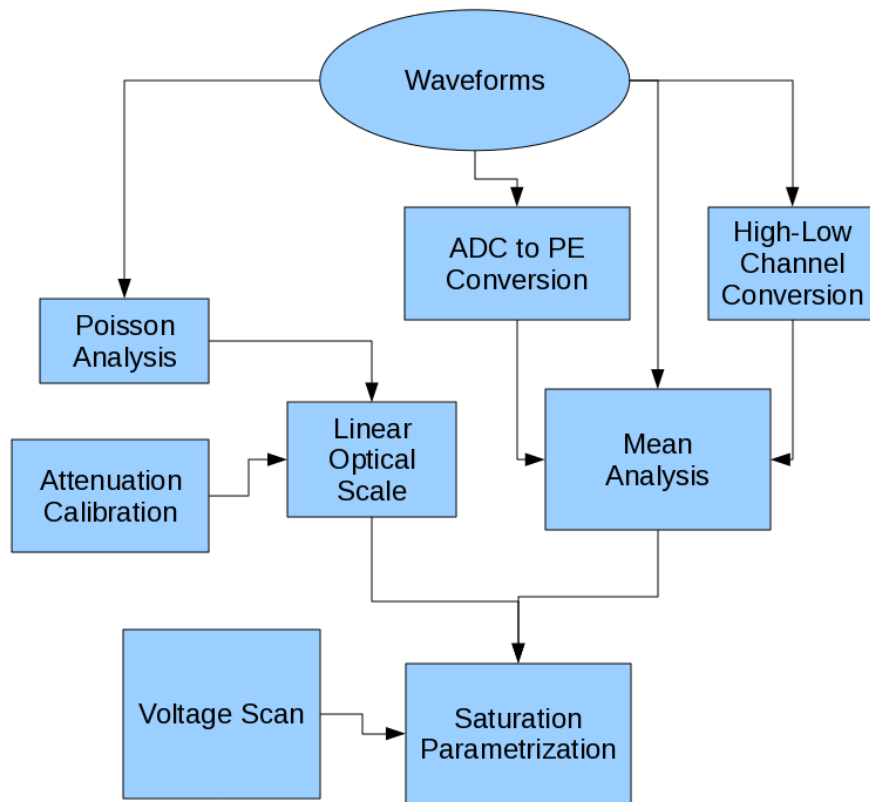


Figure 1.10: This flow chart illustrates the dependencies between different stages of the analysis. The ADC to PE conversion and HiLo conversion are in particular in common (although implemented independently) with the full FGD analysis software.

Chapter 2

Optical Equipment and Linear Optical Unit Construction

This chapter discusses the use of a laser and digital attenuator(DA) to produce a linear light source, and the process of calibrating that source.

2.1 The Poisson Analysis Method

The probability of firing a pixel firing when a photon is emitted from the laser can be modeled as a binomial process. For large numbers of trials with relatively low probability of success, the number of fired pixels can be modeled as a Poisson distribution. This approximation can be justified by noting that while the particle detection efficiency(PDE) of the MPPC is not small (We expect it to be between 10% and 30%, but never explicitly measure it) the total probability of success of the entire system including optical attenuator and coupling is infact very small. Given this approximation, we now have a Poisson distribution of the probability of a number of pixels

2.1. The Poisson Analysis Method

firing:

$$P(k, \lambda) = \frac{\lambda^k e^{-\lambda}}{k!} \quad (2.1)$$

Where P is the probability for a k photons to fire a pixel when the average number of pixels firing at this illumination is λ .

The distribution can be distorted in the case where one or more pixels are fired by a single photon due to the effects of cross-talk and after-pulsing. The after-pulsing fires do not occur simultaneously with the main avalanche, but from the perspective of our electronics may occur too closely to distinguish. These effects, however, do not change the chance of zero pixels firing.

$$P(0, \lambda) = e^{-\lambda} \quad (2.2)$$

With this, we can calculate the probability of no pixel firing in any given time bin. This is the probability of no dark noise pixel fires multiplied by that of no optical pixel firings (whether from the laser or otherwise):

$$P(\text{No Pixel Firing}) = P(\text{No dark noise}) \times P(\text{No Optical Fires})$$

$$P(0, \lambda) = P(\text{No Optical Fires}) = \frac{P(\text{No Pixel Fires})}{P(\text{No darknoise})}$$

Thus our average signal, λ , is the number of photoelectrons (NPe):

2.1. The Poisson Analysis Method

$$\lambda = -\ln\left(\frac{P(\text{No Optical or DN Firing})}{P(\text{No darknoise})}\right) \quad (2.3)$$

In practice, counting the number of zeros is accomplished by sampling from different parts of the same waveform outputted by the MiniFGD. In Figure 2.1, the red area (right) contains the laser pulse and is sampled for no optical or dark noise fires, and the blue for just no dark noise fires. The dark noise can be sampled before the expected optical area, lessening cool down effects (such as long after pulsing) from large laser pulses.

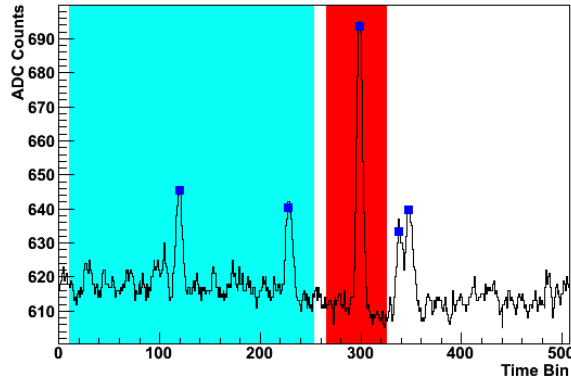


Figure 2.1: A comparison between two different regions of the wave form is used in order to measure the pixel fires from optical sources (in red, right), and measure background from dark noise (the region in blue). Typically dark noise measurements are performed before the optical source gate to prevent long after-pulsing from biasing the measurement.

The probability of no pulses being observed in each gate is determined as the fraction of events in which no pulses occurred. Error analysis on this accomplished as follows. We assume there are two Poisson processes,

2.1. The Poisson Analysis Method

one governing the probability of observing dark noise in the noise sample gate, and another governing the probability of observing either dark noise and optical pulses during the laser illumination gate. Further, the chance of observing some number of zeros is governed in both cases by a binomial process dictated by each case's Poisson distribution. To calculate the error of the mean of a binomial distribution which governs the number of zeros observed, we calculate the variance as:

$$\sigma_{binomial}^2 = N_{trial}P_{obs}(1 - P_{obs}) \quad (2.4)$$

where N_{trial} is the number of events sampled, and P_{obs} is the probability as inferred from the number of zero events seen during N_{trial} events. The error on this quantity is then:

$$\delta_{Zeros,binomial} = \sqrt{(\sigma_{binomial}^2/N_{gate})} \quad (2.5)$$

$$= \sqrt{\left(\frac{N_{trial} \frac{Zeros_{obs}}{N_{trial}} \left(1 - \frac{Zeros_{obs}}{N_{trial}}\right)}{N_{gate}}\right)} \quad (2.6)$$

$$= \sqrt{\left(\frac{Zeros_{obs} \left(1 - \frac{Zeros_{obs}}{N_{trial}}\right)}{N_{gate}}\right)} \quad (2.7)$$

$$(2.8)$$

Here $Zeros_{obs}$ is the number of zeros observed in the gate and N_{gate} is the number of gates (separate parts of the waveform) we choose to average over to produce the estimate of zeros. In the case of the laser there can only be

2.1. The Poisson Analysis Method

one gate (where a gate is a fixed region of the waveform used for analysis), however in the case of the dark noise samples there can be as many as 40 gates by tiling the area in front of the laser gate with sampling gates. This can take up a great deal of memory, so typically at most five are used. The error in λ is now calculable as:

$$\delta\lambda = \sqrt{\left(\frac{\partial\lambda\delta_{N_{zerosDN}}}{\partial N_{zerosDN}}\right)^2 + \left(\frac{\partial\lambda\delta_{N_{zerosOptical+DN}}}{\partial N_{zerosOptical+DN}}\right)^2} \quad (2.9)$$

$$\frac{\partial\lambda}{\partial N_{zerosDN}} = -\frac{\partial\lambda}{\partial N_{zerosDN+Optical}} = \frac{1}{N_{zeros}} \quad (2.10)$$

In principle, a more complete error correction could be employed to correct for the efficiency of the pulse-finder. Because the efficiency of the pulse finder is presently poorly determined, we typically derive the Poisson analysis equations with the assumption that the pulse-finding efficiency is 1. The effect of this assumption cannot be studied without knowledge of the response of the pulse-finder to complicated patterns of pulses. The efficiency of the pulse finder is difficult to estimate at low gain, or in the region after another pulse. This introduces a systematic uncertainty to the analysis which is difficult to quantify.

The Poisson analysis is expected to be strongest when there are even numbers of empty waveforms and non-empty wave forms. Below this level our sensitivity is limited by dark noise, and above this level the small count statistics on the number of zeros limits our sensitivity. The number of expected non-empty waveforms from optical fires drops below the typical

2.2. *Constructing The Linear Optical Unit System*

number of events measured in between 5 and 8 PE. After this point the method is no longer able to measure light intensity. One difficulty with this analysis is that there are time-shifting data corruption events sporadically throughout the data. These events will introduce artificial zeros in the Poisson Analysis by moving optical pulses to a region outside the gate, while moving a region of background into the gate. This occurs infrequently. If we use high intensity data (which is unequivocal about the location of the optical pulse on the waveform) to quantify its rate, we find about one instance in any given run. The baseline of a waveform (the charge level read from the SCA in regions between pulses) was found to jump discontinuously in events where time shifting had occurred. Waveform veto schemes for rejection of events with large baseline shifts were developed to remove events with characteristic defects. Because the large baseline shifts observed in time-shifted events are not seen as commonly in low intensity events the efficiency of these veto schemes is uncertain. While a small effect, time shifting corruption does limit the sensitivity of the Poisson Analysis. We therefore require that the number of zero events used in the Poisson Analysis be large compared to one for an unbiased measurement by choosing to use a photo-electron range such that the least zeros observed is about 100.

2.2 Constructing The Linear Optical Unit System

In order to quantify the amount of light hitting the MPPC, we could choose to use the definition of attenuation provided by the digital attenuator (ab-

2.2. *Constructing The Linear Optical Unit System*

breviated as DA, OZ Optics unit DA-100). This would provide a scale which is in principle linear with the original light exposure, once the appropriate exponential conversion is made. However, after observing a number of anomalies in the results of this approach which seemed larger than 0.03 dB error expected of the system, we chose to directly measure the output of the attenuator. This undertaking required fully understanding both the laser, and the Newport power-meters 1930-C and 2931-C (with UV heads) used to directly measure the laser output at a fire rate of about 100 MHz (depending on the specific calibration run).

The photo-sensors on the power meter are sensitive to the ambient temperature. Figure 2.2 shows the drift in baseline of the power-meter, and the temperature during a period of about 30 hours. The baseline values of the power-meter are the result of dark current in the silicon based detectors, and are measured with the sensors in a dark box and the laser turned off. From these data it is clear one must control or carefully understand the temperature in order to have results which are meaningful at low light intensity - a regime necessarily explored by a device that operates over four orders of magnitude in optical intensity.

The calibration of the DA consists of setting the requested dB to each value used during our studies (Values 0.0, 0.5, ..., 40) and measuring the resulting output of the power meter. A run collected in the LADD area of TRIUMF is shown in Figure 2.3. After collecting and analyzing this scan, it became apparent that the dark-current is sensitive to temperature. The temperature sensitivity of the LADD laser data is shown in Figure 2.4. It is apparent from this data that the laser power is also sensitive to temperature

2.2. Constructing The Linear Optical Unit System

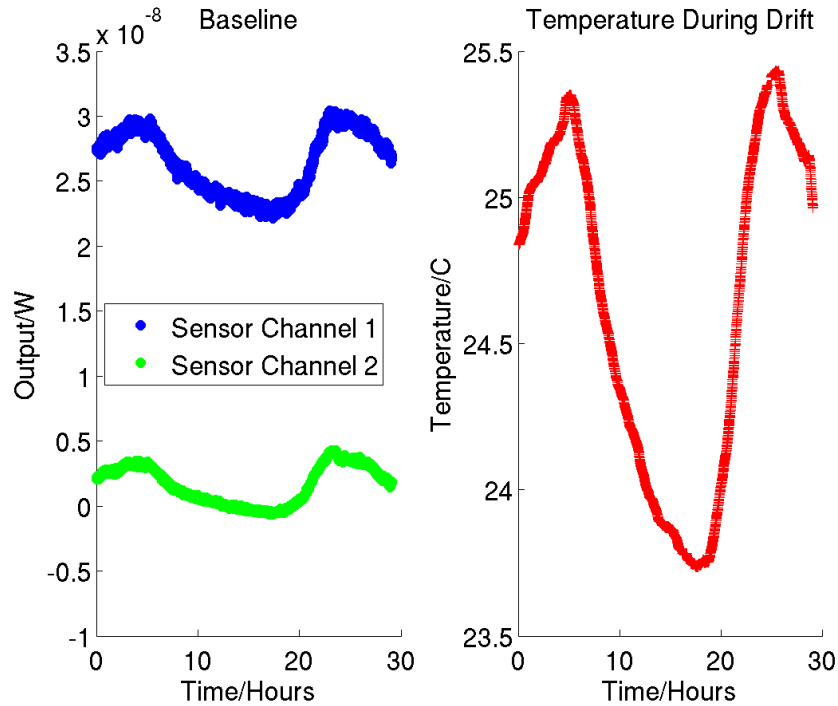


Figure 2.2: The left panel shows the output of the power-meter’s two channels (using the 2931C PM), and the right plot shows the temperature simultaneously. The strong correlation is the result of the dark-current’s dependence on temperature.

Because of our dependence on the stability of the laser system, this is a serious issue. Over time, this drift can be responsible for a 20% or more change in laser intensity.

Given the sensitivity to temperature in both the emitting as well as measuring device, another measurement of this process was performed inside the Micro-structure Lab’s clean-room. The stability of the laser system and the room temperature are shown in Figure 2.5. The calibration measurement from Figure 2.3, as well as the clean room measurements for both attenuator

2.2. Constructing The Linear Optical Unit System

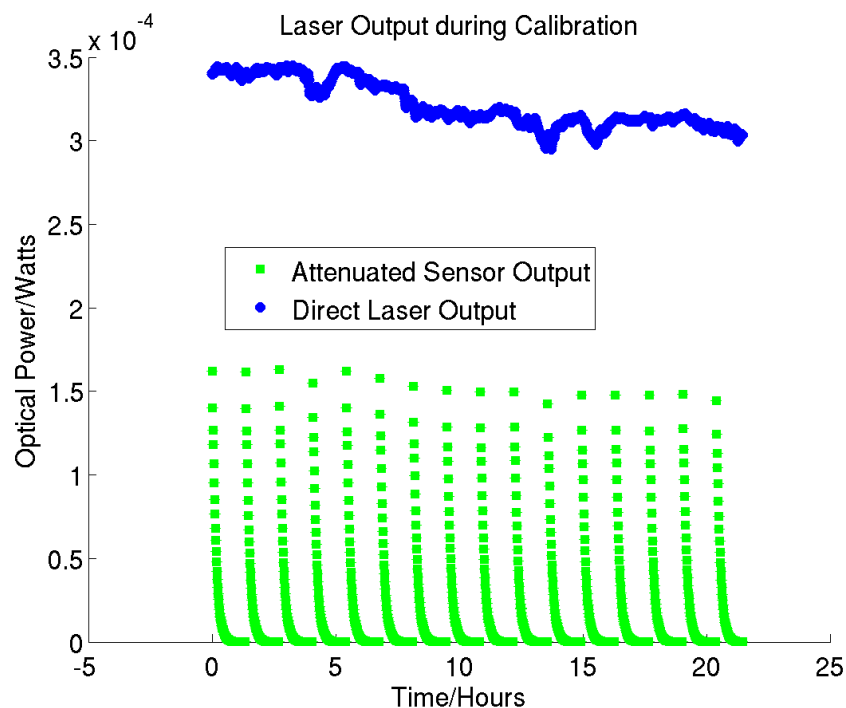


Figure 2.3: This diagram shows the attenuated channel in green, and the non-attenuated (direct) laser intensity in blue. The variation in the laser intensity can be seen to clearly have an affect on the data in the attenuated channel over the course of the repeated measurements. Not visible at this scale is the relationship between temperature and the zeroing observed in the green channel at high attenuation.

units used are included in Figure 2.6 on a log scale.

2.2. Constructing The Linear Optical Unit System

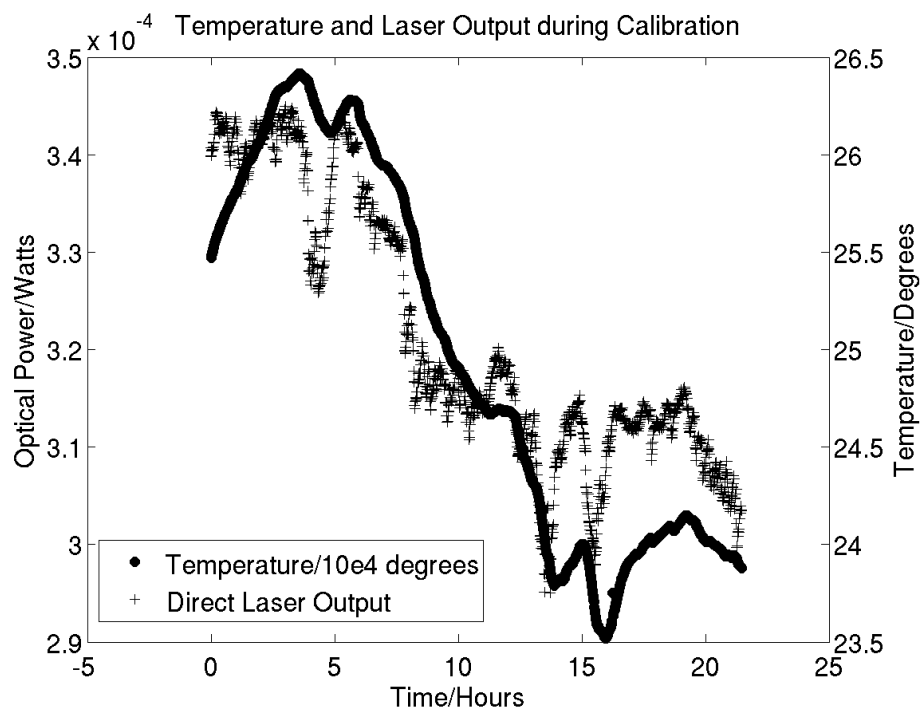


Figure 2.4: This diagram shows the temperature in solid circles and the non-attenuated (direct) laser intensity in crosses. The direct dependence between laser intensity and temperature is clearly seen. Examining the position of minima in the two curves suggests that there is a time lag between them.

2.2. Constructing The Linear Optical Unit System

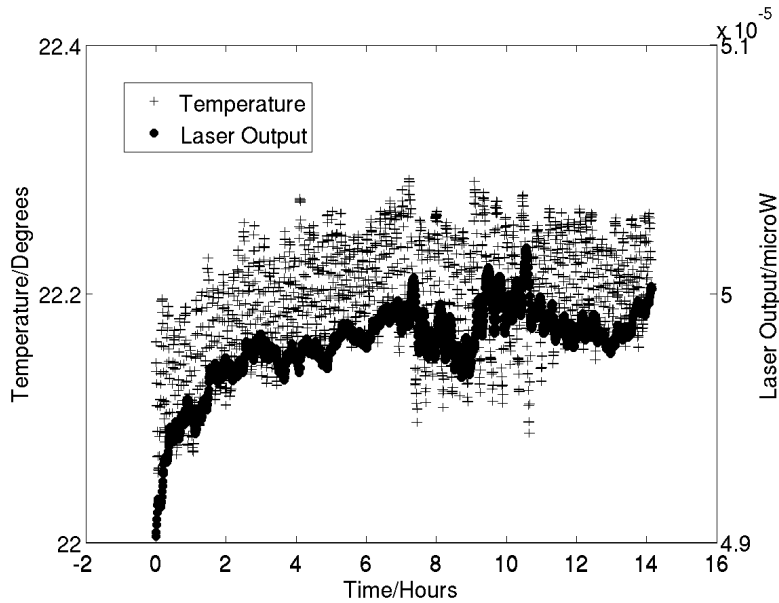


Figure 2.5: The temperature (as measured by the power meter itself) stability is demonstrated to be approximately 0.25°C . The periodic oscillations in the laser output seen are traceable to variations in temperature, and are most likely the result of an air-conditioning unit triggering.

It is now possible to calibrate the attenuator with an accurate power-meter in a temperature controlled environment. By definition of the unit dB, the log-graph of the intensity of the laser/attenuator system should have a slope of about 0.23, and should be strictly linear. To test the built-in calibration, we can fit the logarithm of the data and find the residual. This is shown in Figure 2.7. The non-linearity in attenuator #2 (serial number 86971-02) is clearly visible between 9.5 and 11.5 dB. Unfortunately, at the time this calibration was complete enough to see this, substantial data was already taken using this device - and as such, it is necessary to post-calibrate to remove the effect. It can be seen that the linearity defect is of the order

2.2. Constructing The Linear Optical Unit System

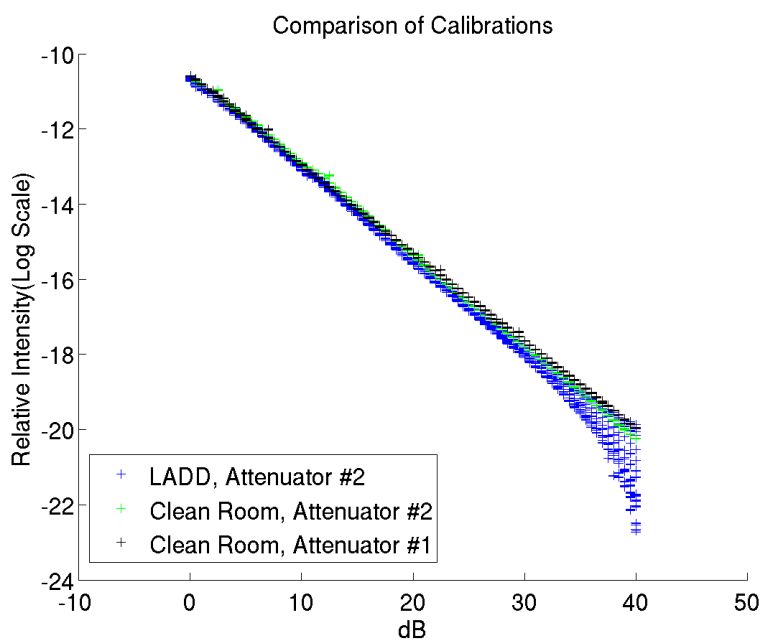


Figure 2.6: The calibrations for two DA units are shown in log scale (DA #1 was used for comparison, but was not used in measurements which follow). The blue points show the effect of additional noise in the measurements at low intensity, and are traceable to the temperature shifts during those runs. The green points are taken with the same attenuator, but in a more temperature stable environment.

2.2. Constructing The Linear Optical Unit System

of 10%. While it is not clear what is causing it, one can hypothesize that it is related to a problem with the gearing in the DA itself. An additional effect seen in both devices is a non-linearity between 0.0 and 1.0 dB. This is expected because the extra space traveled by a gear system when reversing direction will cause an inaccuracy at any turning point. With this in mind, all measurements were done consistently such that settings were done by monotonically increasing the attenuation from 0 dB.

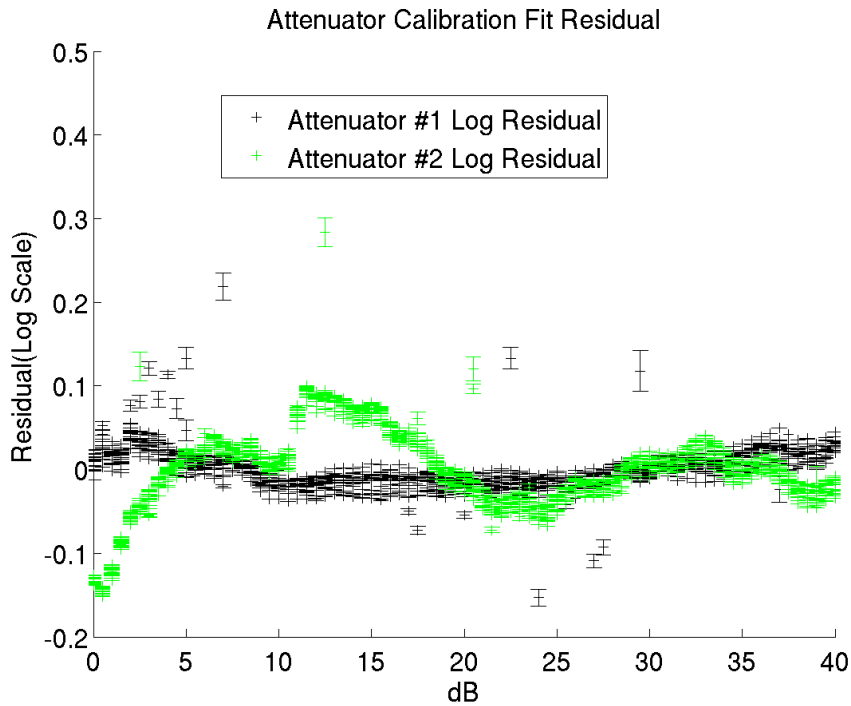


Figure 2.7: This diagram shows the non-linearities in the DA-100 unit #2, when compared to unit #1. Variation is not due to statistical error, but rather temperature and other non-reproducible variables.

While these measurements were performed, we were also able to produce

2.2. Constructing The Linear Optical Unit System

a measurement of the sensitivity of the laser system to temperature shifts. This is complicated by two factors: the power meter temperature sensor is located in a different location and different thermal mass than the laser, and the laser itself is equipped with a Peltier cooler to reduce this variation. We can easily remove the linearly varying component, but higher order terms will remain. Additionally, due to the factors listed above, the temperature change as measured by the sensor and the effect of that change are delayed by approximately 40 minutes relative to each other. Having taken this effect into account by finding the maximum correlation between the laser output and the temperature sensor reading (see Figure 2.8), we perform a linear fit to estimate the removable component, and find that it is approximately 4.1% per degree, or $13.3 \mu\text{W}/\text{degree}$. The fit, along with the shifted and unshifted values are shown in Figure 2.9.

We have chosen to work with a DA unit with a relative calibration. This allows us to control the relative intensity in a well-defined fashion. However, this choice means that we can't know the real photon-detection efficiency of the system. To produce comparable plots we choose to work in a natural unit for the detector itself: we calibrate the system relative to the light necessary to see one photoelectron(PE) on average. By creating a conversion between power and PE observed, we then can analyze the MPPCs relative to their asymptotic linear behavior at low light level. This is accomplished by dividing all exposed power values by the mean PE observed per unit change in power (in arbitrary but consistent units).

Figure 2.10 shows this process for three different voltages of 1 MPPC, where the fits are performed between one and three PE, as determined by

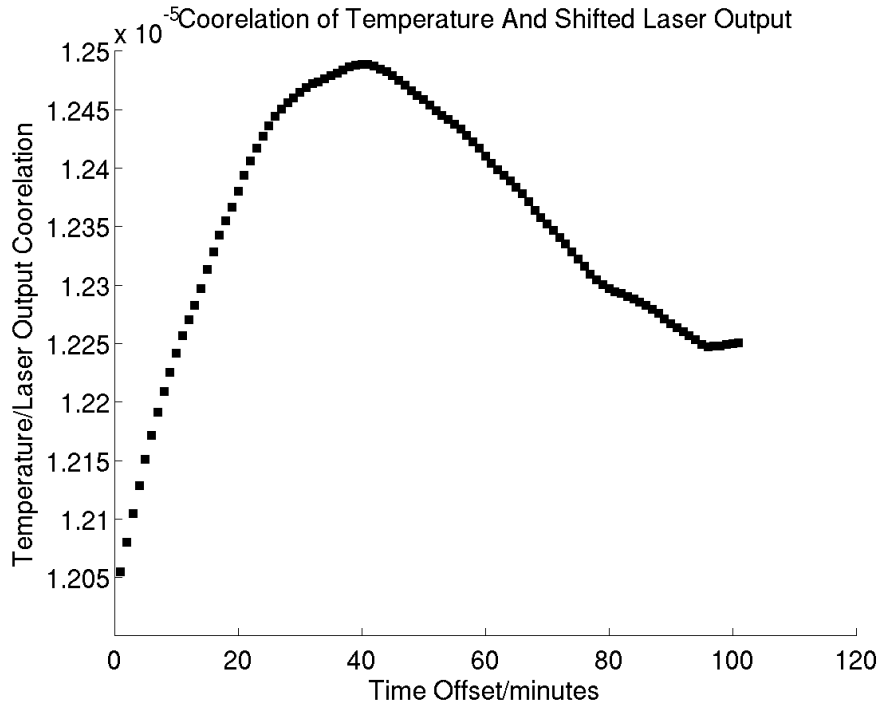


Figure 2.8: This plot shows the correlation between laser output and temperature, as a function of a temporal shift. The maximum correlation is found to be 40 minutes, suggesting that there is a 40 minute delay in the effect of a temperature shift observed at the temperature sensor relative to that effect being observed at the power-meter.

the Poisson analysis. The plots in Figure 2.11 show the residuals of the measured points from the fitted line. The first two plots are take at an OV of 0.76 and 0.90 Volts, whereas the FGD is expected to operate between 0.6 and 0.9V OV. As we approach breakdown, and in particular at any voltages lower then about 0.6 Volts above break down, the behavior of the curves becomes biased against one PE signals. This occurs because the pulse-finder will still be able to identify 2 PE and larger pulses easily, but

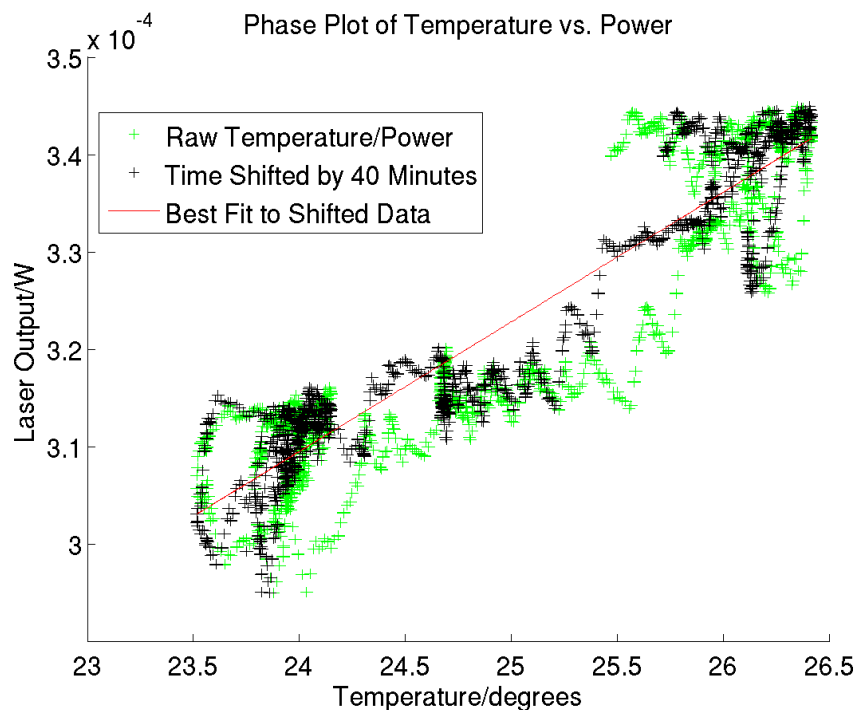


Figure 2.9: This figure shows scatter plots of the laser power vs. temperature, with and without a 40 minute shift. A fit to the shifted data is shown in red. The graphs shows a great deal of structure which cannot be explained by the temperature shifts. This structure is likely partially the result of the the peltier cooler in the laser responding to not just the temperature, but also the rate of change of the temperature.

will have trouble finding 1 PE pulses due to their lower pulse height.

The slope in Figure 2.10 incorporates photon-detection efficiency, which is itself a function of voltage. This has the effect of removing any dependence on photon detection efficiency from the slopes, because it is performed separately for each intensity scan. Patterns in these slopes can then be used to analyze the effect of voltage on PDE. These can be seen in Figure 2.14 and Figure 2.12 for a wide variety of bare MPPCs and fiber based measurements.

2.2. Constructing The Linear Optical Unit System

The trend below 1 PE in Figure 2.11 can be further examined by looking at patterns in the intercepts. Figure 2.15 shows the zero-intercept of the linear fits in Figure 2.10 for both direct optical exposure, while Figure 2.13 shows it for fiber based exposures. A clear bias in the points which are directly exposed can be seen. It's unclear what causes this, but there are two differences in the treatment of these two data sets (which will be discussed further in Chapters Three and Four). The first difference is that the bare MPPCs are run at much lower laser power. Bare MPPCs have many points between 0 and 1 PE, whereas MPPCs exposed through a wavelength shifting fiber are typically exposed to almost none below 1 PE. This difference in laser power was necessary as the efficiencies of the two systems are very different, although the specific ranges ultimately used are sub-optimal due to this difference. Despite this difference, the number of points used in the fit between the attenuation calibration and the fiber data are similar (4 or 5). The second difference is that bare MPPCs are removed from the Kyoto coupler and resoldered to the daughter board via two wires a few inches long. In this process, they are necessarily exposed to substantial heating. It is unclear what effect this may have had on them, but it is possible that it may have damaged the wafer.

The actual construction of our exposed light scale is performed by fitting N_{PE} as a function of power-meter output, and then using the slope to create a new variable, $PE_{exposed}$ which is a unit of light linear with the true number photons exposed, albeit with a unknown constant of linearity. This constant will be a function of both OV and will also tend to absorb effects due to light losses at any interfaces and the irreproducibility of those interfaces.

2.2. Constructing The Linear Optical Unit System

From Figure 2.11 non-linearities would seem to be present in the data. Anomalous results above 3 PE can be explained by poor statistics and a bias due to time-shifting corruption. Below 1 PE, however, it is much more difficult to understand the non-linearities, some possible explanations are suggested in section 3.1. Figure 2.16 shows the relative residuals from the fits in Figure 2.10.

The final light scale is constructed as follows:

$$PE_{Exposed} = PM(db) * Eff(OV) + Noise \quad (2.11)$$

where we have defined PM as the output of the power-meter used to calibrate the DA unit and Eff is the ratio of this power to the number of PE actually observed in the sensor at that OV. A noise term is also included. This term can either cancel uncanceled noise, or compensate for incorrect cancellation. Note that the formula above is fit over the range one to three photo-electrons, while to extract the exposed optical values we plug in the fit values and attenuator settings used. This could not be done with the mean output charge of the MPPC, as it would not be a on linear scale - both cross-talk and after-pulsing are sensitive to the number of available pixels, and hence are not immune to saturation effects. The excess slope would therefore change and the curve would be distorted.

2.2. Constructing The Linear Optical Unit System

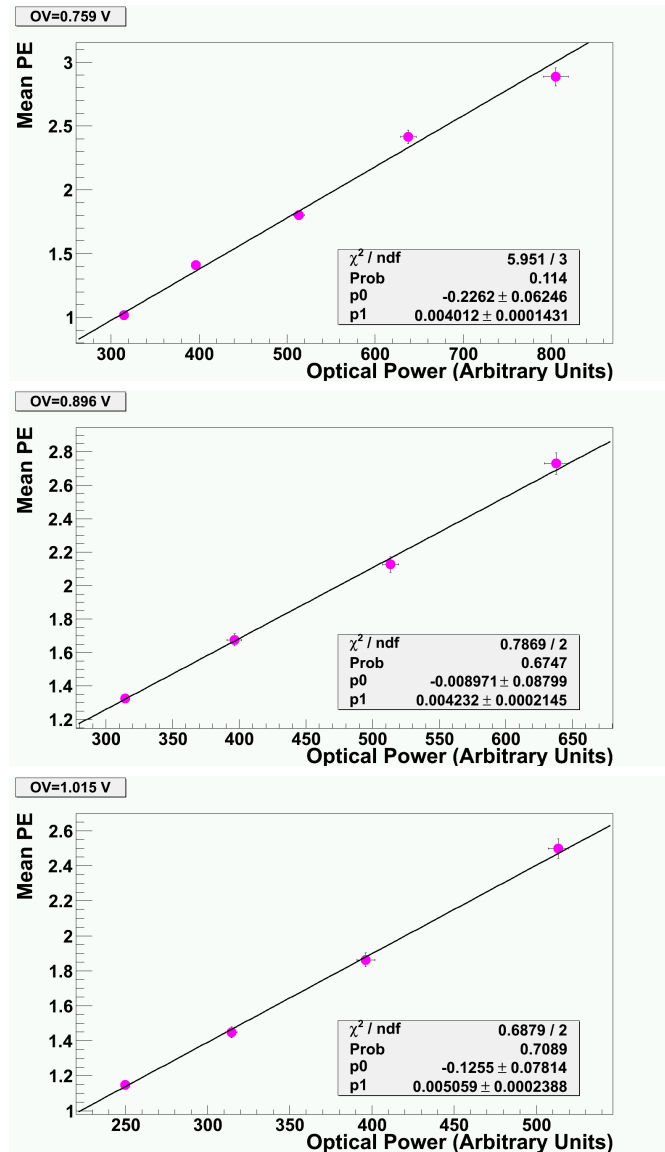


Figure 2.10: The mean PE observed in the MPPC as determined by the Poisson analysis versus the apparent power exposed. The extracted slope defines the optical intensity scale in subsequent measurements. The scans were done at 0.76, 0.90, and 1.01 V OV.

2.2. Constructing The Linear Optical Unit System

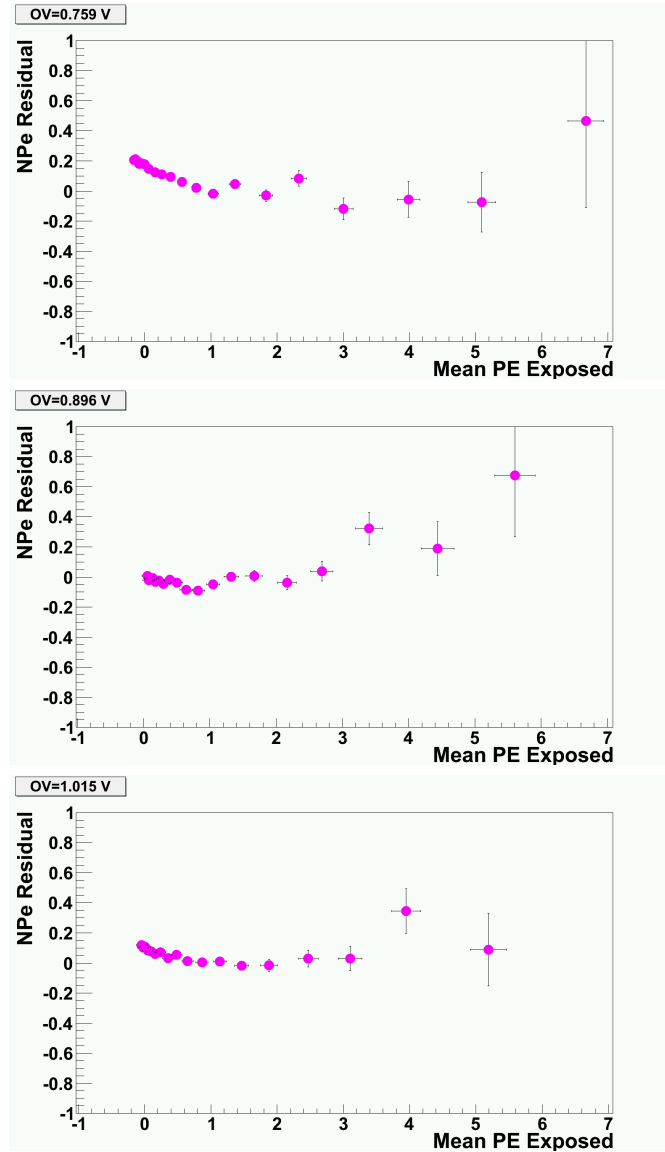


Figure 2.11: Residuals of the correlation plots in Figure 2.10. There are clear trends above and below the fit range used (1 to 3 PE). The trend towards higher values above this range can be understood as being partially the result of time shifting. At 4 PE, there are about 70 zeros in the above plots. At 5 there are only 25. A clear bias must be present in these cases due to the artificial zero introduced by time shifting. Below 1 PE there is a shift upwards, with unknown cause.

2.2. Constructing The Linear Optical Unit System

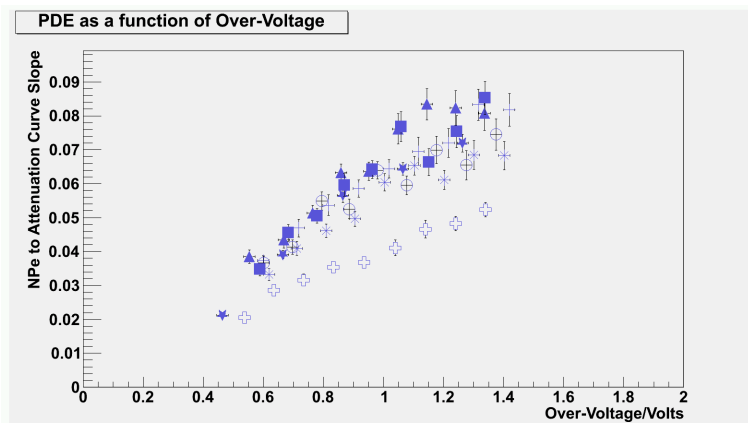


Figure 2.12: This plot illustrates the relationship between optical interface and the behavior of the attenuation calibration slope plots. Different symbols indicate each fiber. Each of these graphs could in principle be rescaled in order produce a measurement of the relationship between voltage and particle detection efficiency.

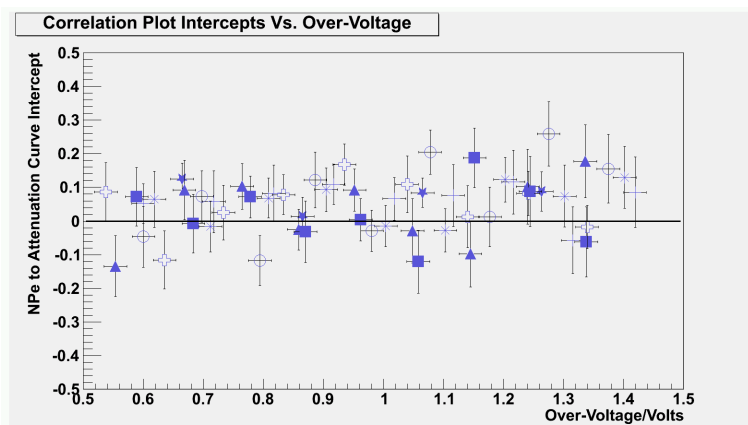


Figure 2.13: This plot illustrates the relationship between optical interface and the behavior of the attenuation calibration correlation plots. Each symbol indicates a different fiber. The plot is centered near zero.

2.2. Constructing The Linear Optical Unit System

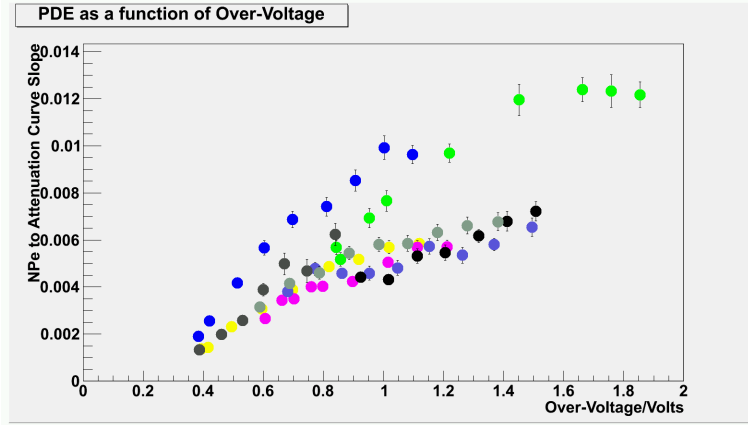


Figure 2.14: This plot illustrates the relationship between optical interface and the behavior of the attenuation calibration slope plots. Each MPPC is indicated by circles of different colors. Bare MPPCs have a much smaller slope due to the lower laser power setting used during exposure. Each of these graphs could in principle be rescaled in order produce a measurement of the relationship between voltage and particle detection efficiency.

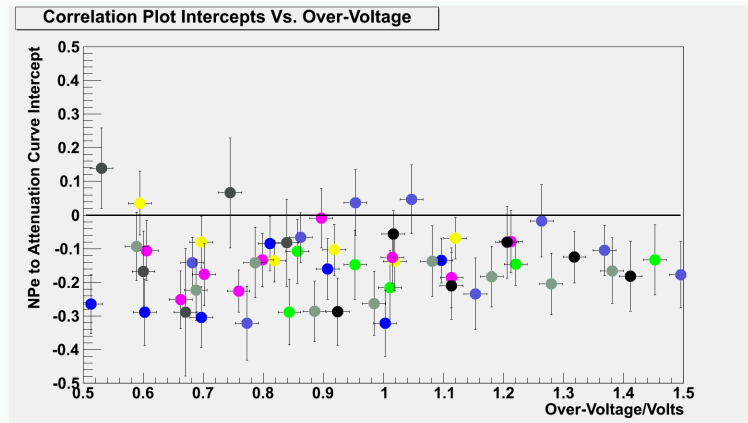


Figure 2.15: This plot illustrates the relationship between optical interface and the behavior of the attenuation calibration correlation plots. Bare MP-PCs are indicated by different colored circles. The bare MPPCs are clearly biased below zero.

2.2. Constructing The Linear Optical Unit System

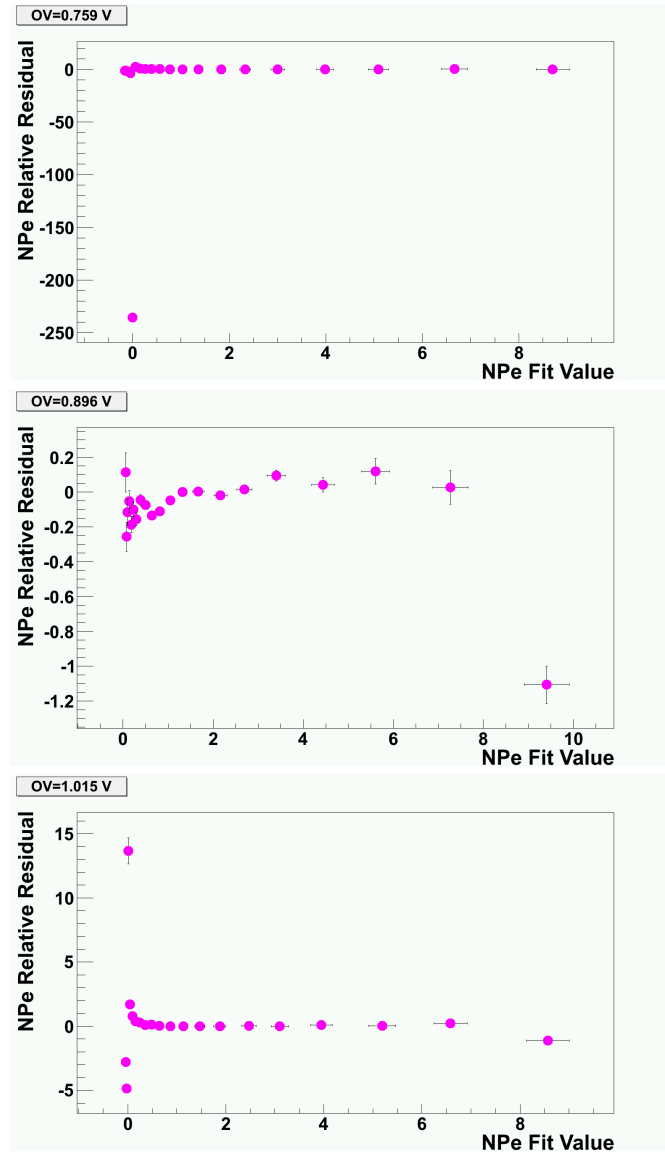


Figure 2.16: This plot shows the relative residual of the above plot, normalized by value of the fit at each point. The asymptotic behavior is the result of the non-zero intercept of the fit line.

Chapter 3

Low level Data Calibration

This chapter describes the MiniFGD implementation of the basic calibrations used in the FGD to convert from pulse height to the number of avalanches. The mean analysis provides a conversion from pulse height to a number of avalanches integrated over a gate relative to a trigger (where a gate is a fixed region on the waveform) and averaged over many events. The high-low conversion is used to convert pulse height measurements from the high attenuation channel into units equivalent to pulse heights measured in the low attenuation channel once digital saturation effects make the low attenuation channel unreliable. An ADC to PE conversion is used to convert the observed pulse heights in ADC counts into an estimated number of avalanches. Finally, a voltage scan is used to measure the break-down voltage of the MPPC and obtain the OV of the MPPC in any given run. This is needed as after-pulsing and cross-talk are related to the rate of saturation, and are themselves a function of voltage. This calibration process is very similar to the FGD calibration chain, except that the FGD event analysis typically does not integrate over a gating period, but rather treats distinct pulses separately.

3.1 The Mean Analysis Method

A complementary system to the Poisson analysis for measuring the amount of light being exposed to the MPPC is referred to as the “mean analysis”. The pulse height spectrum in Figure 3.1 is collected by histogramming all pulses which occurred during a particular gate period over many events. This spectrum can be used to calculate the average pulse height that was observed by fitting it to a sum of Gaussians, and integrating below the curve. This has the advantage that it is robust to noise. However, as the number of photons increases this spectrum blurs and this method fails.

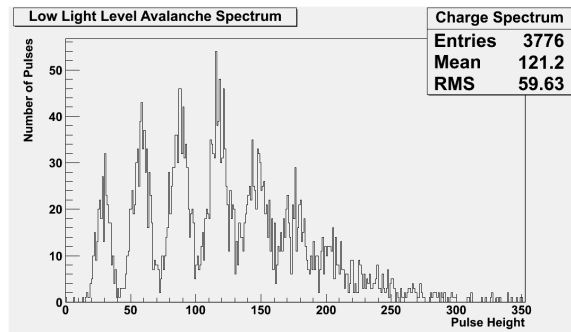


Figure 3.1: Plot of the pulse heights, measured in ADC counts, for a fixed gate over many events at low light intensity. This histogram shows the discrete avalanche structure present in the signal, which includes dark noise as a convolution. The fitted curve is a sum of Gaussians.

As the number of photons in a given laser illumination increases it is therefore necessary to analyze the mean of the charge histogram, rather than analyzing the distribution of the individual charges. Because a dark noise fire may occur simultaneously with the optically induced pulse (for instance, the laser in the MiniFGD data), one must subtract the expected

3.1. The Mean Analysis Method

dark noise signal. For example, if one observes a 3 PE pulse, it is impossible to tell what portion of that pulse height is dark noise and what portion is signal. One can only estimate an average contribution from the dark noise. We accomplish this subtraction by calculating the mean number of avalanches in dark noise sampled from a gate prior to the laser firing, and subtracting this contribution from the avalanches seen within the gate.

Because the gate surrounding the laser pulse must be large enough to include all laser pulses, it will also include some dark noise and after-pulses. To compensate for this effect, we sum the pulse heights seen in each waveform, and histogram this sum. The dark noise contribution can then be subtracted, and the error estimated as the error on the mean of this histogram. An example of such a histogram is shown in Figure 3.2.

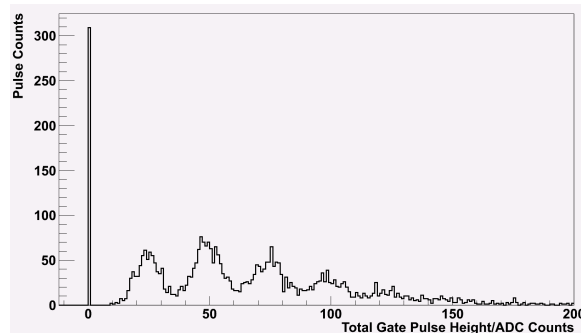


Figure 3.2: This histogram shows the sum of pulse heights in each event. It differs from the pulse height histogram seen in Figure 3.1 by the frequency of multi-pulse events. For small gates of the size we use, there is a typical dark noise contribution of 0.05 to 0.1 PE. This implies that between 5% and 10% of the time there is a dark noise pulse convoluted with any optical fires. Note that there is explicitly a set of events at zero in this histogram, whereas the pulse height histogram has no zero events.

As in the case of the Poisson analysis, the mean analysis can be cor-

3.1. *The Mean Analysis Method*

rected for pulse-finder efficiency. At the moment the pulse finder efficiency is characterized as between 96 and 99 percent by visually scanning for pulses and identifying those which are missed by the pulse-finder. We do not know how the efficiency varies with pulse height or the time since last pulse as these values cannot be estimated by manual comparison. As a result, the efficiency may in fact be substantially worse than currently measured. We therefore assume the efficiencies to be 1 during the analysis, with the understanding that this has introduced a systematic error. The measurement is performed on pulses which occur either in dark noise, or are clearly visible in the laser spectrum to a human operator. The measurements are therefore biased against measuring the efficiency of after-pulses, which we expect to make up a substantial part (Between 0 and 20% according to [25], or between about 4% and 25% according to [12]) of the true number of avalanches. An external simulation will be necessary to examine this effect.

Both the Poisson analysis and mean analysis compensate for dark noise. However, they measure slightly different things. The Poisson analysis measures the number of photoelectrons (NPe), the number of avalanches which were started directly by a prompt external photon, as opposed to after-pulsing or cross-talk. The mean analysis measures these but also includes avalanches caused by cross-talk and after-pulsing. This second quantity is referred to as the number of avalanches, or NAvA. The two methods use a very different mathematical basis, and can therefore be used to cross check one another. If they are functioning correctly, they should form a constant ratio with one another at low light level as both after-pulsing and cross-talk are independent of intensity at low light level. The plot in Figure 3.3 shows

3.2. *The High To Low Channel Conversion*

a comparison of these two methods, while Figure 3.4 shows the ratio of NPe to NAva. This shows the slight excess due to after-pulsing and cross-talk in the mean analysis. A scatter plot of the two quantities can be found in Figure 3.5, with residuals in Figure 3.6. The residuals indicate that the Poisson and mean analysis methods maintain a generally flat ratio at low light level. This is despite the fact that the power-meter measurement to NPe fits (shown in Figure 2.11) had a poor residual between 0 and 1 PE. As these two methods work in very different fashions, this suggests that the residuals in Figure 2.11 are not the result of a problem with the Poisson analysis. Future work will need to understand the source of this discrepancy. One possibility is that the attenuation calibration did not correctly remove a light background. This is unlikely, as the effect in Figure 2.11 is present even when the DA's own calibration is used. Another possibility is that the electronics or pulse-finder are biased in such a way as to introduce a non-linear response near 0 PE. This must be studied with simulation. A last possibility is that in the course of soldering the MPPCs to prepare them for direct exposure they were damaged. This will require a test performed with low temperature soldering in order to confirm the MPPCs response to heat treatment. The solution is as is described in Chapter 2: to fit above the area where this appears to be poorly behaved.

3.2 The High To Low Channel Conversion

The FEB has two channels for reading in each MPPC. Both channels use a 12 bit ADC, but one channel (the high attenuation channel) is attenuated

3.2. The High To Low Channel Conversion

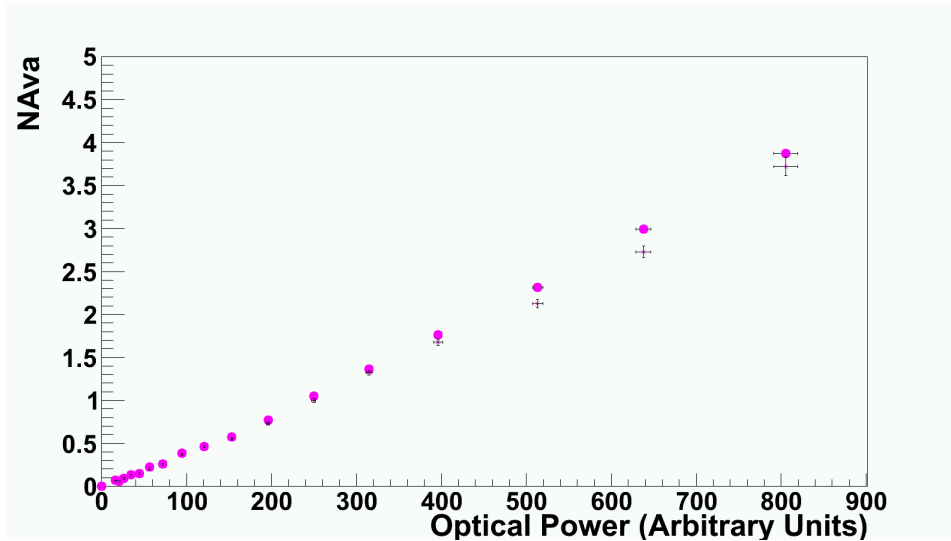


Figure 3.3: A plot demonstrating both the mean analysis and Poisson analysis on one graph. The circle points are the mean analysis, the X points are the Poisson analysis.

by a factor of about 8.5. The high attenuation channel will provide a larger dynamic range than the low attenuation channel, but a worse pulse height resolution. This factor is board dependent. Because high intensity pulses will saturate the low attenuation channel ADC, we must apply a calibration (the HiLo calibration) to convert the pulse height in the high attenuation channel to the equivalent low attenuation channel ADC counts. Figure 3.7 shows a waveform with a high intensity laser pulse saturating the low attenuation channel. It is necessary to perform this conversion well before reaching saturation, as it will distort the upper part of the charge histogram and bias the result, as shown in Figure 3.9. Figure 3.8 illustrates this conversion, which was done by applying laser light to MPPCs in the MiniFGD, and comparing the pulse height found in the high and low channels. The

3.2. The High To Low Channel Conversion

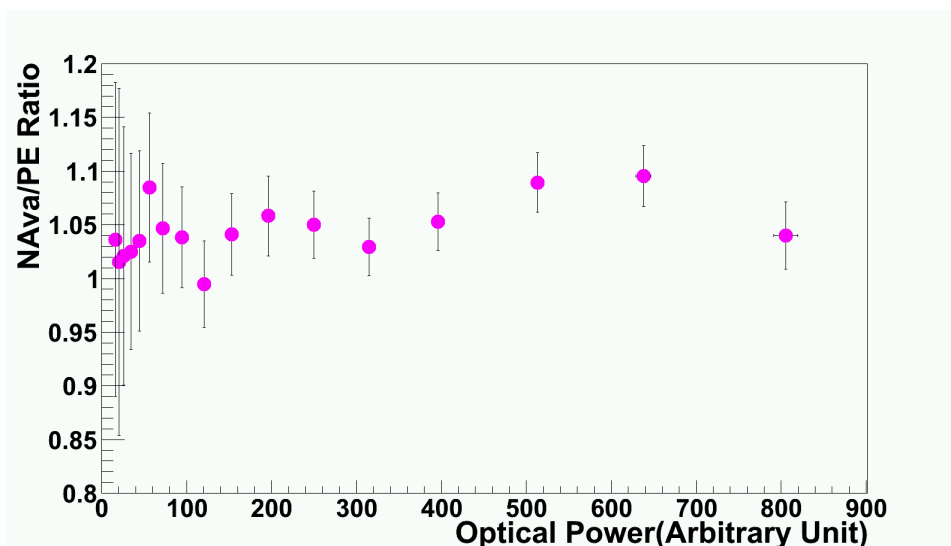


Figure 3.4: A plot demonstrating ratio of the mean analysis and Poisson analysis. The value above 1 indicates the excess to to after-pulsing and cross-talk.

pulse by pulse conversion was chosen for use in this analysis as it is the method used in the FGD calibration.

3.2. The High To Low Channel Conversion

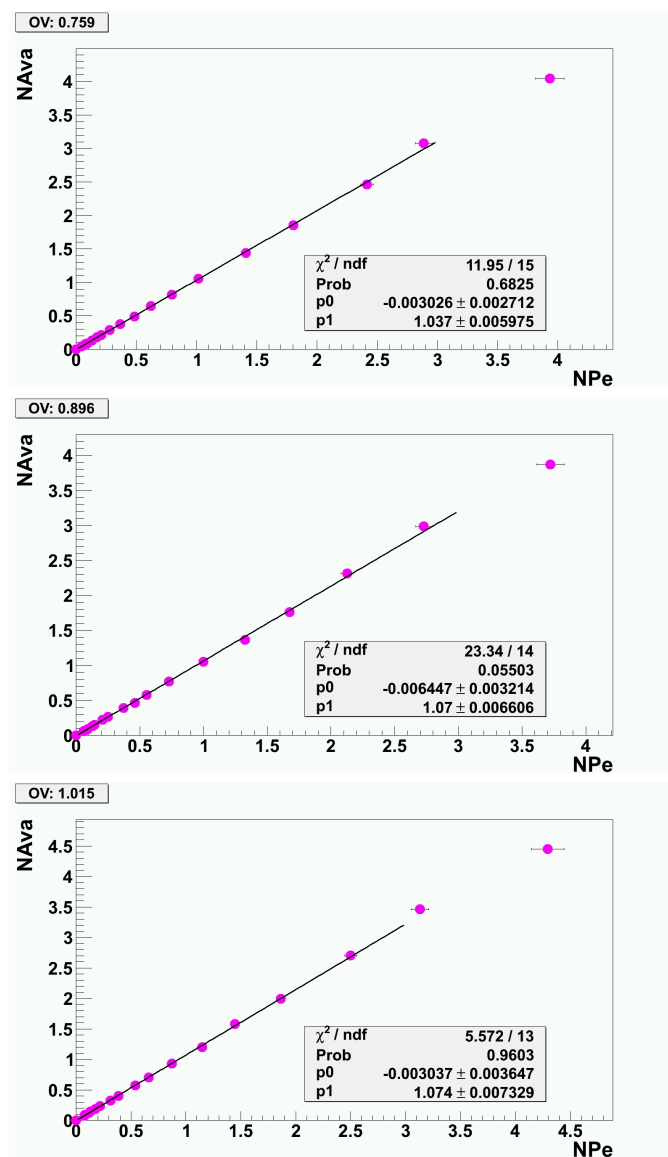


Figure 3.5: Direct comparison with fit of the mean to Poisson analysis. Fit range is 0 to 3 PE, as shown in the diagram.

3.2. The High To Low Channel Conversion

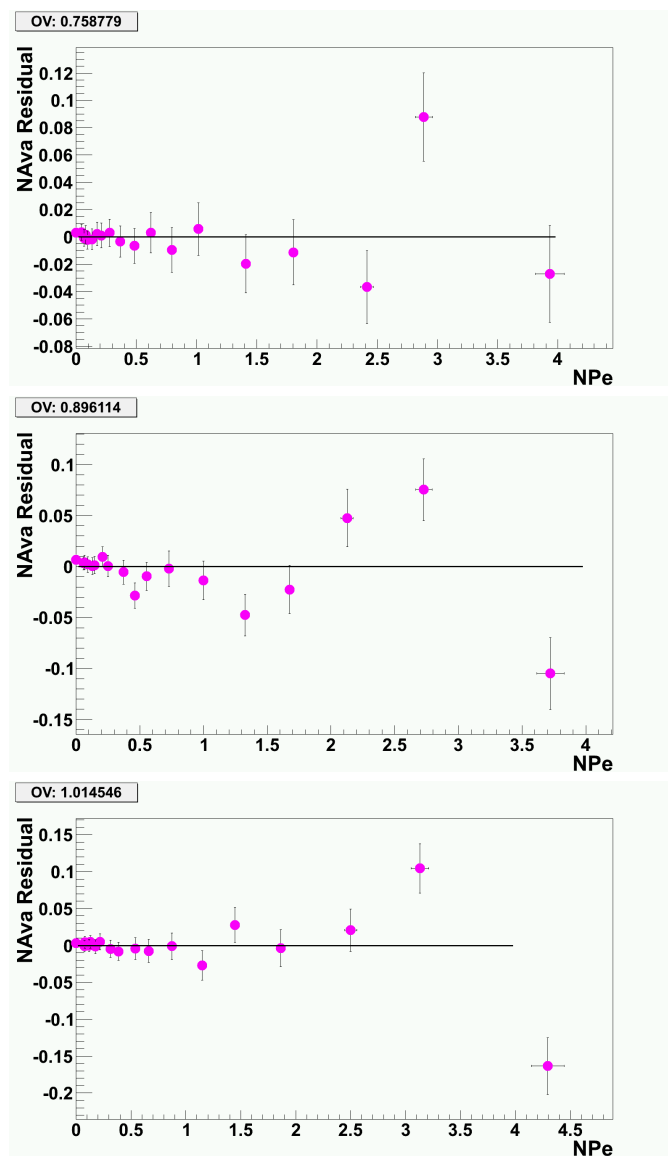


Figure 3.6: Residual of a fit of the mean to Poisson analysis scatter plot, demonstrating that the mean and Poisson analysis are in agreement, to within a multiple of the true slope due to after-pulsing and cross-talk.

3.2. The High To Low Channel Conversion

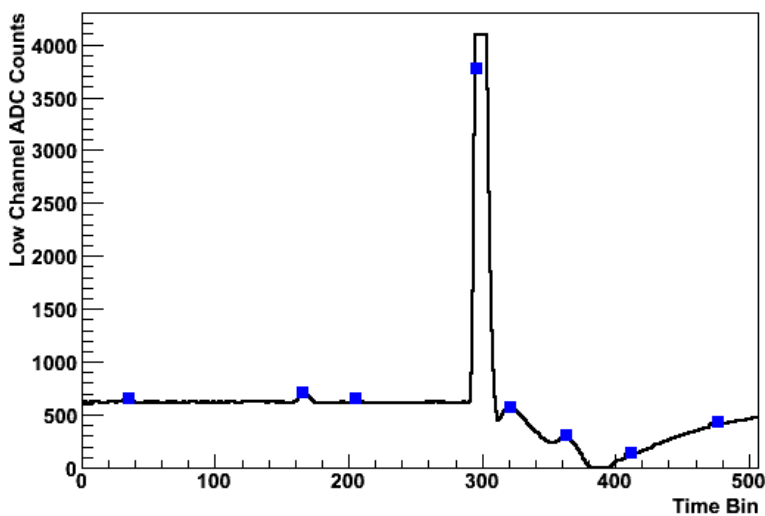


Figure 3.7: A waveform from a high intensity laser run, with the laser centered at time bin 300. Square dots indicate locations where the pulse-finder found a pulse. In particular, the pulse to the right of the laser is spurious and is produced by ringing in the recovery curve following the large saturating pulse.

3.2. The High To Low Channel Conversion

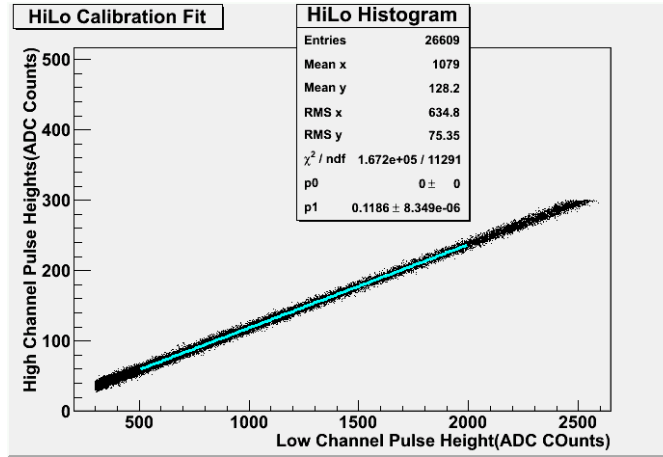


Figure 3.8: The high channel plotted against the low channel for one MPPC at one voltage, for all pulses. This plot is used to define the hi-lo channel calibration. The fit uses limited range to prevent noise and saturation from biasing the result. The histogram has cuts to remove pulses with values greater than 300 in the high channel, or less than 300 in the low channel. The fit itself is performed on the range 500 to 2000 on the low channel.

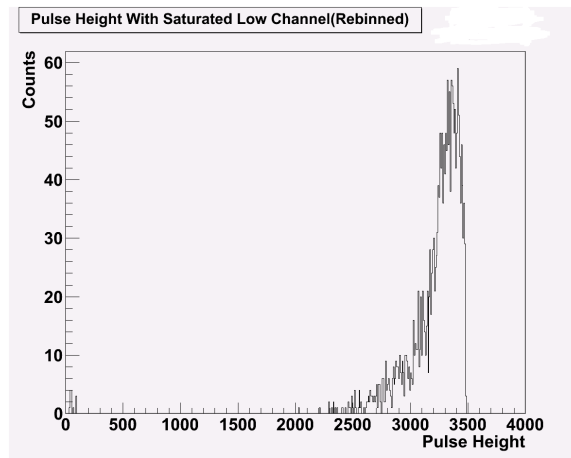


Figure 3.9: This is a pulse height histogram showing the low attenuation channel saturation. This effect necessitates using the high channel substantially before the mean expected pulse height approaches the limit.

3.3. Gate Timing Selection

Although the same components are in principle used on each voltage divider, part to part differences may result in some variation in value of the HiLo conversion. The conversion factor is shown for a selection of MPPCs and voltages in the Figure 3.10.

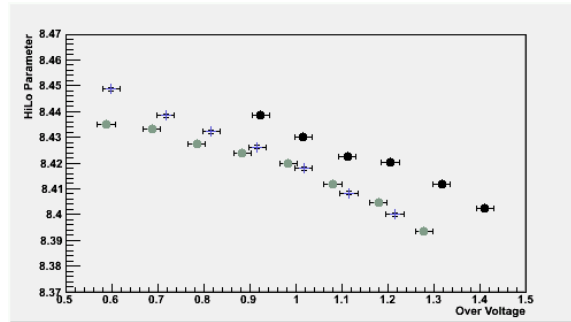


Figure 3.10: This plot shows the high low conversion factor against voltage. Different colors represent different MPPCs, whereas different symbols represent different fibers. Solid circles represent bare MPPC measurements.

The distribution in Figure 3.10 varies by about 1% over the range used. This effect is not understood, however it is suspected that a frequency dependence in the attenuation circuitry may be responsible. This is corrected for in the analysis presented in this work but is such a small effect that it is probably not necessary to correct for this in the FGD.

3.3 Gate Timing Selection

For the purposes of gate selection it is desirable to include all optical pulses in an event but to exclude as much noise as possible. The position of the laser gate on the waveform is determined by finding by eye the bounds on the laser timing distribution. This can be seen in Figure 3.11 and Figure 3.12.

3.3. Gate Timing Selection

The gate edges were chosen to go from time bin 293 to 302 inclusively. Figure 3.12 demonstrates that this gate should collect the vast majority of optical pulses. If the later gate bound is too early, the after-pulsing component will be underestimated. If the gate bound is too late we will over subtract the dark noise correction due to the pulse finder and electronics being unable to detect pulses after a primary pulse. An excess of artificial events can be seen in Figure 3.11 after the laser pulse. These are known to be artificial as they occur in every high intensity event, and do not show a typical pulse shape.

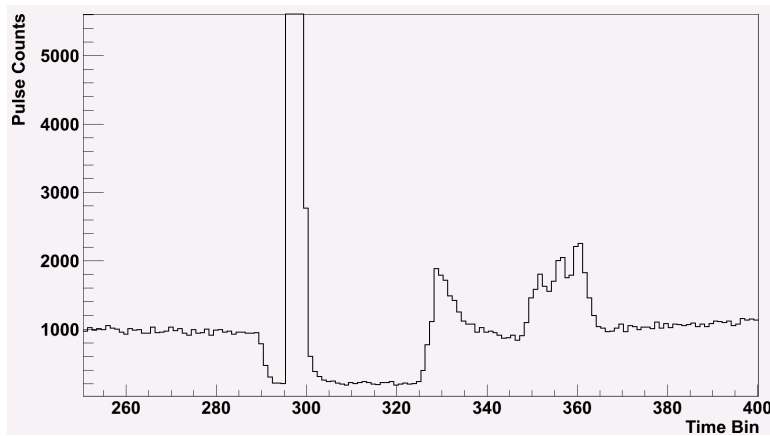


Figure 3.11: This figure illustrates the time distribution of the pulse in the waveform, zoomed broadly around the laser at 300 time bins. This histogram includes all pulses for an entire intensity scan. Two dead zones (caused by large laser pulses tending to “absorb” smaller ones) can be seen on the sides of the laser gate and to beyond them it’s one can see the dark noise forming a solid background above 380 and below 280 time bins. Additionally, false pulses are found in the region just right of the dead zone between 330 and 375 time bins.

3.4. Pulse Height to Photoelectron Conversion

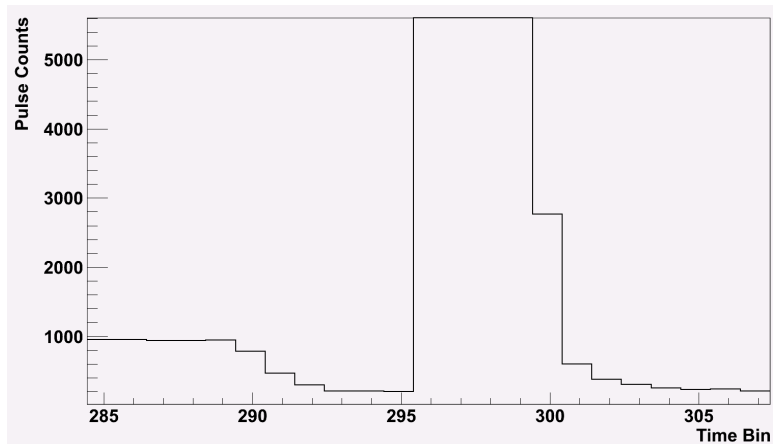


Figure 3.12: This time histogram of an entire intensity scan is zoomed in on the region around the laser pulse. There is a long tail after the laser pulse that may be due to late de-excitations from the WLS fiber. We could increase the size of the gate to capture these, but this would increase the noise rate and increase the issue of pulse-finder efficiency after large pulses.

3.4 Pulse Height to Photoelectron Conversion

The mean analysis takes as its input a histogram of total pulse heights from the laser gate and outputs an estimate of the average number of avalanches that occurred in the gate. The conversion is done by dividing the average total pulse height seen in an event by the pulse height seen with one avalanche dark noise pulses. The one avalanche pulse height (often referred to as the one PE pulse height, because the two are equivalent unless there is a long after-pulsing pulse) is measured for each intensity setting. This in practice means that gain variations slower than the one minute run length will be removed by this conversion.

In order to measure the the one PE pulse height we employ the gate scheme described for the Poisson analysis: we analyze the behavior of the one photo-electron peak as observed prior to the laser in the waveform. For this calibration our gate is the entire space prior to the laser gate on the waveform. To avoid pulse-finder effects we do not use the 20 time bins at the beginning of the waveform or the 20 just prior to the laser pulse. It is also necessary to place a veto on pulses where another pulse has occurred within 30 time bins, as the recovery will bias the pulse height downward. This effect can be as large as a few percent.

Figure 3.13 shows a histogram of all pulse heights which occurred within the gate with an example fit of the 1-photo-electron peak. The 2-PE peak is visible on its right hand shoulder. A conversion between low-channel pulse height in ADC counts and the number of avalanches is now accomplished by assuming a constant conversion factor of the one photo-electron pulse

3.4. Pulse Height to Photoelectron Conversion

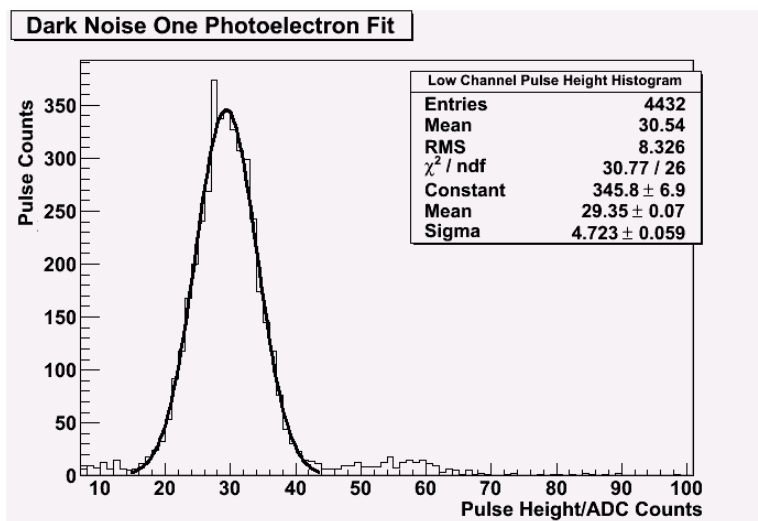


Figure 3.13: This histogram show the distribution of dark noise pulse heights, and a Gaussian fit to the largest one used to calibrate the value of one avalanche for this run.

height. This assumes that the pulse height of a pulse with 20 avalanches has 20 times the pulse height of a one avalanche pulse.

Although it is unnecessary to correct for temperature due to the short time scale of this measurement, it is worth noting that had we not measured this factor on every run it would have been necessary to correct for temperature. Figures 3.14 illustrates the relationship between temperature and 1PE pulse height. The expected relationship is that for each degree increased, the MPPC break-down voltage will increase by 56 mV, and thus the pulse height will decrease.

The one PE pulse height conversion is performed once for every run. When data from all runs is looked at collectively there can 2500 or more points in a single fit. At higher voltage, the dark noise charge histogram

3.4. Pulse Height to Photoelectron Conversion

becomes noisier because of electrical noise. This causes the rates of failed one PE Pulse height fits to increase. It is therefore important to fail rarely, and in the event of a failure to veto the point. Reliable fits are accomplished by forcing the Gaussian fit to have a mean close to the maximum bin of the charge histogram and by fitting only near the maximum bin. Points where the error on the Gaussian mean parameter is greater than 10% or larger than 0.5 bins are rejected. We also require that the χ^2 value to be less than 10^6 and that the maximum bin be within 3 bins of the Gaussian mean. The χ^2 requirement is intended to remove any fit which gets stuck with very large parameter values. The final fit and veto results (removed with rules just mentioned) are shown in Figure 3.15. This plot shows the one photoelectron pulse height as determined by this calibration for an entire set of intensity and voltage scans. Each voltage results in a roughly constant one PE pulse height on the graph, with intensity being decreased from largest to smallest as we increase the run number.

At the beginning of each run in Figure 3.15, a downward tail is visible in the runs where the DA is at the lowest attenuation setting and hence at the highest intensity. This effect is not fully understood, but is believed to be caused by the partial depletion of a charging capacitor in the channel splitting circuitry around the MPPC. Under this hypothesis, the effective voltage would drop somewhat for the highest few points in each run. As the shift is smaller than the separation between voltage sets, this will not have a substantial effect on the analysis. This is further mitigated by the fact that those runs which are worst in this sense will also likely to have had pulses which saturated the high channel ASIC, and will have been removed

already.

3.5 Determining the Over-Voltage of an MPPC

The OV is an important variable in determining the behavior of MPPCs. To first order, almost any effect can be described purely as a function of OV. This is particularly important as the MPPC is extremely sensitive to temperature - but a shift in temperature results in a shift in OV which simultaneously explains most of the change due to temperature.

Before performing intensity scans (Normally done at between 5 and 9 OV values), a voltage scan is taken between 67 and 71V. This allows us to determine the OV (the voltage level above the breakdown voltage) for any given run. Figure 3.16 shows the linear relationship between voltage and one photo-electron pulse height with the results of a voltage scan. At the break-down voltage, the gain of the MPPC drops by many orders of magnitude, and grows linearly above this point. Measurements in the FGD have indicated that a quadratic relationship may more accurately describe these curves, however such curves fail more often during fitting and provide nearly identical results when successful. Voltage scans are important because we expect after-pulsing and cross-talk to be functions of OV. This will cause the saturation behavior to also be a function of OV, and so the calibration must take this into account.

3.5. Determining the Over-Voltage of an MPPC

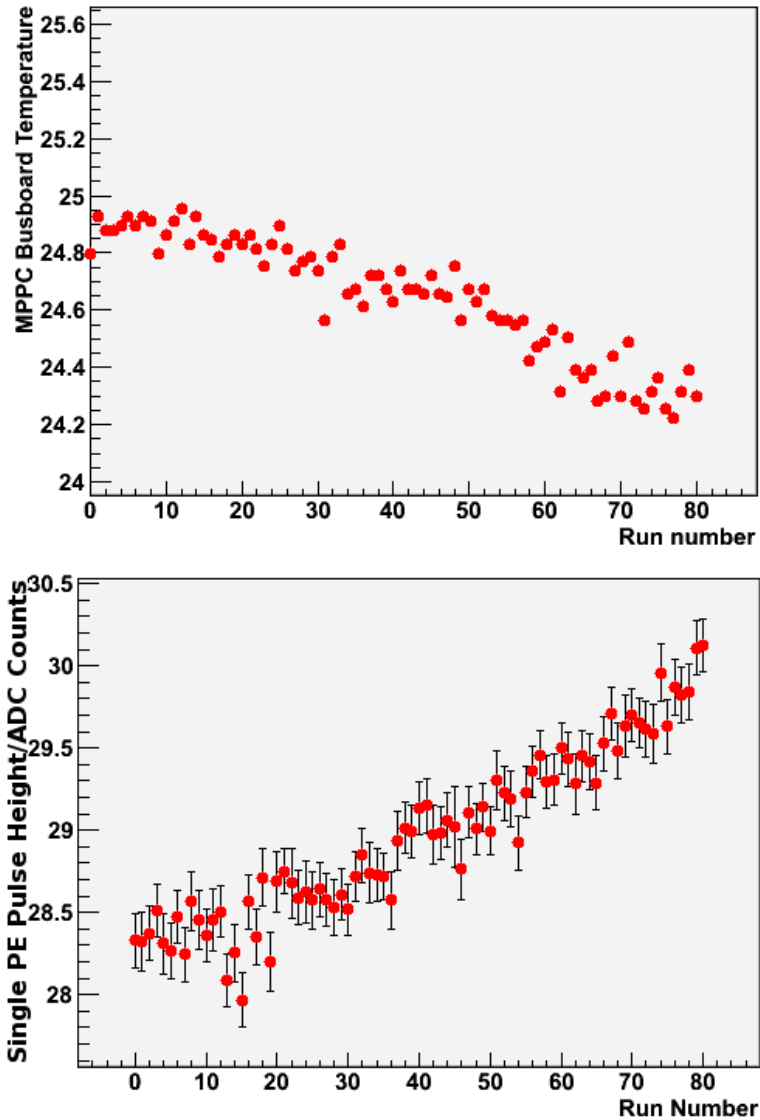


Figure 3.14: The top figure illustrates the temperature reading from a sensor on the bus-board used during a single intensity scan. The x-axis indicates which run in the series was used. The bottom figure illustrates the one-PE pulse height measured for each of these runs, and shows the temperature dependence qualitatively matching the expected behavior - increasing as temperature decreases. The size of the temperature change during this intensity is unusually large due to the length of time this scan took. A typical intensity scan has a scan length about 1/4 the time this one used.⁷⁴

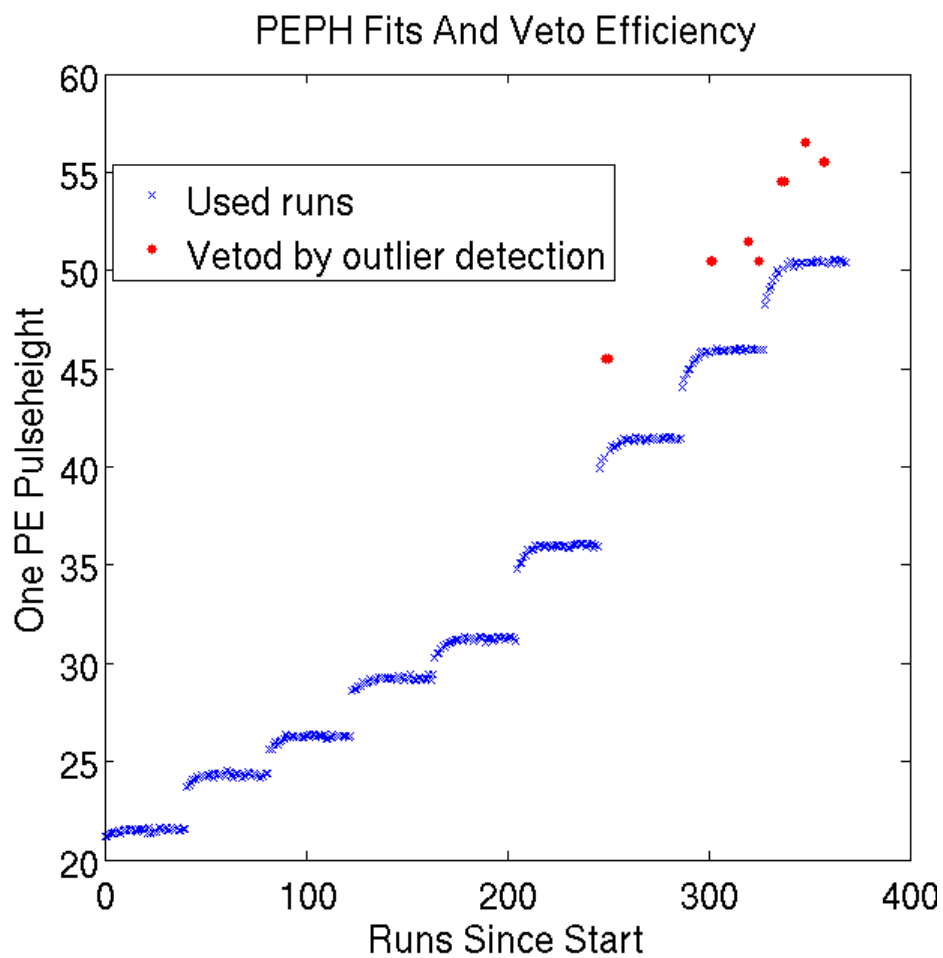


Figure 3.15: This figure illustrates the one-PE pulse height measured for each of these runs, and shows (in red circles) the failed fits. Failed fits were all selected for removal by the vetos described in the text.

3.5. Determining the Over-Voltage of an MPPC

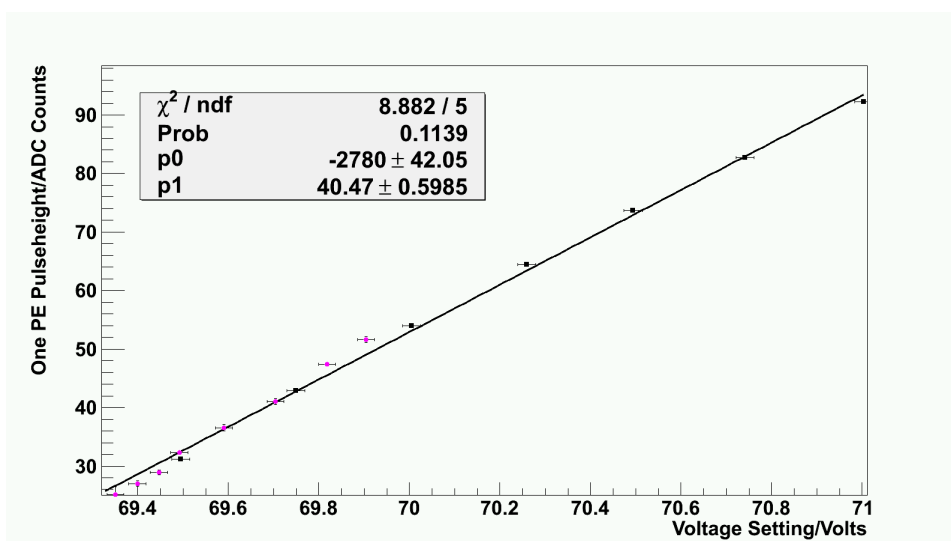


Figure 3.16: This plot shows the relationship between one-photoelectron pulse height and voltage for one MPPC. Runs marked with a circle were taken during the run itself, whereas points marked with a square were taken during a dedicated voltage scan before the run.

Chapter 4

The MiniFGD Saturation Analysis

The focus of this work is to produce a saturation calibration of the MPPC within the context of the T2K FGD detectors. In the previous chapters we have shown calibrations for measuring output from the MPPCs in terms of the number of avalanches, a calibration of the optical light scale that is linear with the true light levels and extracted the over voltage in any given run based on voltage scans. These three methods, taken together, allow us to measure what effect the saturation of the MPPC has on the device at high light intensity. This chapter will introduce a functional form for this correction, and explore the consequences of different methods of fitting this function to the saturation curves.

4.1 Saturation Parametrization

A common parametrization in use by groups studying MPPCs and other avalanche photo diodes can be derived under a few assumptions. If the probability of any given pixel firing when exposed to a single photon is:

4.1. Saturation Parametrization

$$P = \frac{\text{PDE}}{N_{pix}} \quad (4.1)$$

then the expected drop in the number of unfired pixels (“Pix below”) for a small change light exposure, δx , is:

$$\langle \delta \text{Pix} \rangle = -\delta x \frac{\text{PDE}}{N_{pix}} \text{Pix} \quad (4.2)$$

Because the MPPC is a probabilistic device, the exact response to a given number of photons cannot be exactly predicted. We therefore approximate the drop in available pixels as the expected drop, with the knowledge that there is some deviation in this response:

$$\frac{d\text{Pix}}{dx} \approx -\text{Pix} \frac{\text{PDE}}{N_{pix}} \quad (4.3)$$

$$\text{Pix}(x) = N_{pix} e^{-x \frac{\text{PDE}}{N_{pix}}} \quad (4.4)$$

We can subtract the number of pixels unfired ($\text{Pix}(x)$) from the total to arrive at a formula for total fired pixels:

$$N_{output} = N_{eff} \cdot (1 - e^{-x \times \text{PDE} / N_{pix}}) \quad (4.5)$$

4.1. Saturation Parametrization

where:

- N_{eff} = The effective number of pixels in the device. The term “effective” is used because the number of pixels produced by this fit will be close to the number of pixels illuminated, rather than the number on the MPPC.
- PDE = The particle detection efficiency as defined for the entire device
- x = Applied number of photons
- N_{output} = The observed number of avalanches

This formula has the advantage of being well based in theory, is used both within the FGD as well as by other detector groups within T2K employing the MPPC, and by other groups studying MPPC performance[22].

This parametrization suffers from a number of deficiencies. First, it assumes that all photons strike the MPPC simultaneously. Because the MPPC has a pixel re-fire (pixel recovery timescale) rate of a few nanoseconds, the number of pixels fired can exceed the number of pixels in the MPPC for longer optical pulses. Optical pulses in the FGD can have a timing distribution longer than 7 ns (the WLS fiber de-excitation time constant) due to optical effects in the scintillator bar and WLS fiber. By contrast the laser study done in the MiniFGD uses substantially shorter pulses (about 85ps, although changing the power setting is known to affect this slightly). Further, this parametrization ignores the possibility of cross-talk between the pixels or of light non-uniformity. In particular, both the laser and WLS fiber are known to have a light profile with higher intensity near the center,

4.1. Saturation Parametrization

and low intensity on the edge. The pixels with high illumination will tend to fire earlier than the ones with low illumination. Pixels with very little illumination may effectively never fire.

In the studies performed by the FGD group, we have chosen to work in a unit defined by the amount of power incident on the MPPC necessary to observe one photoelectron on average. The process of deriving these units creates a ratio of NAva to NPe of greater than 1 as the parametrization asymptotically approaches no applied light. This excess is the result of cross-talk and after-pulsing. That is, we expect that without after-pulsing and cross-talk:

$$\frac{dL}{dx} = \text{PDE} * e^{-x * \text{PDE} / N_{pix}} \quad (4.6)$$

$$\lim_{x \rightarrow 0} \frac{dL}{dx} = \text{PDE} = 1 \quad (4.7)$$

However, as this parametrization is not an exact match for the physics of the MPPC, the constraint of PDE=1 may be violated while fitting in order to better match the full shape of the curve. As our linear light scale is based on the number of photo-electrons rather than the number of avalanches this is expected. One would expect that the asymptotic slope is unity plus the cross-talk probability, and some fraction of the after-pulsing probability. This may not be the case over the entire optical range as the probability of after-pulsing and cross-talk will decline when there are fewer additional pixels available to fire. Hence there is a non-linear distortion of the fitting curve which will be reflected in the best-fit parameters.

The number of effective pixels, N_{eff} , is not necessarily the 667 pixels in MPPC. This is the expected number in the case of uniform light illumi-

4.1. Saturation Parametrization

nation. However as mentioned above, the light application is not uniform but rather approximately Gaussian[10]. Further, the number of pixels hit by the light from a track in a single channel may have an upper limit due to shadowing effects of WLS fiber on the surface of the MPPC (where some pixels are exposed to little or no light from the fiber). This results in an effective N_{eff} lower than the value for the bare MPPC exposure. Due to the effects of charge transfer between pixels, the number of exposed pixels cannot be considered an upper bound on the N_{eff} parameter but it may be lower in practice due to the light illumination effects mentioned above. This reduction depends on the the MPPC to WLS fiber coupling. We do not presently know how much variation in coupling efficiency there is. Both the N_{eff} and PDE parameters above are needed in order to encompass the variety of data present.

The saturation effects on the MPPC are not small. The 2nd order deviation from linearity expected is:

$$\begin{aligned} \delta N_{output} &= \text{PDE} * x - N_{pix} * (1 - e^{-x * \text{PDE} / N_{pix}}) \\ &= \text{PDE} * x - N_{pix} + N_{pix} \left[1 - \frac{x * \text{PDE}}{N_{pix}} + 0.5 * x^2 \frac{\text{PDE}^2}{N_{pix}^2} + O(x^3) \right] \end{aligned}$$

Note in the above expansion that in the limit of no light exposure we produce linear behaviour. Under the assumption PDE is = 1, we have:

$$= x^2 \frac{\text{PDE}^2}{N_{pix}^2} = \frac{x^2}{667 * 2}$$

4.1. Saturation Parametrization

$$\frac{\Delta L}{N_{output}} = \frac{x}{667 * 2}$$

This implies that a 1% deviation from linearity is expected around 14 PE, and a 10% deviation at 140 PE, with upper order terms each a factor of 667 smaller.

In order to explore this measurement under controlled conditions, we have used the MiniFGD to expose single MPPCs to a known light exposure. Figure 4.1 below shows a typical saturation curve using a curve with parameters $N_{eff}=667$ and $PDE=1$. The curve is clearly a poor fit. The dominant difference is due to the use of a PDE of 1 in the curves. Attempts at fitting this function are shown in the following sections.

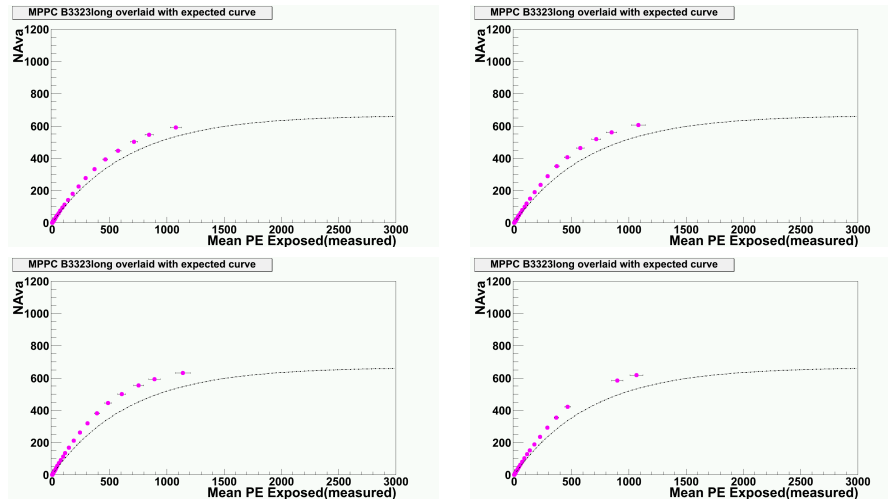


Figure 4.1: The naively expected saturation curve for a bare MPPC would use 667 pixels, and have an intercept slope of 1. These four plots are taken with one MPPC at four different voltages, with the default saturation curve super-imposed. The plot the output of the MPPC in NAVA to the input extrapolated using the power-meter measurements. This graph clearly shows that after-pulsing and cross-talk significantly contribute to this process.

4.2 Saturation Fit Parameters on Bare MPPCs

The plots in Figure 4.1 show that the expected values are not a good description of the data. In particular, we expect that there is 0-20% after-pulsing and cross-talk[25], and that this should be voltage dependent. Figure 4.2 shows bare data fitted with N_{eff} and PDE floating, while Figure 4.3 shows the residuals to the fit and Figure 4.4 shows the relative residuals (Noting we have deliberately cut off data on the low end of the relative residual). The fits were performed on a range of 0 to 1000 PE. This will produce different results when compared to other detectors in ND280 because they use a different electronics system (known as TRIP-T) and saturate their ADC at a lower light level (about 400 PE), and will therefore sample a smaller range of the behavior for their fits. If this function modelled the data perfectly this would not matter. Because higher light levels match this function more poorly than lower light levels, we will reach systematically different results by sampling on different ranges.

The residuals here are defined as the fit function minus the data point, and in the relative residual they are normalized by the function. This demonstrates that the relative residual in the fits is small above 100 PE. Poor low level performance cannot be explained by an incorrect fit in the linear optical scale, as the PDE parameter is able to scale to correct such a deficiency. The residuals in the fits to the bare MPPC are typically less than 10%, and above 70 PE do substantially better.

The distribution of fit parameters for the MPPC with serial number B3323 can be seen as a function of OV can be seen in Figure 4.5, while

4.2. Saturation Fit Parameters on Bare MPPCs

the distribution over all bare MPPCs can be seen in Figure 4.6. Examining Figure 4.6, between 0.6 and 0.9 V OV (the range we are interested in) the average N_{eff} value is 861.9 ± 11.2 and the PDE parameter is 1.099 ± 0.003 .

Precise parameter values describing the saturation of the bare MPPCs are not necessary for this work, as the FGD uses only fiber data. All data points are placed together in Figure 4.7, with the above fit parameters. The fits appear to be generally of good quality, judging from the χ^2 values seen in Figure 4.8. The χ^2 values seem too low given the residuals present in the function, which suggests we are over-estimating our errors on the points. Figure 4.9 shows pull graphs for this data, which would be expected to be centered on zero for accurate χ^2 values of the size we are seeing. These graphs support the interpretation that we are over-estimating the error on our data points.

4.2. Saturation Fit Parameters on Bare MPPCs

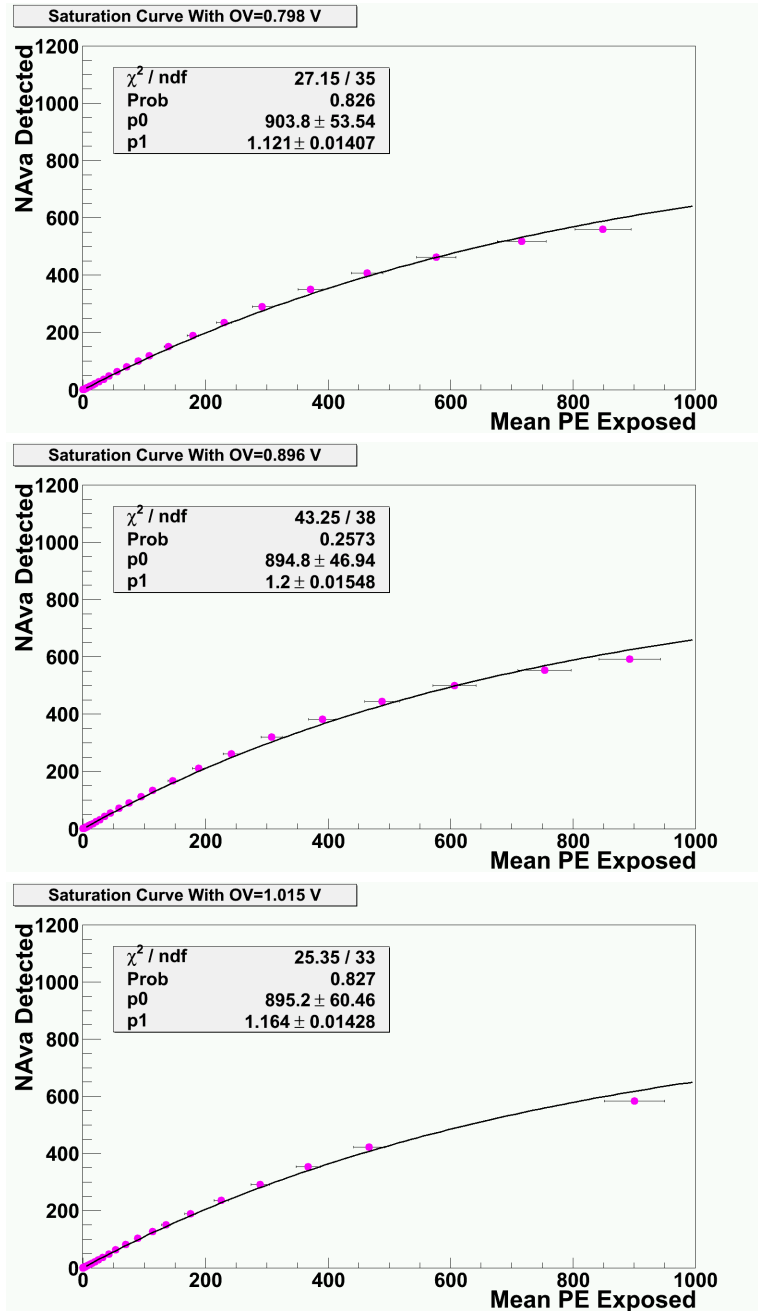


Figure 4.2: Plot shows the best fits of the bare data to the two parameter saturation function. p0 is the N_{eff} parameter, and p1 is the PDE parameter used in the above saturation formula.

4.2. Saturation Fit Parameters on Bare MPPCs

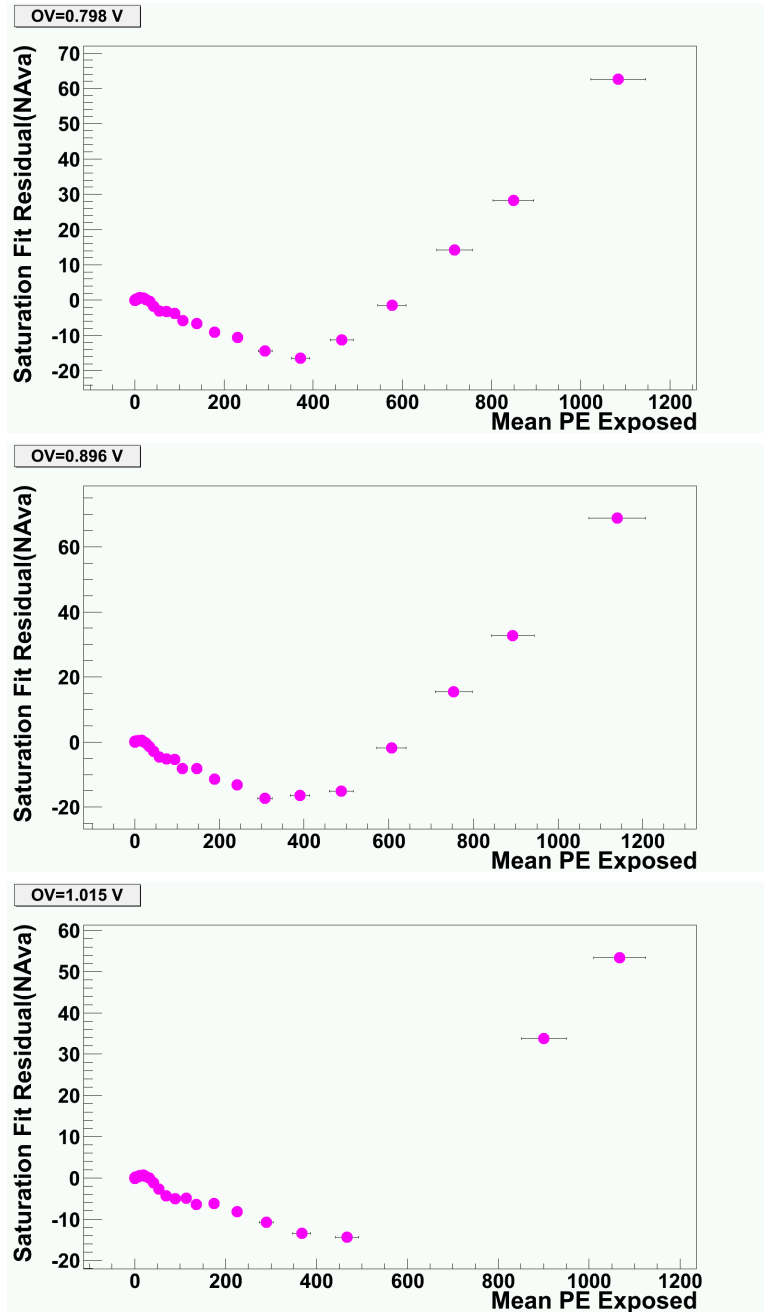


Figure 4.3: Plot shows the residuals of the bare data to the two parameter saturation function.

4.2. Saturation Fit Parameters on Bare MPPCs

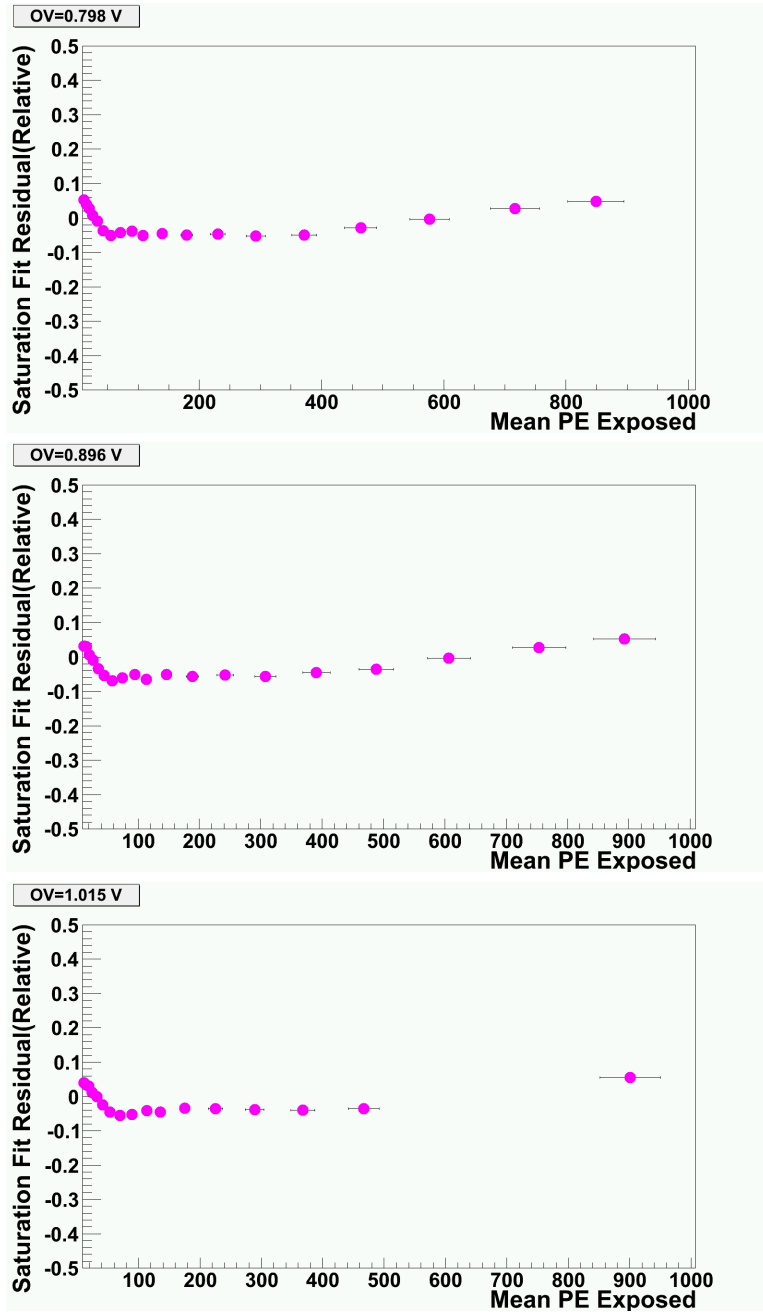


Figure 4.4: Plot shows the relative residuals of the bare data to the two parameter saturation function. Note that we have excluded the bottom end of the range to allow for meaningful judgments on the high end.

4.2. Saturation Fit Parameters on Bare MPPCs

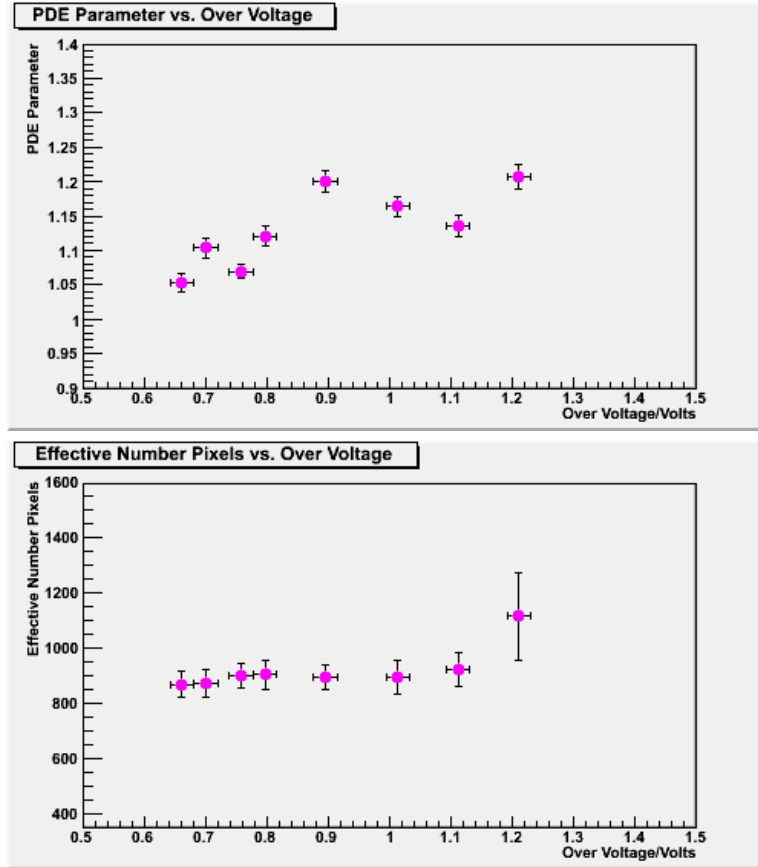


Figure 4.5: The top plot is the PDE parameter for one MPPC as a function of voltage, whereas the bottom plot show the N_{eff} , the effective pixel count as a function of voltage.

4.2. Saturation Fit Parameters on Bare MPPCs

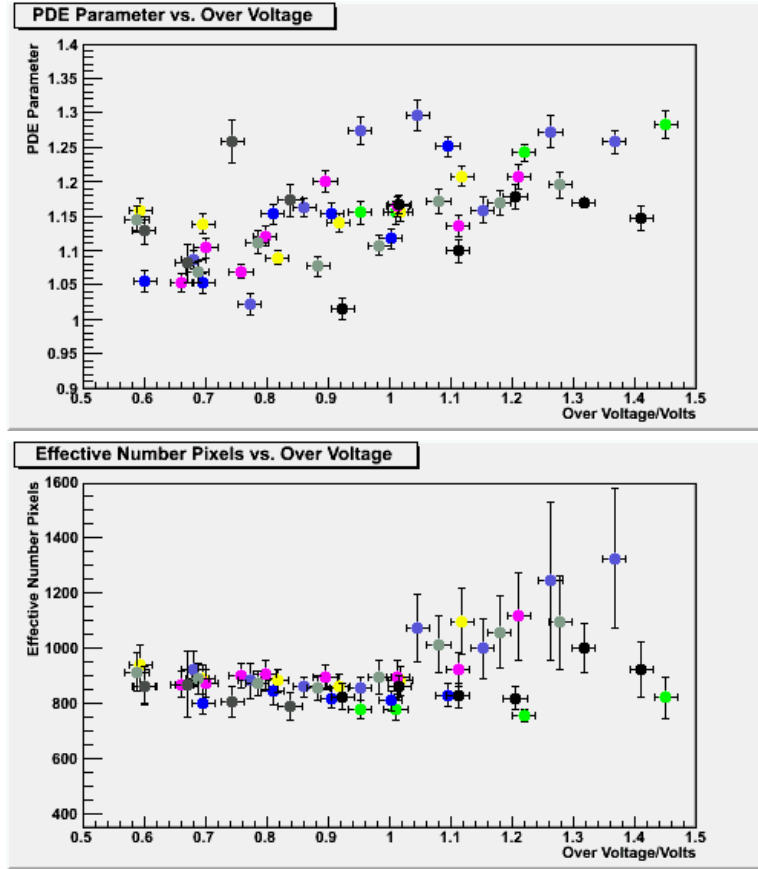


Figure 4.6: The top plot is the PDE parameter for all bare MPPCs as a function of voltage, whereas the bottom plot show the N_{eff} , the effective pixel count as a function of voltage. Each color is a separate MPPC

4.2. Saturation Fit Parameters on Bare MPPCs

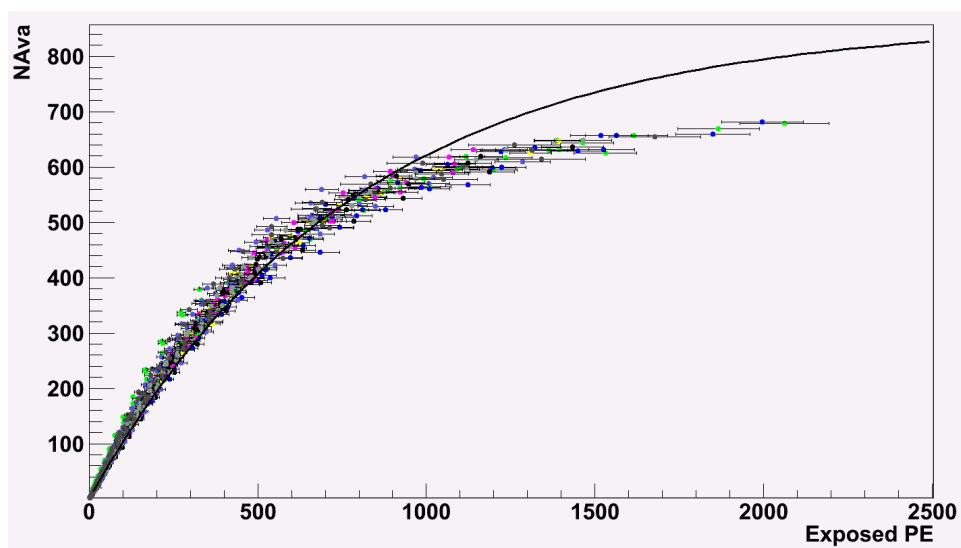


Figure 4.7: This figure shows all bare MPPC data, from all voltages. The displayed curve is a rough value consistent with the fits, with $N_{eff}=862$ and $PDE=1.10$.

4.2. Saturation Fit Parameters on Bare MPPCs

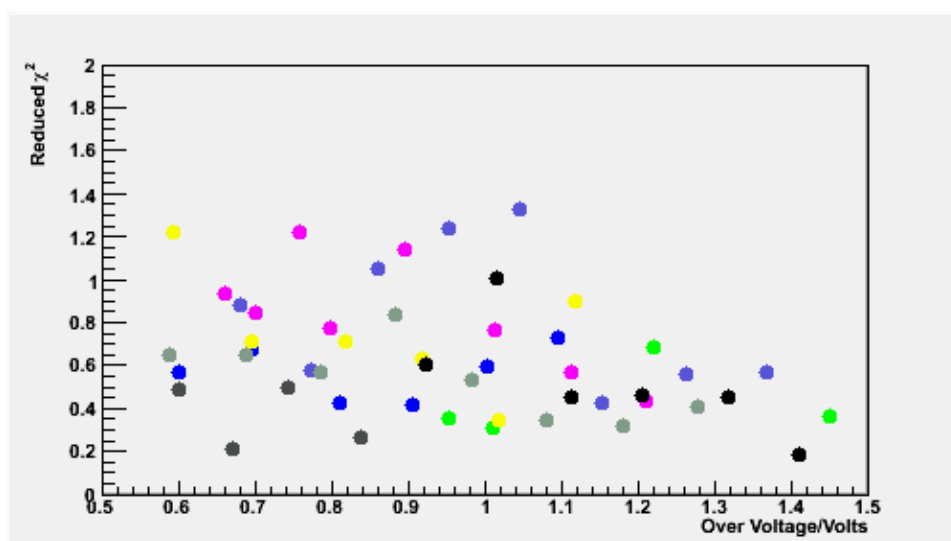


Figure 4.8: This figure shows the reduced χ^2 for bare MPPCs fit with the standard expression using two parameters. Each color represents a different MPPC. These values suggest that we are over-estimating our errors on the data points, as the structure in the residual does not support the idea that our fits are as strong as these χ^2 values indicate.

4.2. Saturation Fit Parameters on Bare MPPCs

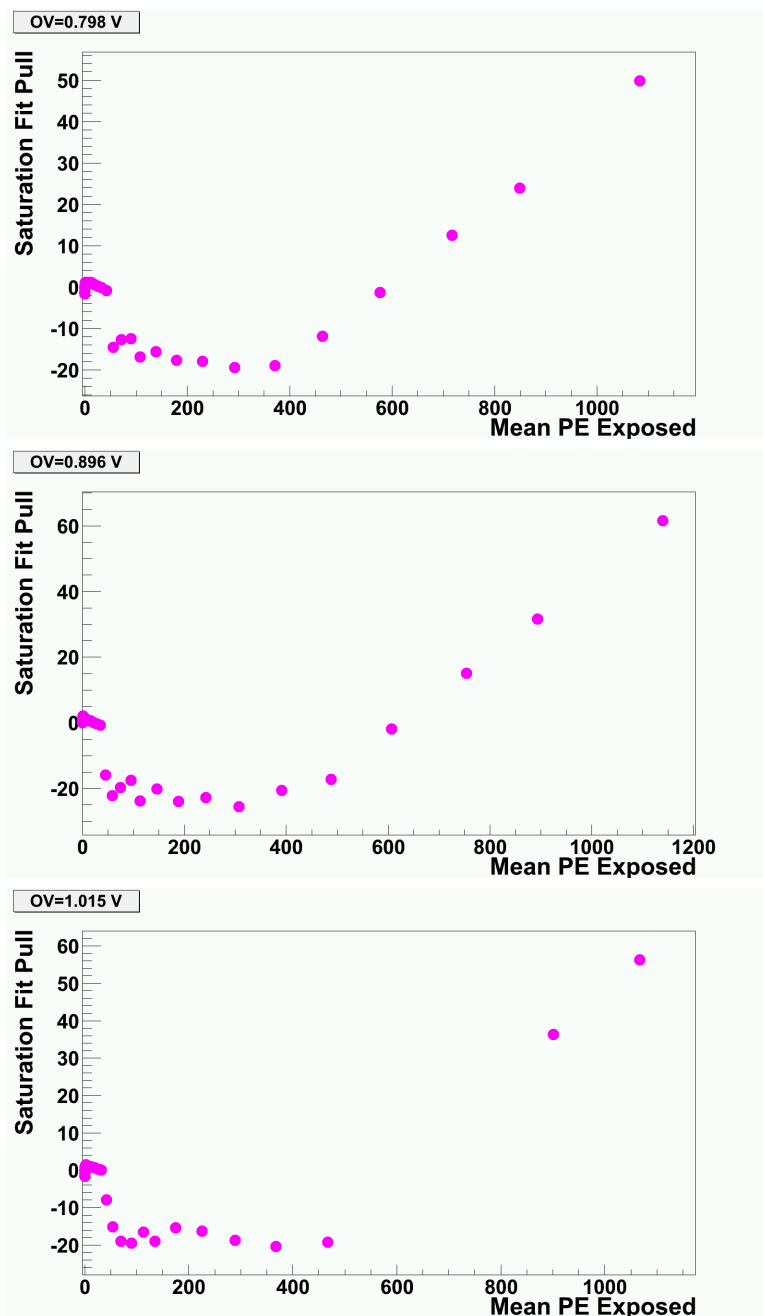


Figure 4.9: The pull graphs for the bare data fits in Figure 4.2.

4.3 Fiber Saturation Studies

The purpose of these studies is to measure the saturation effects in the MPPCs used in the FGD. With that in mind, we not only measured the saturation of the MPPCs alone, but also in combination with WLS fibers. The optical properties of the WLS fiber become somewhat important at this point. In particular, it is fortuitous that a laser was available with a wavelength of 405 nm, close to the WLS fiber peak of 430 nm. An additional question regarding the optical properties of the WLS fibers is whether the distribution of light exiting them is a function of distance from emission. In order to test this, several fibers were excited at both 57 mm and 258 mm from the edge of the scintillator bar being used to hold the WLS fiber in position. The results in Figure 4.10 indicate that on the available resolution in our experiment no difference is visible. This test should not be seen as showing that there is not a relationship between position of excitation and saturation in the FGD, as the FGD fibers are about 2 meters long. This test only shows that on the length of the MiniFGD there is visible no dependence.

We proceed with the analysis of the fiber data in a similar fashion to the bare MPPC saturation measurement. In Figures 4.11, 4.12, and 4.13, we display the two parameter fits, residuals, and relative residuals to a series of 4 voltages, each performed on MPPC B4371 for one fiber. In the fitted range the plots are generally well behaved, showing small relative residuals above 50 exposed PE and below 1000 exposed PE.

Unlike the case with the bare MPPCs, we see in Figure 4.12 that the residual actually becomes extremely large - a residual of hundreds of avalanches

4.3. Fiber Saturation Studies

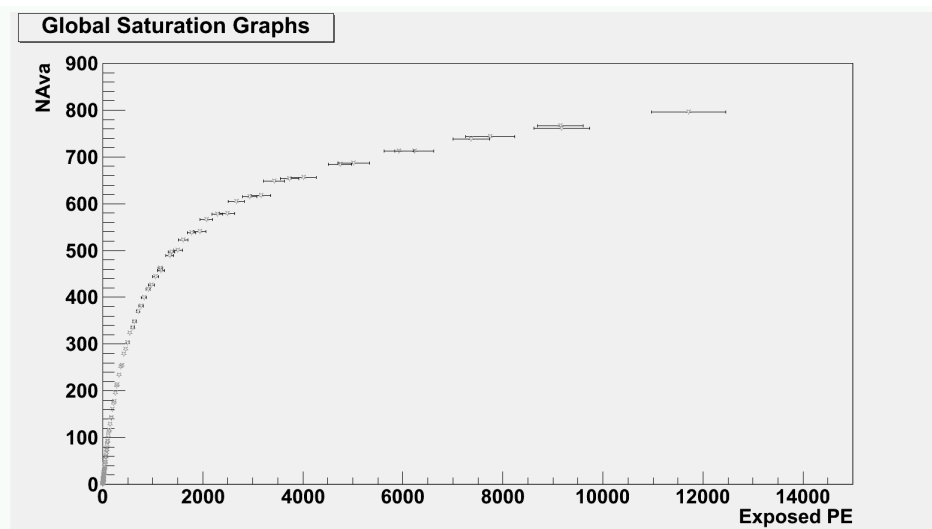


Figure 4.10: This figure shows data taken 57 and 258 mm away from the edge of the scintillator with the same MPPC and fiber. In particular, points in gray were taken at 258 mm, and points in blue from 57 mm. The data is from the range 0.6 to 0.9 V OV, and the distributions appear to overlap to the precision the experiment allows.

at maximum. However, examining the ranges on the residual plots will show that large residuals only become present at values far outside the fit range used (0 to 1000 PE). Figure 4.17 demonstrates that the behavior of the MPPC-fiber complex is not describable by the parameters chosen at high light illumination, however as mentioned earlier light pulses of this magnitude will occur rarely in the FGD. Further, the gradual rise in NAVA output seen in this data at high light level cannot be described well with this function with any parameters. Because the optical efficiencies of the coupling to the bare MPPCs are different than the coupling during fiber measurements, the laser power was set to different powers on the two run types, although

4.3. Fiber Saturation Studies

the setting was consistent on most of the runs within each group. This is likely responsible for the rather large difference in ranges of light illumination between the two data sets: whereas the bare data runs between perhaps 0.1 PE and 2000 PE, the fiber data runs from about 1 PE to 15000 PE. The two parameter fits in Figure 4.11 are performed on the range 0 to 1000 in both cases, although some bare data does not have data points quite this high. We can also see from Figure 4.14 that the χ^2 s are similar from the bare MPPC case.

The fiber parameters from the 2 parameter fits can be seen in Figures 4.15 and 4.16. We can again estimate the necessary parameters from the average of the curve. We find a PDE parameter of 1.028 ± 0.002 , and an effective pixel value of 475.66 ± 2.00 . Figure 4.17 shows an overlay of all fiber data, and the saturation curve with values from the parameter scatter plots.

The results of this calibration are parameters to use in an inversion of the saturation parametrization. This will allow us to convert between between the observed N_{Ava} and the number of photoelectrons which would have been triggered in the absence of saturation effects. A problem with this parametrization becomes evident upon examination of the inverted data and inverted curve, as shown in Figure 4.18. The curve will asymptotically approach N_{eff} as x approaches infinity. As a result, any pulse with more than this number of avalanches falls into a region where the inversion is undefined. However, looking at Figure 4.17, it is not evident that the number of avalanches is limited in this way and it clearly exceeds the 667 available on the MPPC. This is possible because a pixel is able to recharge (either

4.3. Fiber Saturation Studies

by drawing charge off other MPPCs, or by drawing charge from the bias circuitry surround the MPPC). In the case of bare MPPCs the light exposure is less than 100 ps long. However the WLS fiber has a time constant of about 7 ns and second-pulsing effects and other time effects become pertinent. For this reason the calibration is not intended to function above 1000 exposed PE (or above 400 or 500 NAvA), and an ad hoc value is used. Pulses of this size are extremely rare in the FGD in practice.

Another approach to estimating the parameters for a saturation calibration is to perform a fit of all measurements from all available fibers within a given voltage range of interest. If we perform such a fit to the data between 0 and 1000 exposed PE in Figure 4.17, including only points between 0.6 and 0.9V OV (any fits or plots showing data from many MPPCs or fibers are referred to as “global” below), we find that that $N_{eff} = 478.5 \pm 2.018$ and $PDE = 1.02911 \pm 0.00241$. The χ^2 value is about 543.16/590. This seems surprisingly low and suggests we are overestimating the errors in our data points. We can perform the same fit on the range 0 to 500 fired pixels on the inverted curve in Figure 4.18. This produces values $N_{eff} = 518.329 \pm 1.148$ and $PDE = 1.01649 \pm 0.00226$. Both of these are similar to what we had expected from our plot of parameters for individual curves. They demonstrate that as a practical matter, there is very little after-pulsing or cross-talk being included in our fits. These values are in line with the values reported in [25].

We can estimate the expected error of this calibration as the residuals of the data in the OV range used to the curve using the fit parameters. Figure 4.19 shows the residuals for both the saturation and inverted saturation

4.3. Fiber Saturation Studies

curves, with $N_{eff} = 518$ and $PDE=1.02$, as well as $PDE=1.00$. The choice of using a PDE of unity allows us to examine the effect of not correcting for after-pulsing and cross-talk. This would define the exposed light in terms of the limit of the number avalanches per unit power (as defined by the power-meter measurements), rather than the number of PE observed per unit power. This is disadvantageous because it is not a linear light scale, although if the PE measurements are accurate it is within 2% of a linear scale on the range we are interested in. There is an open question as to the best approach of what to do when a pulse occurs which is above the N_{eff} suggested by this calibration. The current approach taken by the FGD software is to set the output value of the calibration to a flag value for the analysis to watch for. This value is currently the inversion of a pulse with $N_{eff}-1$ avalanches plus 10. This value is sub-optimal as it provides a poor estimate of the light level of the curve. A flag value which makes a more realistic estimate of the input light level could be chosen. A value larger than N_{eff} can happen for two reasons in the FGD. At this stage in the software development, this frequently indicates that an ADC to PE conversion was not performed correctly. As mentioned above we expect values larger than N_{eff} to occur due to the physics of the device as well, although very infrequently. Possible avenues for this to occur include recoil protons, alpha rays, and high output particles which happen to traverse a single bar the length of the detector, or deposit a large fraction of their energy in one bar. It is also the case that there are channel to channel variations in the N_{eff} values. One immediate solution might be to use a different functional form on the data which does not have a singularity somewhere inconvenient. Another option

4.3. Fiber Saturation Studies

is to provide an individual calibration for each MPPC in the detector. In the long term, both of these methods are likely to be implemented.

The root mean square of the residuals can provide an estimate of the expected reconstruction error of the calibration. This function is seen in Figure 4.20. Reconstruction errors using our nominal global fits are about 5% below 200 PE, and below about 15% until about 450 PE. Without this calibration, we would expect for $N_{eff}=500$ to have a 35% error in the reconstruction at 450PE, and an 18% error at 200PE. The calibration produces a substantial improvement in this result.

4.3. Fiber Saturation Studies

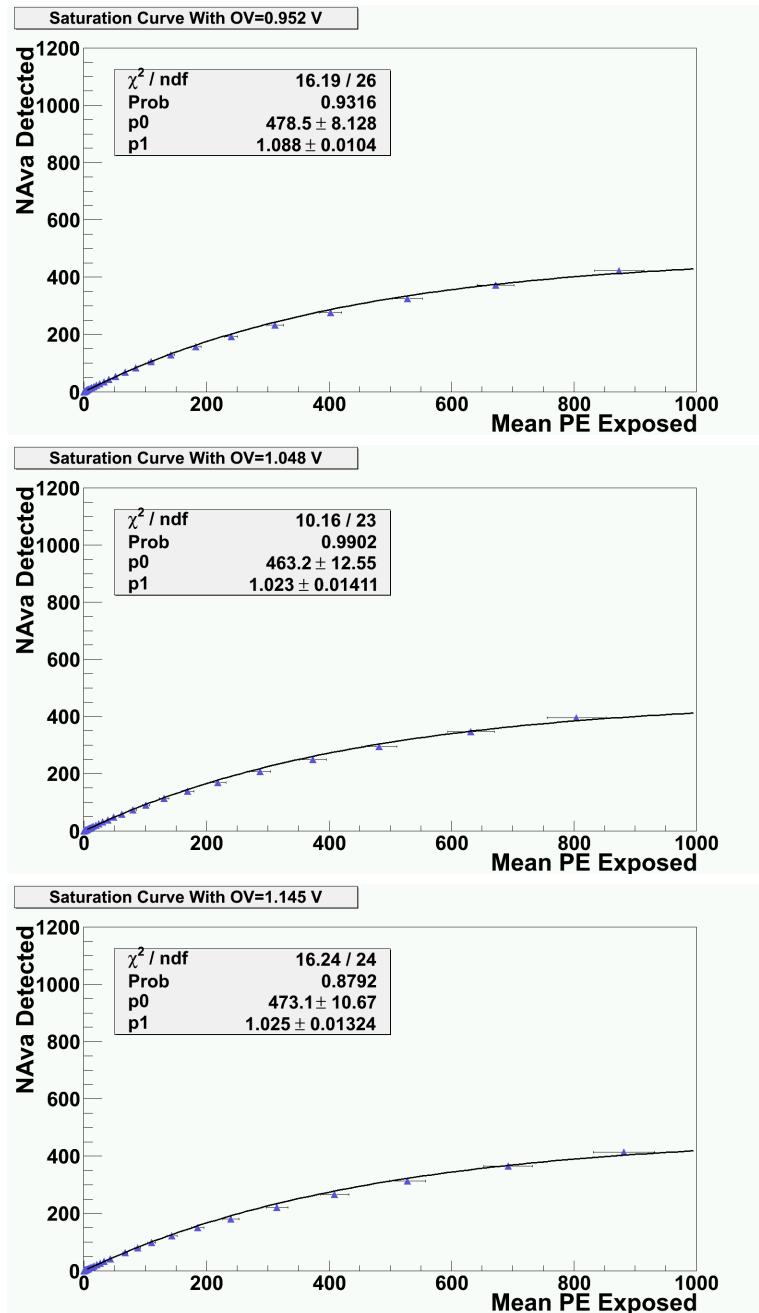


Figure 4.11: Best fits of the fiber data for one MPPC fiber pair to the two parameter saturation function.

4.3. Fiber Saturation Studies

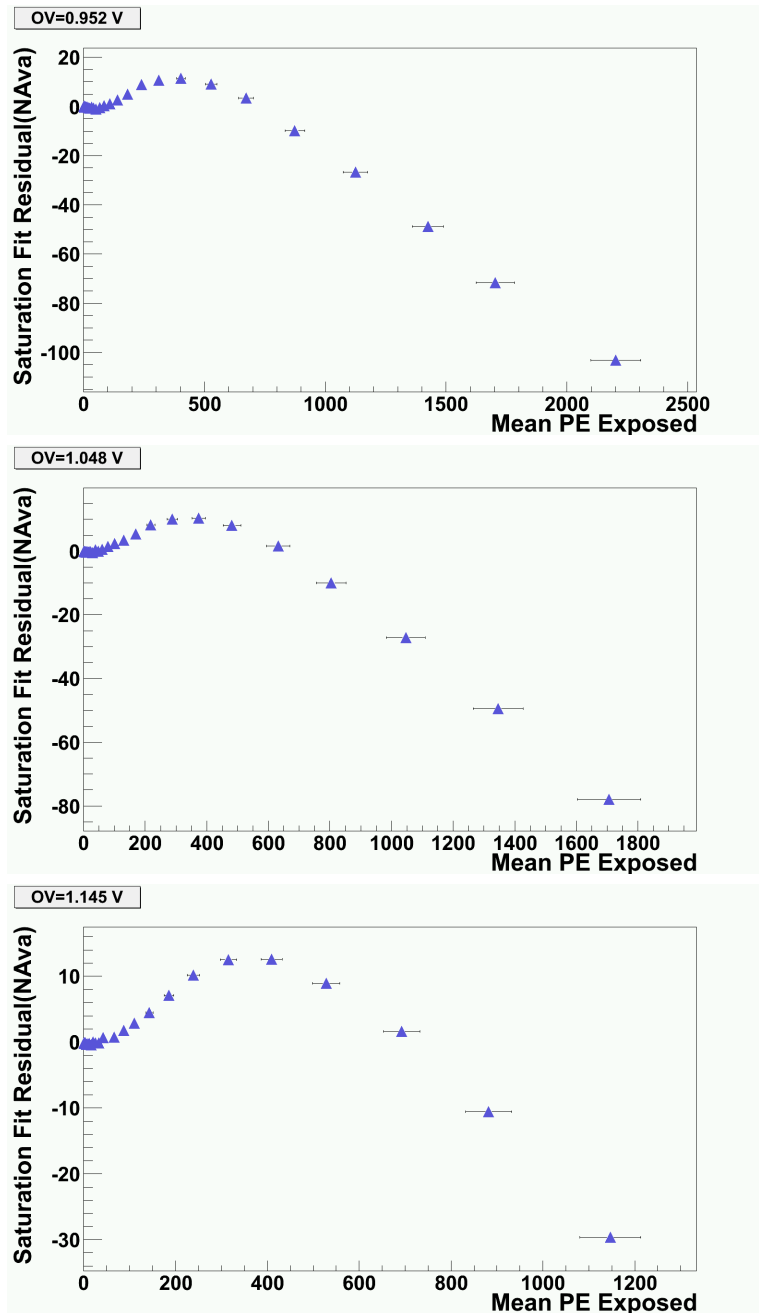


Figure 4.12: This plot shows the residuals of the fiber data to the two parameter saturation function.

4.3. Fiber Saturation Studies

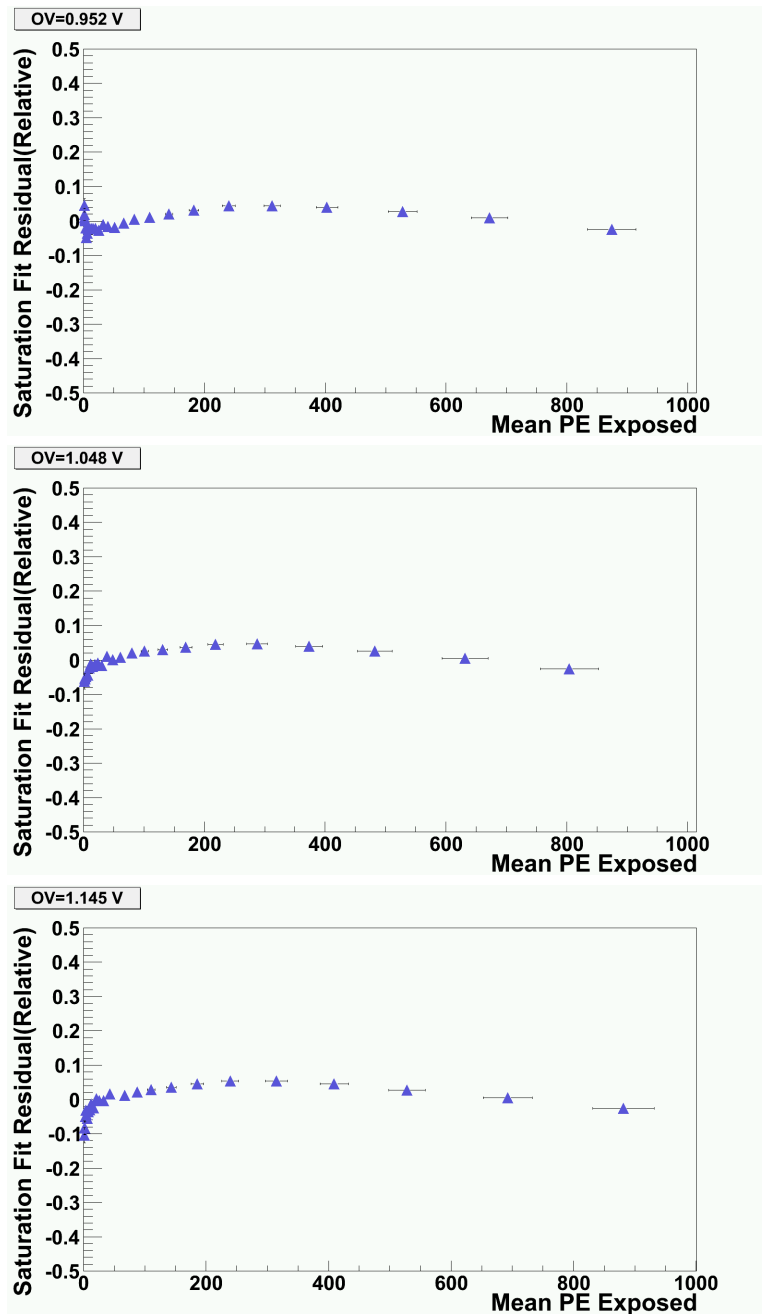


Figure 4.13: This figure shows the relative residuals of the fiber data to the two parameter saturation function. Note that we have excluded the bottom end of the range to allow for meaningful judgments on the high end. The relative residual of a curve that is going near zero is not meaningful when the statistical errors are large compared to the value of the curve. 101

4.3. Fiber Saturation Studies

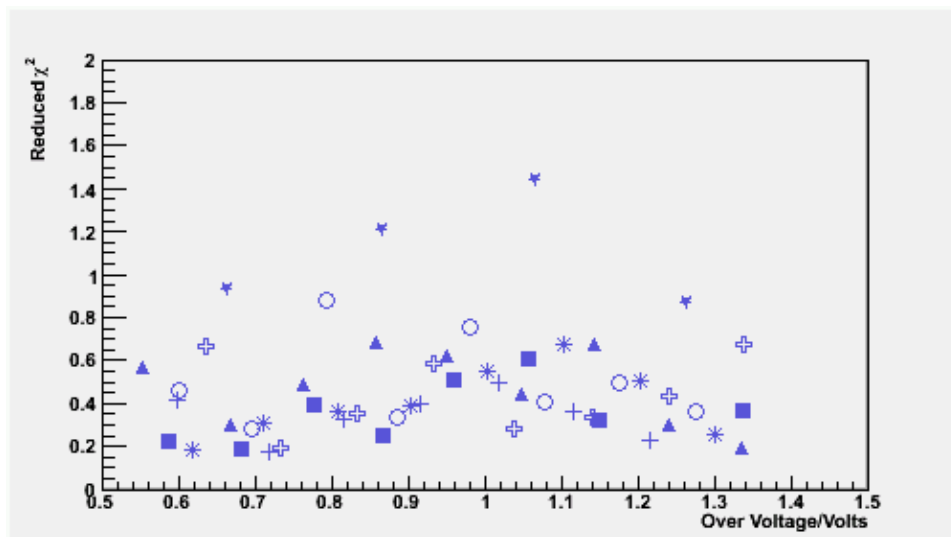


Figure 4.14: This figure shows the chi-squares for MPPC B4371 with all fibers, fit with the standard expression using two parameters. Note that each symbol represents a different fiber. The χ^2 values in this curve are quite low, and suggest we are overestimating the errors on our data points.

4.3. Fiber Saturation Studies

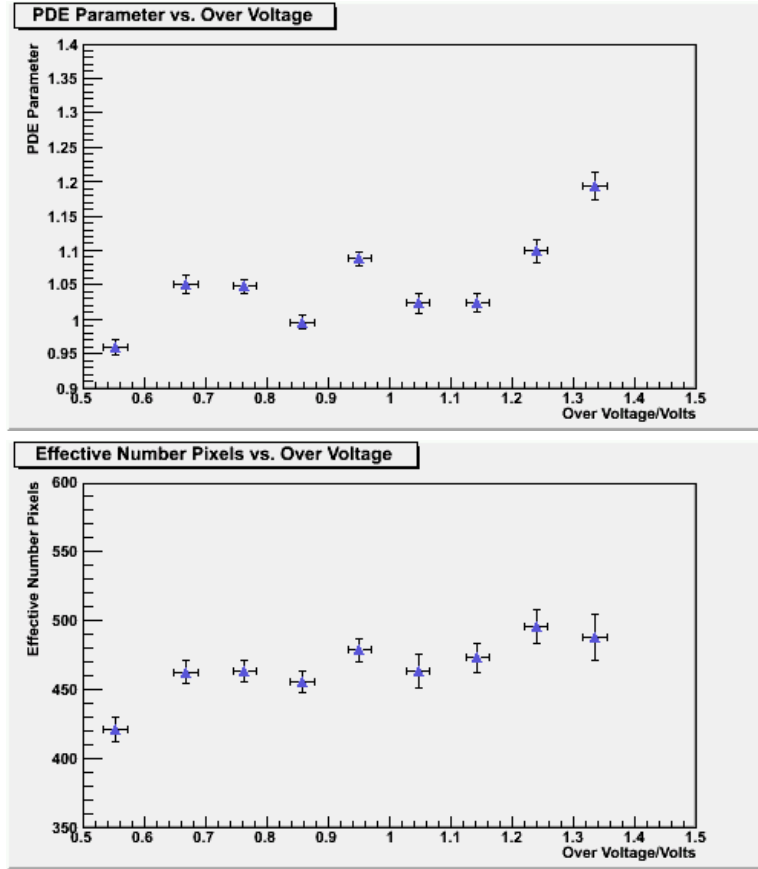


Figure 4.15: The top plot is the PDE parameter for fiber 11 with MPPC B4371 as a function of voltage, whereas the bottom plot show the N_{eff} , the effective pixel count as a function of voltage.

4.3. Fiber Saturation Studies

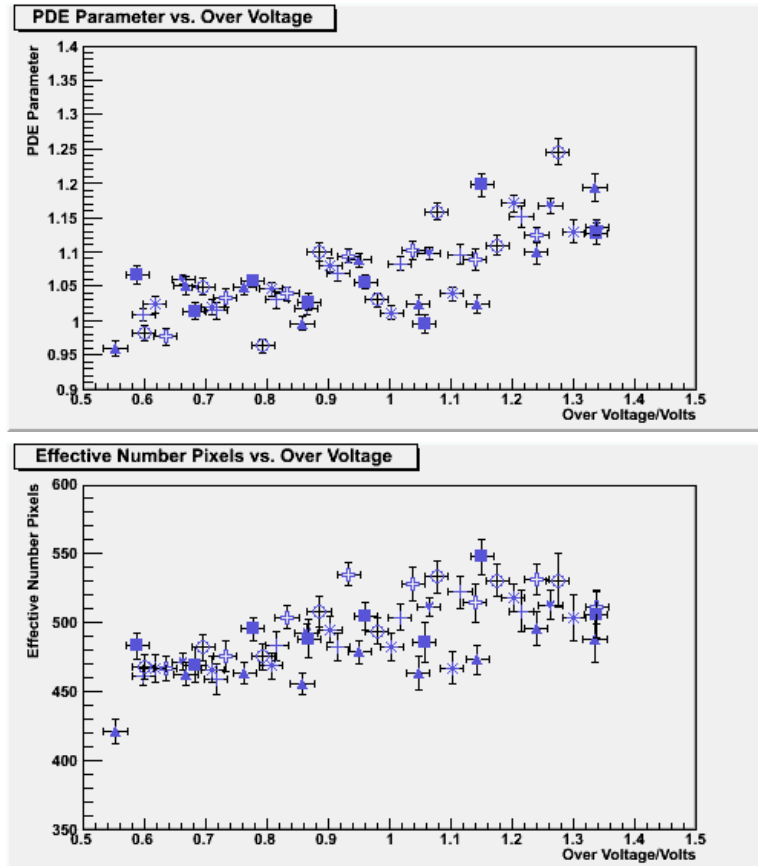


Figure 4.16: The top plot is the PDE parameter for all fibers for MPPC B4371 as a function of voltage, whereas the bottom plot show the N_{eff} , the effective pixel count as a function of voltage. Each symbol is a separate fiber.

4.3. Fiber Saturation Studies

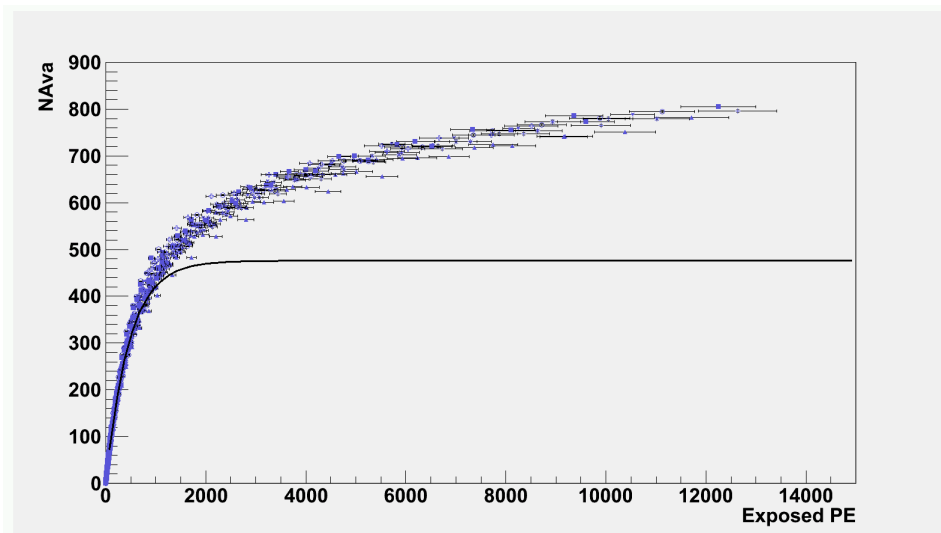


Figure 4.17: This figure shows all data from all fibers with MPPC B4371, with all voltages. The displayed curve is the value consistent with the fits, with $N_{eff}=476$ and $PDE=1.03$.

4.3. Fiber Saturation Studies

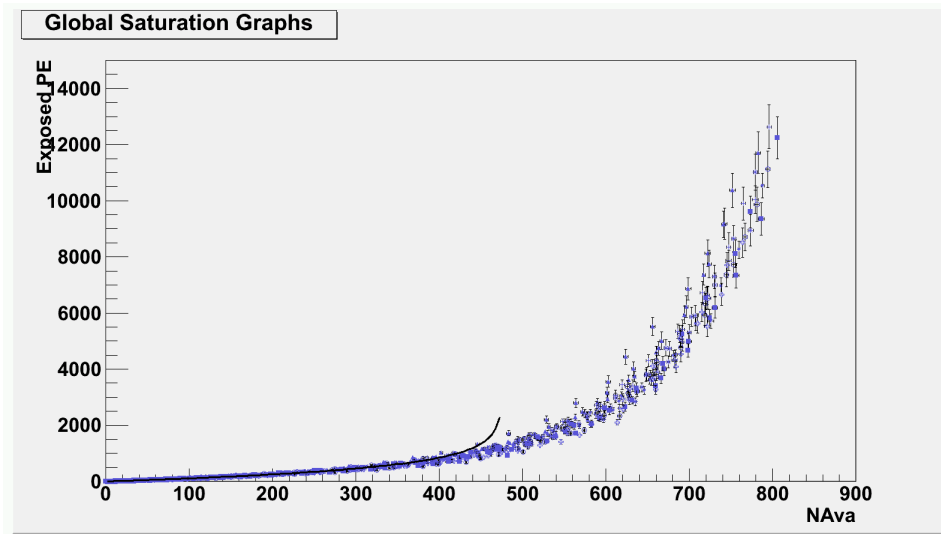


Figure 4.18: This figure shows all data from all fibers with MPPC B4371, with all voltages. It is the inversion of Figure 4.17. The displayed curve is a rough value consistent with the fits, with $N_{eff}=476$ and $PDE=1.03$.

4.3. Fiber Saturation Studies

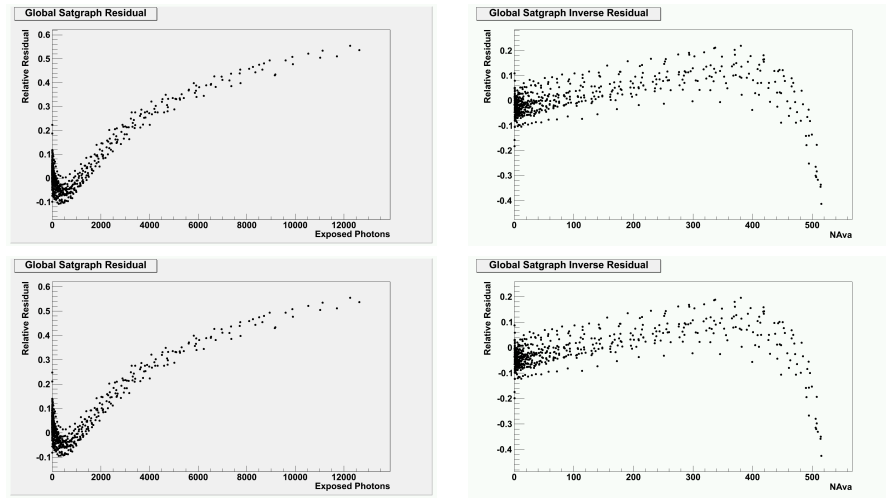


Figure 4.19: This figure illustrates the global residuals to the best fit, with and without an AP+CT correction. The top row uses $N_{eff} = 518$ and $PDE=1.02$, while the bottom row uses $PDE=1.0$. The left hand plots show the residual to the saturation curve, whereas the right hand plots show the expected error in the calibration output. Both plots include data in the range 0.6 to 0.9 V OV.

4.3. Fiber Saturation Studies

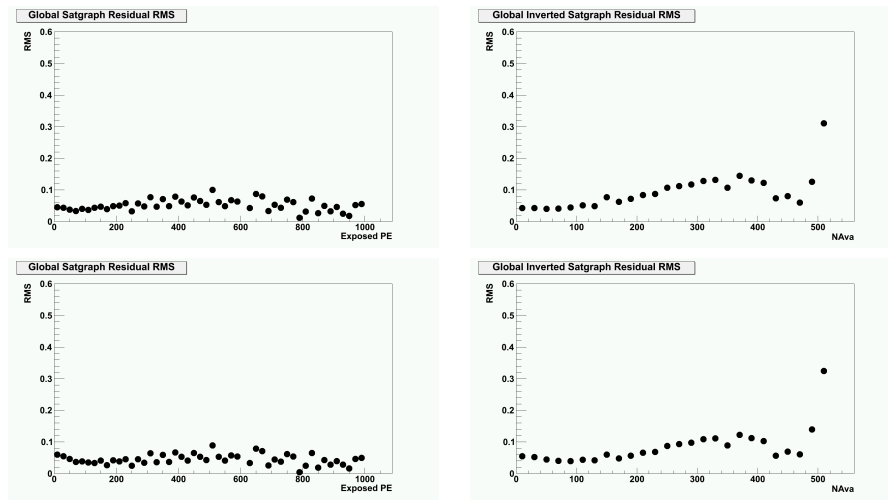


Figure 4.20: This figure illustrates the global RMS of the residuals to the best fit, with and without an after-pulsing and cross-talk correction. The top row uses $N_{eff} = 518$ and $PDE=1.02$, while the bottom row uses $PDE=1.0$. The left hand plots show the residual RMS to the saturation curve, whereas the right hand plots show the expected error in the calibrations reconstruction. Both plots include data in the range 0.6 to 0.9 V OV

Chapter 5

Conclusion

5.1 Calibration Results

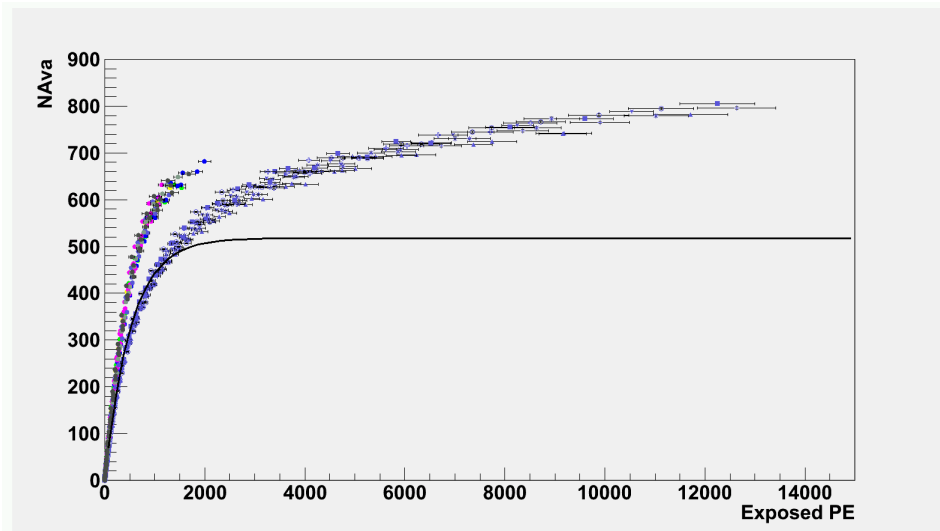


Figure 5.1: This figure shows all bare and fiber data from 2010 overlapped. Different colors represent different MPPCs, while different symbols represent different fibers. The top lines of points are bare MPPCs, whereas the lower line is fiber data. The fit values for the curve are the ones produced for the final result of the calibration: 518 effective pixels, and a slope of 1. Data only includes voltages between 0.6 and 0.9V OV.

The MPPC saturation correction has been completed by producing an effective curve between the observed light output and the predicted light

5.1. Calibration Results

input. A series of sub-calibrations were completed to allow this, including an ADC to PE calibration, a high-low channel conversion, and an OV calibration. A final value of 518 photo-electrons for the N_{eff} parameter and a value of 1 for the PDE parameter are suggested for the purposes of calibration in the detector, and should provide errors below 10% in the main area of interest. The after-pulsing and cross-talk probability was found to be 1.6% in the range of interest. Figure 5.1 shows the final calibration in the context of the entire data set, including bare and fiber data. As was expected, the fiber data saturates at a substantially lower level. However, other effects seem to extend it slowly after reaching saturation, allowing it to continue to grow long after the illuminated pixels have all fired at least once.

The primary limitation of this work is the lack of understanding of the response function of the electronics and pulse-finding system. Without a better characterization of these systems, it is impossible to correctly identify the component of after pulsing and cross-talk present in the NAva signal. This limitation is most important in the calibration of the linear light scale, which should have an intercept of zero. That it does not implies that the combination of noise and signal is not being correctly compensated for. This means that the response to the combined signal is not the sum of the two sub-signals, and calls into question the low level linearity of the device. It is assumed that by staying well above the dark noise level (0.1 PE), we are avoiding this issue, but it is by no means confirmed. Simulation and direct measurements may be the only way to solve this conundrum. For these reasons, in the authors opinion, the value of N_{eff} can be taken as

accurate. However, the PDE parameter most likely should not be trusted as a measurement of after-pulsing and cross-talk, and the best approach would be to correct to a scale which includes after-pulsing and cross-talk, rather than try to correct to a linear scale with light.

5.2 Future Work

Future work should focus on two main areas. First, the calibration has not been individualized for specific MPPCs. This issue must be explored as values substantially different from the predicted value will result in very corrupted data values at higher light level. While very little variation is visible in Figure 5.1 between the two classes of measurements, the number of distinct samples collected is still small (7 fibers) compared to the 8448 MPPCs in the FGD. This work would most likely require repairing and calibrating the light pulser boards in the FGDs, although it is conceivable that cosmics may provide enough high energy events to perform these scans as well. As there is no way of guaranteeing that the DAC values set on the LPBs are linear, the most likely solution is to use nearby MPPCs to measure in their own linear range the output of an LED, and then use that light scale to calibrate the saturated MPPC. This would essentially use neighboring MPPCs in the same fashion as the measurements in this work used a power-meter.

A second area that must be understood is the MPPC's response function when convoluted with the ASIC and pulse-finder. Without a good understanding of this bias in the cases which are most difficult for the pulse

5.2. *Future Work*

finder it is impossible to perform an accurate measurement of after-pulsing and cross-talk. The worst understood bias of the pulse-finder occurs immediately after another pulse - precisely where you expect to find after-pulses. As cross-talk and after-pulsing are believed to vary substantially between MP-PCs, it may be desirable to understand these scales for every MPPC. This response function may also explain the non-linear response near 1PE. Such a characterization most likely will be done by simulation, with cross-checks with another electrical system which has a fast-amplifier able to distinguish much finer pulse-separation.

Bibliography

- [1] T2k nd280 conceptual design report. Internal T2K Document, 2005.
- [2] <http://www.pbs.org/wgbh/nova/neutrino/missing.html>. Website, February 2006.
- [3] Nd280 review document for ipns. Internal T2K Document, 2006.
- [4] <http://www.symmetrymagazine.org/cms/?pid=1000450>. Website, 2007.
- [5] F. retire. Personal Correspondance, August 2010.
- [6] James S. Allen. *THE NEUTRINO*. PRINCETON UNIVERSITY PRESS, PRINCETON, NEW JERSEY, 1958.
- [7] Y. Ashie, J. Hosaka, K. Ishihara, Y. Itow, J. Kameda, Y. Koshio, A. Minamino, C. Mitsuda, M. Miura, S. Moriyama, M. Nakahata, T. Namba, R. Nambu, Y. Obayashi, M. Shiozawa, Y. Suzuki, Y. Takeuchi, K. Taki, S. Yamada, M. Ishitsuka, T. Kajita, K. Kaneyuki, S. Nakayama, A. Okada, K. Okumura, C. Saji, Y. Takenaga, S. T. Clark, S. Desai, E. Kearns, S. Likhoded, J. L. Stone, L. R. Sulak, W. Wang, M. Goldhaber, D. Casper, J. P. Cravens, W. Gajewski, W. R. Kropp, D. W. Liu, S. Mine, M. B. Smy, H. W. Sobel, C. W. Sterner, M. R. Vagins,

Bibliography

- K. S. Ganezer, J. Hill, W. E. Keig, J. S. Jang, J. Y. Kim, I. T. Lim, K. Scholberg, C. W. Walter, R. W. Ellsworth, S. Tasaka, G. Guillian, A. Kibayashi, J. G. Learned, S. Matsuno, D. Takemori, M. D. Messier, Y. Hayato, A. K. Ichikawa, T. Ishida, T. Ishii, T. Iwashita, T. Kobayashi, T. Maruyama, K. Nakamura, K. Nitta, Y. Oyama, M. Sakuda, Y. Totsuka, A. T. Suzuki, M. Hasegawa, K. Hayashi, I. Kato, H. Maesaka, T. Morita, T. Nakaya, K. Nishikawa, T. Sasaki, S. Ueda, S. Yamamoto, T. J. Haines, S. Dazeley, S. Hatakeyama, R. Svoboda, E. Blaufuss, J. A. Goodman, G. W. Sullivan, D. Turcan, A. Habig, Y. Fukuda, C. K. Jung, T. Kato, K. Kobayashi, M. Malek, C. Mauger, C. McGrew, A. Sarrat, E. Sharkey, C. Yanagisawa, T. Toshito, K. Miyano, N. Tamura, J. Ishii, Y. Kuno, M. Yoshida, S. B. Kim, J. Yoo, H. Okazawa, T. Ishizuka, Y. Choi, H. K. Seo, Y. Gando, T. Hasegawa, K. Inoue, J. Shirai, A. Suzuki, M. Koshiba, Y. Nakajima, K. Nishijima, T. Harada, H. Ishino, Y. Watanabe, D. Kielczewska, J. Zalipska, H. G. Berns, R. Gran, K. K. Shiraishi, A. Stachyra, K. Washburn, and R. J. Wilkes. Measurement of atmospheric neutrino oscillation parameters by super-kamiokande i. *Phys. Rev. D*, 71(11):112005, Jun 2005.
- [8] P. Baron, D. Calvet, E. Delagnes, X. de La Broise, A. Delbart, F. Druillole, E. Mazzucato, E. Monmarthe, F. Pierre, and M. Zito. AFTER, an ASIC for the Readout of the Large T2K Time Projection Chambers. *IEEE Transactions on Nuclear Science*, 55:1744–1752, June 2008.
- [9] D. Bishop. Feb64.rev2 schematics. Internal Document, 2010.

Bibliography

- [10] Martyn Bryant. Plastic scintillators for the t2k fine-grained detector. *Masters Thesis*, 2007.
- [11] B. T. Cleveland, T. Daily, R. Davis, Jr., J. R. Distel, K. Lande, C. K. Lee, P. S. Wildenhain, and J. Ullman. Measurement of the Solar Electron Neutrino Flux with the Homestake Chlorine Detector. *Astrophysical Journal*, 496:505–+, March 1998.
- [12] Y. Du and F. Retire. After-pulsing and cross-talk in multi-pixel photon counters. *Nuclear Instruments and Methods in Physics Research Section A: Accelerators, Spectrometers, Detectors and Associated Equipment*, 596(3):396 – 401, 2008.
- [13] K. Eguchi, S. Enomoto, K. Furuno, J. Goldman, H. Hanada, H. Ikeda, K. Ikeda, K. Inoue, K. Ishihara, W. Itoh, T. Iwamoto, T. Kawaguchi, T. Kawashima, H. Kinoshita, Y. Kishimoto, M. Koga, Y. Koseki, T. Maeda, T. Mitsui, M. Motoki, K. Nakajima, M. Nakajima, T. Nakajima, H. Ogawa, K. Owada, T. Sakabe, I. Shimizu, J. Shirai, F. Suekane, A. Suzuki, K. Tada, O. Tajima, T. Takayama, K. Tamae, H. Watanabe, J. Busenitz, Z. Djurcic, K. McKinny, D.-M. Mei, A. Piepke, E. Yaku-shev, B. E. Berger, Y. D. Chan, M. P. Decowski, D. A. Dwyer, S. J. Freedman, Y. Fu, B. K. Fujikawa, K. M. Heeger, K. T. Lesko, K.-B. Luk, H. Murayama, D. R. Nygren, C. E. Okada, A. W. P. Poon, H. M. Steiner, L. A. Winslow, G. A. Horton-Smith, R. D. McKeown, J. Ritter, B. Tipton, P. Vogel, C. E. Lane, T. Miletic, P. W. Gorham, G. Guillian, J. G. Learned, J. Maricic, S. Matsuno, S. Pakvasa, S. Dazeley, S. Hatakeyama, M. Murakami, R. C. Svoboda, B. D. Dieterle, M. Di-

Bibliography

- Mauro, J. Detwiler, G. Gratta, K. Ishii, N. Tolich, Y. Uchida, M. Batygov, W. Bugg, H. Cohn, Y. Efremenko, Y. Kamyshev, A. Kozlov, Y. Nakamura, L. De Braekeleer, C. R. Gould, H. J. Karwowski, D. M. Markoff, J. A. Messimore, K. Nakamura, R. M. Rohm, W. Tornow, A. R. Young, and Y.-F. Wang. First results from kamland: Evidence for reactor antineutrino disappearance. *Phys. Rev. Lett.*, 90(2):021802, Jan 2003.
- [14] Ahmad et. al. Direct evidence for neutrino flavor transformation from neutral-current interactions in the sudbury neutrino observatory. *Phys. Rev. Lett.*, 89, 2002.
- [15] G. Feinberg and S. Weinberg. Law of conservation of muons. *Phys. Rev. Lett.*, 6(7):381–383, Apr 1961.
- [16] Tsuyoshi Nakaya Hajime Kubo, Kodai Matsuoka and Masashi Yokoyama. Development of the muon beam monitor for the t2k long baseline neutrino oscillation experiment. *IEEE Nuclear Science Symposium Conference Record*, 2008.
- [17] Hamamatsu. Delivery specification sheet prototype. Internal Document, 2007.
- [18] C. L. Cowan Jr., F. Reines, F. B. Harrison, H. W. Kruse, and A. D. McGuire. Detection of the free neutrino: A confirmation. *Science*, 124(3212):103–104, 1956.
- [19] Boris Kayser. Neutrino mass, mixing, and flavor change. <http://arxiv.org/abs/0804.1497>, 2008.

Bibliography

- [20] Seth H. Neddermeyer and Carl D. Anderson. Note on the nature of cosmic-ray particles. *Physical Review*, 51:884 – 886, 1937.
- [21] M. L. Perl, G. S. Abrams, A. M. Boyarski, M. Breidenbach, D. D. Briggs, F. Bulos, W. Chinowsky, J. T. Dakin, G. J. Feldman, C. E. Friedberg, D. Fryberger, G. Goldhaber, G. Hanson, F. B. Heile, B. Jean-Marie, J. A. Kadyk, R. R. Larsen, A. M. Litke, D. Lüke, B. A. Lulu, V. Lüth, D. Lyon, C. C. Morehouse, J. M. Paterson, F. M. Pierre, T. P. Pun, P. A. Rapidis, B. Richter, B. Sadoulet, R. F. Schwitters, W. Tanenbaum, G. H. Trilling, F. Vannucci, J. S. Whitaker, F. C. Winkelmann, and J. E. Wiss. Evidence for anomalous lepton production in e^+e^- annihilation. *Phys. Rev. Lett.*, 35(22):1489–1492, Dec 1975.
- [22] D. Runker and E. Lorenz. Advances in solid state photon detectors. *Journal of Instrumentation*, 4, 2009.
- [23] Yoichiro Suzuki. Kamiokande solar neutrino results. *Nuclear Physics B - Proceedings Supplements*, 38(1-3):54 – 59, 1995. Neutrino 94.
- [24] Brian Kirby Thomas Lindner. Fgd raw data manual. Internal Document, 2010.
- [25] M. Yokoyama, T. Nakaya, S. Gomi, A. Minamino, N. Nagai, K. Nitta, D. Orme, M. Otani, T. Murakami, T. Nakadaira, and M. Tanaka. Mass production test of hamamatsu mppc for t2k neutrino oscillation experiment. *Nuclear Instruments and Methods in Physics Research Section A: Accelerators, Spectrometers, Detectors and Associated Equipment*, 610(1):362 – 365, 2009. New Developments In Photodetection NDIP08,

Proceedings of the Fifth International Conference on New Developments in Photodetection.

The Attenuation Calibration

The actual results of the attenuation calibration are displayed in the table below. Errors are cited as they were used in this work: as if extrapolating from 40 dB. This incorporates non-reproducibility of the measurement. Scans Reproducibility will vary depending on the range used, and the errors below are only valid for full range scans between 0 and 40. For attenuator #2 with serial number 86971-02, the constants are in the following tables.

The Attenuation Calibration

dB requested	Calibrated Intensity	Calibration Error
0.0e+00	2.692811e-05	7.765873e-07
5.0e-01	2.363718e-05	6.714473e-07
1.0e+00	2.110012e-05	5.110826e-07
1.5e+00	1.947552e-05	5.598682e-07
2.0e+00	1.780758e-05	4.968369e-07
2.5e+00	1.647225e-05	6.462483e-07
3.0e+00	1.433003e-05	3.924854e-07
3.5e+00	1.287444e-05	3.850888e-07
4.0e+00	1.153363e-05	3.283549e-07
4.5e+00	1.031817e-05	2.739072e-07
5.0e+00	9.232828e-06	2.464630e-07
5.5e+00	8.190004e-06	2.127240e-07
6.0e+00	7.268483e-06	1.831074e-07
6.5e+00	6.500027e-06	1.589501e-07
7.0e+00	5.722538e-06	1.365106e-07
7.5e+00	5.035802e-06	1.138241e-07
8.0e+00	4.460878e-06	9.558578e-08
8.5e+00	3.961142e-06	8.402201e-08
9.0e+00	3.460676e-06	6.922815e-08
9.5e+00	3.030227e-06	5.775210e-08
1.0e+01	2.676886e-06	5.021978e-08
1.05+01	2.379658e-06	4.167037e-08
1.1e+01	2.239790e-06	3.696725e-08
1.15+01	2.009342e-06	3.330571e-08
1.2e+01	1.768193e-06	2.730383e-08
1.25+01	1.551116e-06	2.591824e-08
1.3e+01	1.373998e-06	2.365820e-08
1.35e+01	1.205456e-06	1.974254e-08
1.4e+01	1.056253e-06	1.479121e-08
1.45e+01	9.353961e-07	1.297766e-08

Table 1: Part One of constants for calibrating the digital optical attenuator

The Attenuation Calibration

dB requested	Calibrated Intensity	Calibration Error
1.5e+01	8.298535e-07	1.371613e-08
1.55e+01	7.240724e-07	9.343691e-09
1.6e+01	6.330192e-07	7.890742e-09
1.65e+01	5.568306e-07	6.684864e-09
1.7e+01	4.904566e-07	5.846013e-09
1.75e+01	4.297515e-07	5.060600e-09
1.8e+01	3.774894e-07	4.412240e-09
1.85e+01	3.310332e-07	4.651443e-09
1.9e+01	2.869676e-07	3.232407e-09
1.95e+01	2.522816e-07	2.976521e-09
2.0e+01	2.224839e-07	2.651266e-09
2.05e+01	1.958116e-07	2.280289e-09
2.1e+01	1.718565e-07	2.381064e-09
2.15e+01	1.505716e-07	1.843581e-09
2.2e+01	1.326279e-07	1.650451e-09
2.25e+01	1.182030e-07	1.543116e-09
2.3e+01	1.050672e-07	1.481947e-09
2.35e+01	9.250891e-08	1.218391e-09
2.4e+01	8.055245e-08	1.390949e-09
2.45e+01	7.183555e-08	9.211893e-10
2.5e+01	6.378557e-08	8.925768e-10
2.55e+01	5.749171e-08	7.555599e-10
2.6e+01	5.133882e-08	6.027641e-10
2.65e+01	4.519095e-08	5.710273e-10
2.7e+01	3.963159e-08	5.538517e-10
2.75e+01	3.531162e-08	3.923691e-10
2.8e+01	3.145687e-08	3.464539e-10
2.85e+01	2.809624e-08	2.963661e-10
2.9e+01	2.497438e-08	2.562882e-10
2.95e+01	2.214529e-08	1.976804e-10

Table 2: Part Two of constants for calibrating the digital optical attenuator

dB requested	Calibrated Intensity	Calibration Error
3.0e+01	1.960921e-08	1.714688e-10
3.05e+01	1.729741e-08	1.141699e-10
3.1e+01	1.532712e-08	9.605960e-11
3.15e+01	1.355426e-08	7.368602e-11
3.2e+01	1.203372e-08	5.729198e-11
3.25e+01	1.067354e-08	4.364107e-11
3.3e+01	9.460260e-09	6.859852e-11
3.35e+01	8.302921e-09	3.086391e-11
3.4e+01	7.220449e-09	2.075973e-11
3.45e+01	6.345564e-09	1.521277e-11
3.5e+01	5.621162e-09	2.018373e-11
3.55e+01	4.992788e-09	1.886619e-11
3.6e+01	4.438257e-09	1.817344e-11
3.65e+01	3.917134e-09	1.897954e-11
3.7e+01	3.442399e-09	1.186460e-11
3.75e+01	3.011378e-09	8.145826e-12
3.8e+01	2.639002e-09	5.524726e-12
3.85e+01	2.320373e-09	1.135562e-11
3.9e+01	2.063541e-09	3.058285e-12
3.95e+01	1.835432e-09	1.764841e-12
4.0e+01	1.633784e-09	2.128431e-12

Table 3: Parts three of constants for calibrating the digital optical attenuator